# From Energy Generation to Storage: The Exploration of Unusual Architectures and Applications of Conjugated Organic Molecules

David Fraser Zeigler

A dissertation submitted in partial fulfillment of the requirements for the degree of

Doctor of Philosophy

University of Washington

2014

Reading committee:
Professor Christine K. Luscombe, Chair
Professor Samson A. Jenekhe
Professor D. Michael Heinekey

Program Authorized to Offer Degree:

Chemistry

University of Washington

## Abstract

# The Exploration of Unusual Architectures and Applications of Conjugated Organic Molecules

David Fraser Zeigler
Chair of the Supervisory Committee:
Professor Christine K. Luscombe
Materials Science and Engineering

The advent of conjugated polymers spurred the field of organic electronics. Since the inception of the field, many have lauded the potential benefits of organic over inorganic platforms, including their light weight, flexibility, and solution-processability, the latter of which makes them amenable to large-scale mass production. Unfortunately, the performance of organic electronics generally pales in comparison to their inorganic analogues. However, synthetic chemistry allows the unprecedented control over the structure and function of conjugated materials at the molecular levels, which is difficult to achieve in bulk inorganic crystals. Currently, donor-acceptor (D-A) polymers and small molecules are the benchmark for light-harvesting materials in organic photovoltaics (OPVs). Using careful design criteria, manipulation of the structure and components of D-A materials can yield organic materials with unique electronic and photonic properties. This can provide increasingly nuanced methods with which to construct novel materials and modify their properties. Such precise and predictable structure-property control is crucial to realizing technological advances in organic electronics. This body of work explores two non-traditional architectures for conjugated polymers and dual-purpose electrochromic light-harvesting molecules.

In the first case, a thiophene-triphenylamine polymer with aldehyde-functionalized indacenodithiophene (IDT) side chains was synthesized. This parent polymer was modified by condensing electron-deficient units on the IDT side chain to achieve a series of polymers with differing absorption and energy levels. The effect of acceptor identity on the polymer properties was probed optically and electrochemically using UV-visible spectroscopy and cyclic voltammetry, respectively. The polymers were tested in organic field effect transistors (OFETs) and OPV devices. It was found that the more electron-deficient molecules led to a deeper lowest unoccupied molecular orbital (LUMO) while leaving the highest occupied molecular orbital (HOMO) unchanged, which thereby caused a redshift of the internal charge transfer (ICT) absorption peak. This was corroborated using Density Functional Theory (DFT), which revealed that the LUMO of the polymer was localized at the terminus of the side chain, while the polymer HOMO was delocalized along the polymer backbone. Overall, the polymer with a thiobarbituric acid acceptor showed the best performance, with a hole mobility ($\mu_h$) of ~1 × $10^{-3}$ $cm^2/Vs$ and a power conversion efficiency (PCE) of 2.5%.

In the second case, a comb copolymer with poly(3-hexyl)thiophene (P3HT) side chains and a carbazole-diketopyrrolopyrrole backbone was synthesized via a graft through approach. This required the development of an unexplored synthetic methodology, which involved the growth of P3HT from a boronic ester-functionalized carbazole to yield a carbazole-P3HT macromonomer, which was then coupled to the diketopyrrolopyrrole monomer through a Suzuki polymerization. Macromonomers with four different P3HT lengths were synthesized and characterized with UV-visible spectroscopy, cyclic voltammetry, gel permeation chromatography and matrix-assisted laser desorption ionization time-of-flight (MALDI-TOF). These macromonomers were then used to make the final comb copolymers, which were subsequently characterized with the same techniques, as well as differential scanning calorimetry (DSC). It was found that the optical and electronic properties of the P3HT chains and the D-A backbone were largely independent. Moreover, the relative expression of the P3HT and D-A properties were proportional to the P3HT length; longer P3HT chains suppressed the D-A characteristics and vice versa. These final comb copolymers were further utilized in OFETs and their films were characterized by atomic force microscopy (AFM). As the active material in OFETs, these comb copolymers behave most like their largest constituent component. The comb copolymer with the longest P3HT chains showed p-type behavior with similar $\mu_h$ values (~6 × $10^{-4}$ $cm^2/Vs$) compared to neat P3HT. Meanwhile, the comb copolymers with the shortest P3HT chains showed ambipolar charge transport and similar mobilities to the control D-A polymer.

Additionally, a number of molecules have been designed, synthesized and characterized for use in dual-purpose electrochromic light-harvesting windows with the architecture of a dye-sensitized solar cell (DSSC). The dyes were intended to function as the TiO2 sensitizer in DSSC function; upon applying a reverse bias to the DSSC, these dyes would ideally transition from a colored to a transparent state. Thus, this DSSC could harvest sunlight on a bright day, but, by reversing current flow, could also allow passive solar heating/lighting on a cloudy day. The design and synthesis of a menagerie of dyes is discussed, including dyes based on perylene diimide (PDI), Methylene Blue, and phthalocyanines. To date, one phthalocyanine dye has shown electrochromic behavior, but it transitions between a green (neutral state) and magenta (reduced state) color.

Finally, hyperbranched ambipolar triphenylamine-based polymers were designed for use as the electrodes of symmetric supercapacitors. Ideally, these polymers would be able to retain more charge than activated carbon (the current benchmark for electrode materials) due to their predilection to engage in redox processes. A series of three triphenylamine-napthalene diimide polymers with a differing number of thiophene spacers were generated through solution polymerization. Initially, a symmetric supercapacitor was made from the first iteration, but yielded poor performance. To further investigate the properties of these materials, the polymers were used to make asymmetric supercapacitors. These devices revealed that the polymers had much better n-type properties, making them useful as the negative electrode of the supercapacitor. However, they did not readily engage in oxidation, making their utility as a positive electrode limited. Overall, the best of the asymmetric supercapacitors achieved a reasonable capacitance of ~22 F/g, which is roughly one order of magnitude lower than activated carbon.

These studies showcase the versatility of organic materials for electronics applications. The synthetic methodologies discussed herein can be used to exercise complete control the structure of organic molecules, and to tune their resultant electronic, optical and chemical properties. This adaptability is evidenced by the fact that they can be used for light-harvesting, energy storage and numerous other applications in the realm of organic electronics. Overall, this body of research provides a glimpse into the vast number of unexplored structures and applications of conjugated organic materials.

# Acknowledgements

First and foremost, my eternal thanks to the organizations that have funded my research throughout graduate school: the National Science Foundation and the Washington State Clean Energy Institute. I would like to extend thanks to the various members of my committee for thought-provoking discussions and critical suggestions. However, I must explicitly and humbly thank Dr. Christine Luscombe, who took me into her group out of compassion and has patiently suffered my zany ideas in the intervening years, providing me with the perfect balance of advice and autonomy throughout. In that vein, I thank all of the past and present members of the Luscombe group, as coworkers, copyeditors (Andrew Rice, Trevor Martin and Kat Mazzio, particularly) and as friends. Additionally, I thank other colleagues and collaborators outside of the Luscombe group. Although these people are too numerous to list exhaustively, one deserves special recognition: Dr. Josh Davies, who mentored me as a fledgling graduate student and taught me all that I know about the mechanics of synthetic chemistry and has also been a boon companion throughout my time in Seattle.

Secondly, this is dedicated to my parents. Without their steady unreserved support, I would have neither the curiosity nor the aptitude to complete such an endeavor. I cannot thank you enough for never monomaniacally pushing me to pursue a given activity (except math workbooks as a youngster!), but for always encouraging me in whatever enterprises – whimsical and otherwise – piqued my interest. Their ethos and reverence for the natural world is the source of my desire to work on renewable energy. By extension, I must thank my sister. Primarily for being a generally stellar sibling, but also for being a superb role model, advice-dispenser, and purveyor of new music throughout our upbringing. Her positivity and effort despite the adversity of a debilitating injury has illustrated the true meaning of fortitude and strength and for that reason and others, will always be an inspiration to me. I could not ask for a better family – what an exuberant, adventurous, loving clan! Moreover, I would be remiss not to thank my friends in this city that have provided me with joyous memories, humorous (and not-so-humorous) diversions, and glorious adventures.

Finally, the rest of this dedication is for Emilie. The commencement of graduate school coincided with our first shared day; in mere hours, it became obvious that our minds were on the same wavelength and the immediate, unforced rapport between us was impossible to ignore. From thenceforth, you have been my mate and friend, confidant and co-conspirator. How could I ever adequately express how thankful I am to have met you? Never have I met someone so strong, so thoughtful, so generous, or someone that understood my brain so thoroughly. There is no one else that is sufficiently peculiar to appreciate my eccentricities, tough enough to willingly endure grueling backcountry trips, and patient enough to pardon my occasional cantankerousness and impertinence. What began with screenings of Hitchcock films has evolved into five years of wonderful memories: bike rides, urban perambulation, wilderness excursions, volunteer events and the associated foodstuffs(!), road trips, concerts, garage sales, and too many other experiences to enumerate, both good and bad. I would not have been able to complete this journey without your love and support. I look forward to the journeys to come: days of delinquency, years of exploration, a lifetime of companionship, and, most of all, finding the perfect alpine meadow to situate a solar-powered cabin and ultimately becoming hermits alone together in the mountains!

# Table of Contents

Page number

## List of Figures:

## List of Schemes:

## List of Tables:

# 1. Introduction

## 1.1 Organic Photovoltaics

The continuous expansion of the global population is placing an ever-increasing strain on our resources and environment. Left unchecked, this growth will amplify our energy demands at an alarming rate. The current major sources of electricity – coal, oil, and gas – are finite and will become more economically costly and environmentally detrimental to extract from the earth. Thus, it is exceedingly important to find an efficient, sustainable and cost-effective strategy to capture and store electricity. Of all the potential renewable energy sources, solar energy is the most abundant and readily available.[1] Inorganic solar cells can convert solar energy to electricity efficiently, but are often prohibitively expensive for commercial implementation. However, with the advent of semiconducting polymers, organic photovoltaics (OPVs) became a promising technology. In the intervening decades, OPV has emerged as an intriguing alternative to inorganic cells due to their light weight, potential for inexpensive solution processability, and potential for large-scale roll-to-roll processing.[2] Unfortunately, OPV devices tend to suffer from depressed power conversion efficiencies (PCE) and degrade rapidly compared to their inorganic analogues.[3] To date, the bulk of the research aimed to improve the PCE of OPV devices focus on the development of new p- and n-type semiconducting molecules to improve light-harvesting or charge transport through the cell[4-19] or precise control of the molecular nanostructure of the device.[20-27]

## 1.2 Semiconducting Organic Materials

To date, most OPVs are based on semiconducting polymers or small molecules. The one defining feature of these materials is that they have fully-conjugated backbones

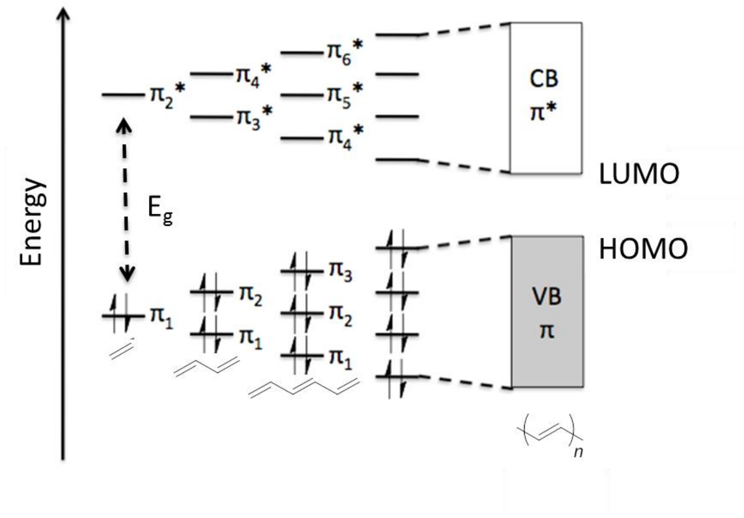

*Figure 1.1: Evolution of discrete to continuous energy levels for polyenes*

– i.e. alternating single and double bonds along the length of the molecule. These double bonds form by electrons that are shared by adjacent $sp^2$-hybridized carbon $p_z$ orbitals; a large amount of overlap is required for electrons to be shared between the two $p_z$ orbitals. Also, since the electrons in these orbitals sit above and below the planar backbone of the material, they result in a highly polarizable delocalized electron cloud over the molecule.[28] Smaller conjugated molecules and oligomers have a discrete highest occupied molecular orbital (HOMO) and lowest unoccupied molecular orbital (LUMO). As the length of conjugation increases from oligomer to polymer, these discrete orbitals have slightly different energies based on their chemical environment and they blend into a continuous band structure, common to inorganic semiconductors (Figure 1.1). In this model, the occupied and unoccupied continuous orbitals are referred to as the valence and conduction bands, respectively. The two bands are separated by a given energy, dubbed the band gap ($E_g$). Interestingly, this increase in conjugation also serves to lessen the $E_g$ by increasing and decreasing the valence and conduction band edges, respectively.[29] However, at a certain point this effect plateaus due to the “effective conjugation length”

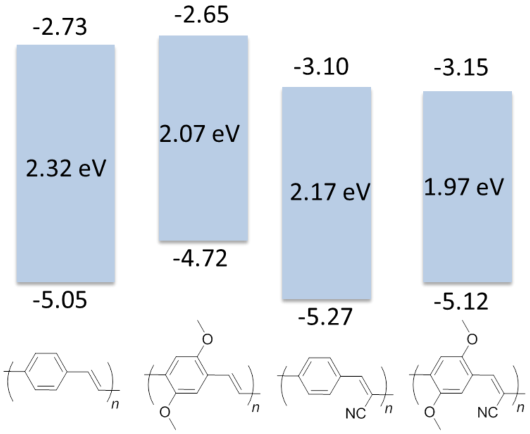

*Figure 1.2: HOMO, LUMO and $E_g$ of poly(para-phenylene vinylene) modified with donating and withdrawing groups*[35]

of the material – i.e. due to inherent disorder of organic systems, there exists a certain number of repeat units after which the carbon $p_z$ orbitals experience little overlap, which limits the delocalization of the electron cloud over the material. Additionally, any steric hindrance between monomer units leads to a torsional twist, which thereby limits the effective conjugation length and the $E_g$.[30-33]

Altering the number of repeat units of a polymer is only one way to control the polymer $E_g$. Unlike relatively intractable inorganic crystals, organic materials can be manipulated synthetically to modify the HOMO, LUMO, $E_g$, as well as other physical and electronic properties. For example, incorporating electron-donating or –withdrawing groups on an organic material will generate lower or higher HOMO and LUMO levels, respectively (Figure 1.2).[34-35] The relative depth of the HOMO and LUMO levels determine what the majority charge carrier in the material will be.[36] Most organic materials are "p-type" in that they have reasonably high HOMO and LUMO levels, meaning they readily conduct positive charge (holes).[37-40] Conversely, n-type organic materials are comparatively rare and preferentially conduct electrons and have very

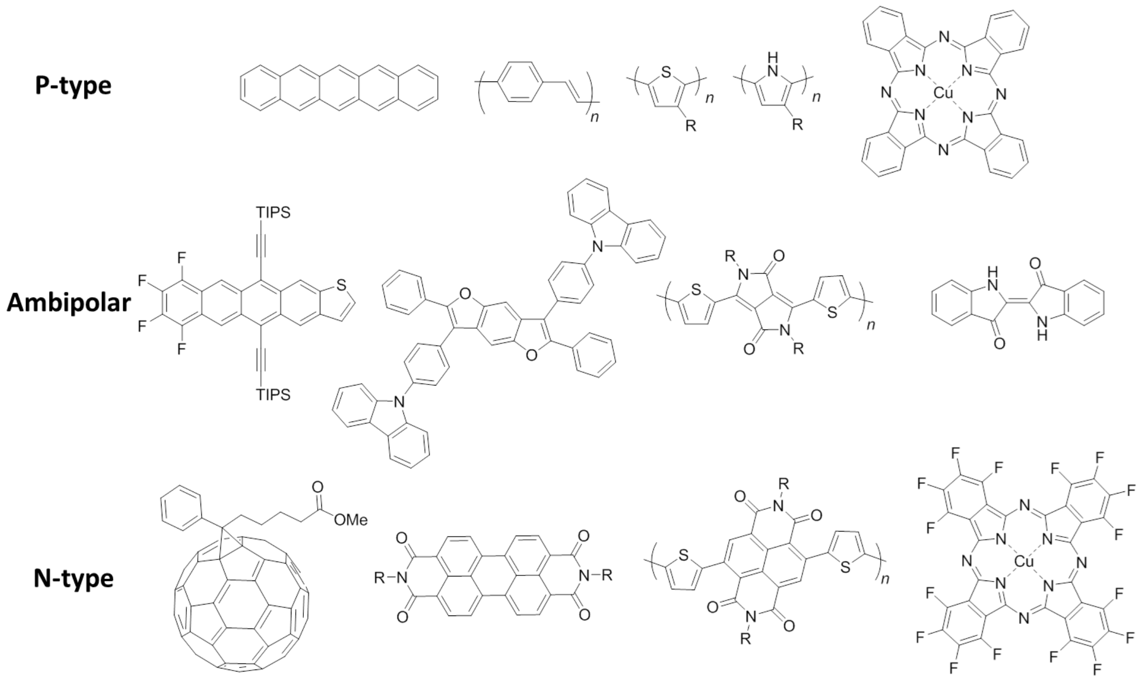

*Figure 1.3: Common p-type, n-type and ambipolar organic materials*

low HOMO and LUMO levels.[41-48] Generally, electron injection into p-type materials permanently damages them, as does hole injection in n-type materials. Additionally, organic materials that can conduct both electrons and holes are called ambipolar molecules.[49] Some common p-type, n-type and ambipolar materials are depicted in Figure 1.3.

### 1.2.1 Poly(3-alkylthiophenes)

One class of p-type semiconducting polymer that deserves special mention are poly(3-alkylthiophenes) (P3ATs). Since the first report of a soluble P3AT in 1986,[50] there has been intensive research on these materials, especially in the context of OPV.[51-60] Given that the 3AT monomer is asymmetric, there are three types of possible linkages between two thiophene units: head-to-head (HH), head-to-tail (HT), and tail-to-tail

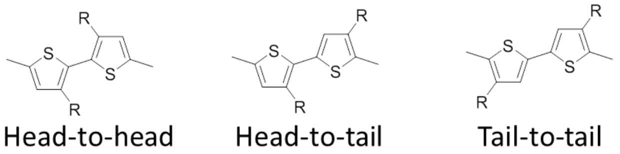

*Figure 1.4: Possible orientations of thiophene linkages*

(TT) (Figure 1.4).[61] There are a number of different ways to synthesize P3ATs; depending upon the method, the P3AT will either be regioregular (if nearly all linkages are HT) or regiorandom (if there is no selectivity in the orientation of the thiophene units). Both HH and TT linkages cause a torsional twist in the P3AT backbone, which limits the polymer crystallinity and decreases the conjugation length, both of which impair the electronic behavior of the P3AT. Conversely, highly regioregular P3ATs exhibit crystalline behavior, which enhances its hole mobility and redshifts its solid state absorbance.[62] The absorbance of P3ATs results from a π-π* transition, where electrons are excited from the bonding to the antibonding orbitals of the P3AT.[63] Historically, P3ATs have been investigated in the context of OPVs due to their ease of synthesis and interesting electronic properties. One of the most heavily studied P3ATs is poly(3-hexyl)thiophene (P3HT).

### 1.2.2 Donor-Acceptor Copolymers

One effective way to modify the HOMO and LUMO levels independently is to utilize a donor-acceptor (D-A) copolymer. These materials possess alternating electron-rich and electron-deficient monomers.[64-65] Due to the proximity of the monomers, internal charge transfer (ICT) occurs during photoexcitation. Thus, the HOMO tends to be dictated by the HOMO level of the electron-rich component while the LUMO is largely determined by the LUMO level of the electron-poor unit (Figure 1.5). In this way,

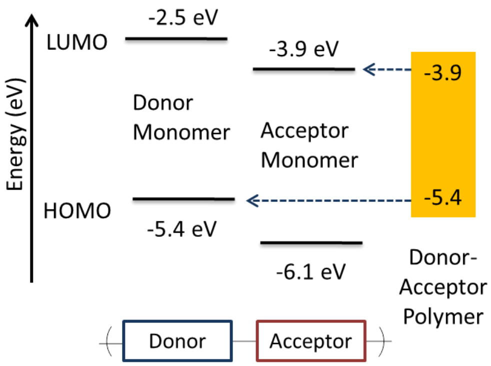

\

*Figure 1.5: Energy level diagram of donor/acceptor monomers and resultant donor-acceptor polymer*

the HOMO, LUMO and $E_g$ can be independently tuned to realize the optimal combination.[4]

Numerous combinations of electron rich (e.g. fluorene, carbazole, benzo[1,2-*b*:4,5-*b*']dithophene, etc.) and poor (e.g. thieno[3,4-*b*]thiophene, diketopyrrolopyrrole, etc.) monomers have been explored to generate low band gap D-A polymers.[66-81] These numerous permutations have yielded a rich library of conjugated donor-acceptor polymers with varying electronic characteristics.

## 1.3 Operating Principles of Organic Photovoltaics

### 1.3.1 Light Absorption

The delocalized electron cloud of conjugated organic materials imbue them with electronic properties not generally exhibited by organic materials, including free charge generation and transport. If a photon has energy equal to or larger than the $E_g$ of the light-harvesting electron donor component, it will promote an electron from the valence to the conduction band. Unfortunately, unlike inorganic materials, organic materials have a low dielectric constant, which arises because the electron cloud of organic materials is much

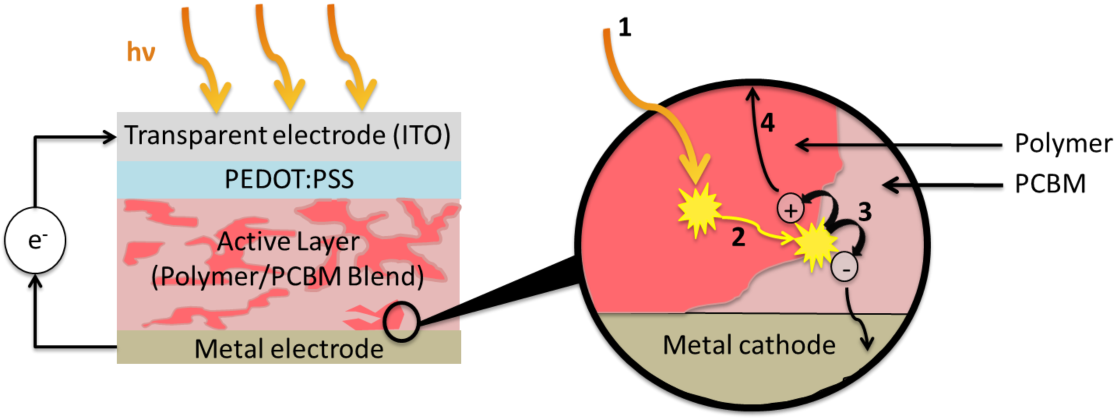

*Figure 1.6: Depiction of basic organic photovoltaic architecture and steps involved in charge collection: 1) light absorption, 2) exciton diffusion, 3) exciton dissocation, 4) charge collection*

more strongly associated to the carbon nuclei due to the small atomic radius of carbon.[82] This thereby limits the amount of electron shielding of the valence shell. Thus, upon light excitation, the excited electron is still coulombically bound to its positively-charged hole, generating an "exciton" (Figure 1.6).[82-84]

### 1.3.2 Exciton Diffusion

Once generated, the exciton will not dissociate spontaneously in ambient conditions; a driving force must make it favorable for the exciton to form free charge carriers. In this case, the driving force is the relative energy structures of the p-type donor material and n-type acceptor material, which favors the separation of the exciton into its constituent free charges. Thus, the exciton must diffuse through the donor domain to an interface with an acceptor domain.[85] It migrates between adjacent donor molecules via a "hopping" mechanism, whereby the exciton transitions between abutting localized energy states on different donor molecules.[86-88] The rate of this transport is dictated by how closely the electron clouds of neighboring donor molecules overlap (i.e. the spatial orientation of the donor molecules relative to one another), as well as the availability of states with similar energy levels on different molecules for the exciton to occupy.[88] Generally, if a given donor material has strong π-π interactions with itself, it will tend to have better charge transport properties.

Unfortunately, due to the large exciton binding energy (i.e. the coulombic attractive energy between the excited electron and hole), excitons have limited stability and exist for a finite amount of time before geminate recombination occurs (i.e. the excited electron recombines with its associated hole), resulting in an energy loss, which decreases the device PCE. The diffusion length of an exciton is dependent upon the electron-donating material, but generally varies between 5-20 nm.[89-90]

### 1.3.3 Exciton Dissociation

If the exciton is able to diffuse to an electron donor/acceptor interface prior to recombination, the offset between the donor/acceptor LUMO levels generates a favorable orbital energy structure that facilitates charge transfer of the excited electron to the acceptor material, while the positive charge remains localized on the donor material. To realize efficient exciton dissociation, the difference in energies between the donor and acceptor LUMO levels must be large enough to overcome the exciton binding energy.[85] Quantitative values for the exciton binding energy are disputed, but empirical values are generally found to be around 0.1 eV.[91]

### 1.3.4 Charge Collection

Following exciton scission, the holes and electrons percolate through the donor and acceptor domains, respectively, to reach their intended electrodes. The free charge carriers are funneled to their respective electrodes through the electric field potential built into the device that is created by using asymmetric electrode materials with different work functions.[92]

The free charge carriers migrate through the donor/acceptor domains at a rate that is described by the free charge carrier mobility ($\mu$) of the material; the higher the $\mu$, the faster the charges migrate. The rate at which the charges reach the electrodes is important because these free charge carriers must be transported to the charge collecting electrodes before bimolecular recombination occurs – i.e. when a positive and negative charge in the process of traveling to their respective electrodes meet at a donor/acceptor interface and subsequently recombine.[93] Ideally, to limit bimolecular recombination as much as possible, the donor and acceptor materials should have roughly equal hole ($\mu_h$) and electron ($\mu_e$) mobilities.[94]

### 1.3.5 Organic Photovoltaic Architectures

The first bilayer OPV cell (Figure 1.7) comprised a layer of p-type copper phthalocyanine light-harvesting donor overlaid with a layer of perylene tetracarboxylic anhydride n-type electron acceptor sandwiched between transparent indium tin oxide (ITO) and metallic electrodes.[95] This electron donor/acceptor layer is called the active layer. The planar junction between the donor and acceptor materials leads to a low interfacial surface area between them and limits exciton dissocation efficiency; any excitons generated further than ~20 nm from the planar donor/acceptor interface will undergo geminate recombination.[96] However, following exciton scission, there are continuous neat donor/acceptor films that lead to the electrodes, thereby limiting bimolecular recombination.

The PCE values of OPV cells increased dramatically after the introduction of the

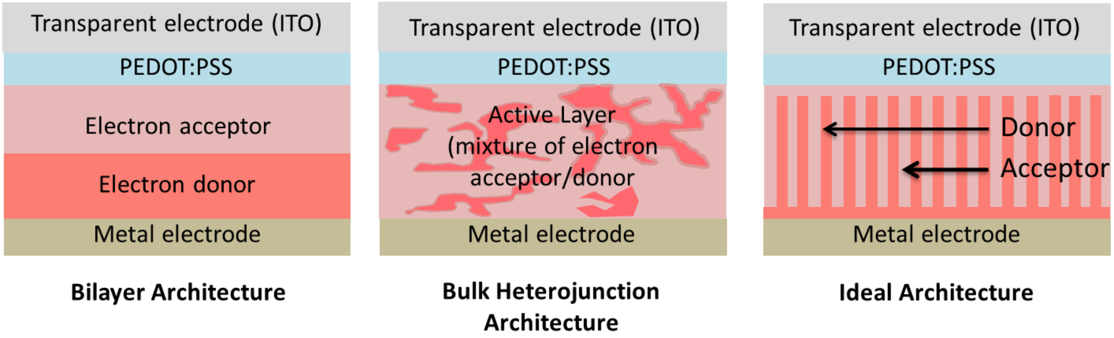

*Figure 1.7: Bilayer, bulk heterojunction and nanostructured OPV architectures*

bulk hetero-junction (BHJ) active layer architecture.[97-100] In contrast to bilayer OPV devices, the BHJ active layer is formed by co-depositing the electron donor and acceptor from the same solution. This forms a bicontinuous interpenetrating network of the donor and acceptor materials. This network generates higher interfacial areas and can help limit geminate recombination losses. However, the random nature of the BHJ leads to areas within the active layer that are “dead-ends” for charge transport, which leads to bimolecular recombination.

Given the limited diffusion length of the exction, the ideal architecture would have a nanostructured active layer that has features on the order of the exciton diffusion length. Thus, most excitons formed would reach a donor/acceptor interface.

### 1.3.6 Measuring Organic Photovoltaic Performance

In order to maximize the PCE of OPV devices, several interrelated parameters describing the device must be maximized. PCE, which is the ratio between the energy extracted from the PSC and the total solar energy incident upon the cell, is calculated by the following equation:[101]

$$\eta = \frac{(V_{oc})(J_{sc})(FF)}{P_{in}}$$

where $V_{oc}$ is the open-circuit voltage, $J_{sc}$ is the short-circuit current density, FF is the fill factor and $P_{in}$ is the incident solar energy (Figure 1.8). Although these parameters are dependent on many aspects of the OPV, the light-harvesting polymer is instrumental in determining the PCE. The $J_{sc}$ represents the current flow of the device under illumination, without an applied voltage. This is affected by the efficiency of generating and collecting charges in the solar cell, which is dependent upon the $E_g$, $\mu$, and the exciton dissociation efficiency.[102] The $V_{oc}$ represents the voltage necessary to stop charge flow under illumination. Generally, the $V_{oc}$ is directly proportional to the energy difference between the HOMO of the donor material and the LUMO of the electron accepting material.[103] Finally, the FF is the ratio between the actual attainable power and the theoretical attainable power and relates to parasitic losses in the OPV.[104]

To achieve the highest possible PCE, the $V_{oc}$, $J_{sc}$ and FF should be maximized. However, the parameters are limited by energy level requirements in the OPV cell. $V_{oc}$ and $J_{sc}$ are generally inversely proportional. To maximize $J_{sc}$, the light absorption must be maximized. Thus, the $E_g$ should be small to harvest as many photons as possible. To do this, the donor LUMO must be decreased and/or the HOMO must be increased. However, as the HOMO increases, the difference between the donor HOMO and acceptor LUMO decreases, thereby decreasing the $V_{oc}$. Additionally, to achieve efficient exciton dissociation, the donor LUMO level is dictated by the acceptor LUMO level and the exciton binding energy.

Thus, the light absorption of the donor must to be optimized to collect as much light as possible (increasing $J_{sc}$). Simultaneously, the donor needs to have as deep a

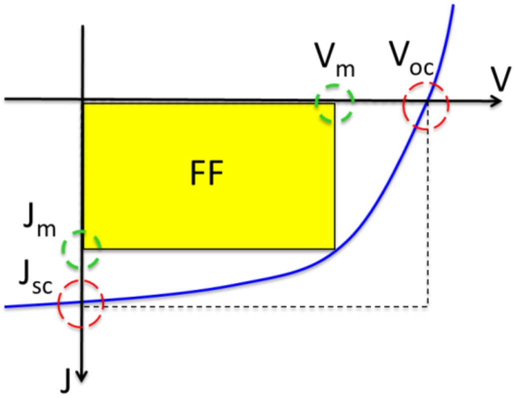

*Figure 1.8: Representative current-voltage curve of a solar cell under illumination. The $V_{oc}$, $J_{sc}$, $V_m$, $J_m$ and FF are highlighted.*

HOMO as possible to maintain a high $V_{oc}$. If the $E_g$ is too large, the material will be transparent to lower energy photons; on the other hand, if the $E_g$ is too small, the excess energy of high-energy photons will be lost through infrared radiation. According to theoretical studies, an optimal light-harvesting material will possess an $E_g$ of ~1.5 eV, with a LUMO ca. -4 eV and a HOMO ca. -5.5 eV.[105] The best way to achieve precise control over the HOMO, LUMO and $E_g$ of a polymer is to utilize D-A structures in donor materials.

## 1.4 Synthesis of Semiconducting Polymers

There are a variety of ways to synthesize semiconducting polymers, which can be grouped into two broad categories: step-growth and chain-growth polymerizations.[106-107] The resultant polymers are characterized by several parameters. The number average molecular weight ($M_n$) is a statistical average determined by taking the total weight of the polymer mixture divided by the number of polymer chains. $M_n$ is calculated by the following equation:[108]

$$M_n = \frac{\Sigma N_i M_i}{\Sigma N_i}$$

where $N_i$ is the number of polymers of a given weight and $M_i$ is the mass of the polymer. Alternatively, the weight average molecular weight ($M_w$) is a weighted average accounting for the weight of each polymer chain. It is calculated from the following equation:[108]

$$M_w = \frac{\Sigma N_i M_i^2}{\Sigma N_i M_i}$$

Finally, polymers can also be characterized by their dispersity (Đ), which is a measure of the heterogeneity of the polymer mixture; this is calculated by dividing $M_w$ by $M_n$. If all the polymer chains in a mixture have identical molecular weights, Đ is equal to one. If the mixture contains polymers of disparate molecular weights, Đ is greater than one.[109]

### 1.4.1 Step-growth Polymerization

The most common way to synthesize semiconducting polymers is via step-growth polymerizations (Figure 1.9). Broadly speaking, this involves the random coupling of monomers, dimers, oligomers and polymers to form long-chain polymers. Each monomer has two or more reactive sites. These reactive sites can have the same or disparate chemical functionalities.

In practice, step-growth polymerizations are difficult to control. This arises from the random coupling of monomers, oligomers and growing polymer chains in solution. This leads to a wide distribution of molecular weights; Đ for step-growth polymerizations is often greater than two.[106] Classes of step-growth polymerizations discussed herein are Stille and Suzuki polymerizations. These are frequently used for the synthesis of D-A polymers.

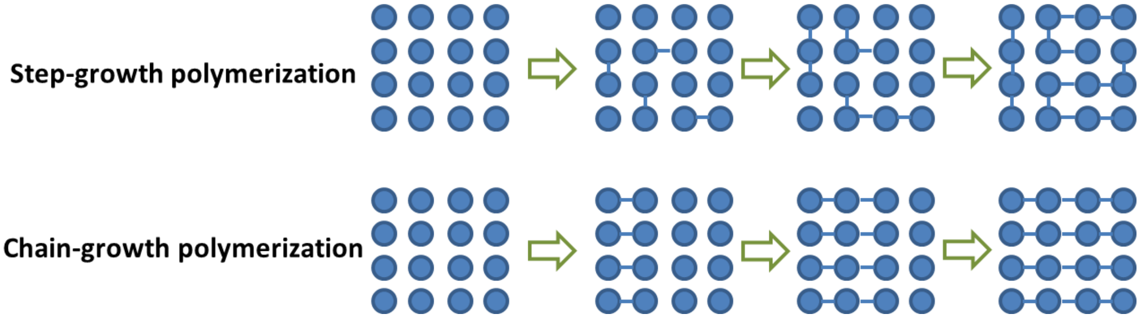

*Figure 1.9: Illustration of progression of polymer growth for step-growth and chain-growth polymerizations*

### 1.4.2 Chain-growth Polymerization

Chain-growth polymerization is markedly different from step-growth polymerization in that it consists of three distinct phases: 1) initiation, 2) propagation and 3) termination. Chain initiation is typically started using an initiator – e.g. an organic compound with a labile functional group. Propagation occurs when new monomers add to the growing polymer chain. Finally, chain termination can occur in a variety of ways. It can either occur purposefully by adding a quenching agent or incidentally through disproportionation where two growing chains combine to form a single polymer. The active center of the growing polymer chain can either be a cation, anion or radical and is located at the growing terminus of the polymer. The defining feature of chain-growth polymerizations is that monomers are added to each growing polymer sequentially.[110] If performed carefully, this yields a polymer mixture with low Đ.[111-114]

Compared to step-growth polymerizations, chain-growth polymerizations are less often used to synthesize semiconducting polymers. The most common form of chain-growth polymerization in this context is Kumada catalyst transfer polycondensation (KCTP).

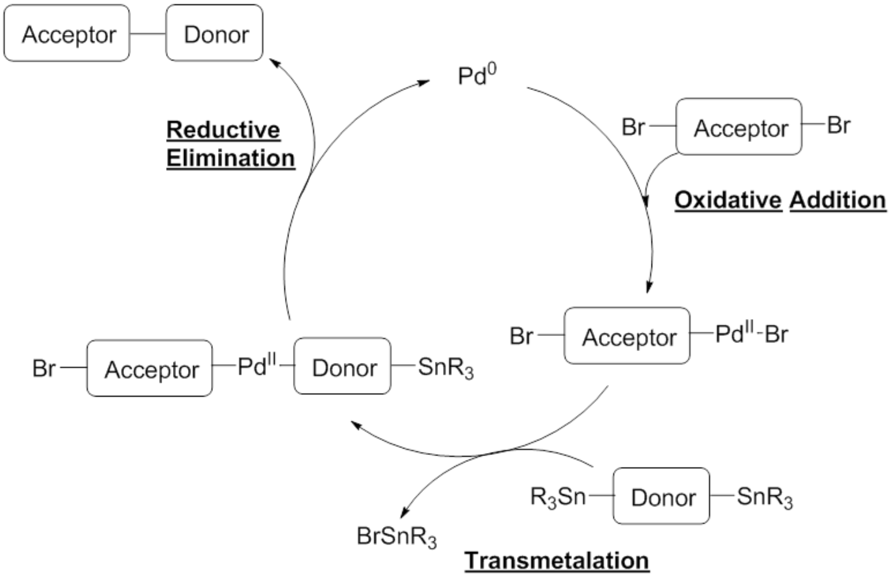

*Figure 1.10: Catalytic cycle for typical Stille polymerization of a conjugated polymer*

### 1.4.3 Stille Polymerization

The Stille reaction is a C-C bond forming reaction catalyzed by a palladium catalyst. The widely used conditions for the Stille coupling were developed by John Stille and David Milstein in 1978, in which an acid chloride and organotin compound were coupled via a palladium catalyst.[115] In the intervening years, the Stille coupling has been expanded to aromatic halides (or pseudohalides) and organotin compounds to form conjugated C-C bonds.[116-121] It can also be applied to polymerizations by utilizing symmetric difunctionalized organotin and halogenated aromatic compounds.[122-125]

The catalytic cycle of the Stille reaction (Figure 1.10) starts with the oxidative addition of the aromatic halide to the palladium(0) catalyst, thereby forming a palladium(II) complex. This step is followed by a transmetalation step with the organotin compound, followed by a reductive elimination step to yield the final C-C bond and to regenerate the palladium(0) species. In the case of a Stille polymerization, the reaction occurs at both ends of the growing chain.[126]

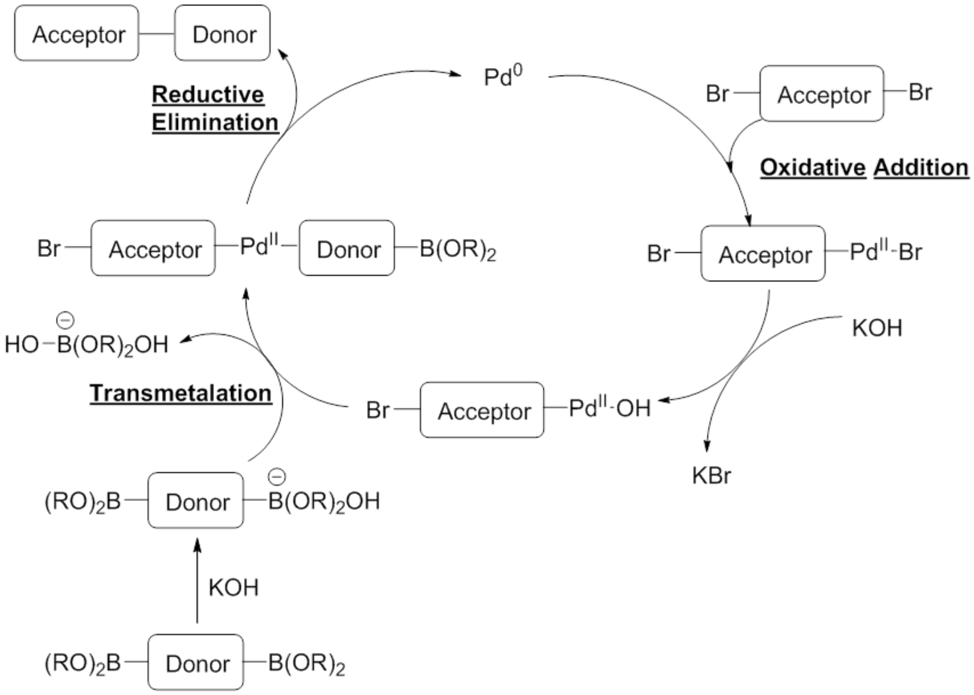

*Figure 1.11: Catalytic cycle for typical Suzuki polymerization of a conjugated polymer*

### 1.4.4 Suzuki Polymerization

The Suzuki reaction is a very similar reaction to the Stille reaction and was pioneered by Akira Suzuki in 1979.[127-128] This is also a C-C bond forming reaction catalyzed by a palladium catalyst and can be viewed mechanistically in terms of sequential oxidative addition, transmetalation and reductive elimination steps (Figure 1.11).[129] However, the Suzuki coupling exploits a boronic ester/acid instead of an organotin compound. Additionally, a base is required for two reasons: one, to undergo ligand exchange with the palladium halide complex, and two, to form a trialkyl borate, which activates the boronic ester/acid compound for the transmetalation step.[130-131]

### 1.4.5 Kumada Catalyst Transfer Polycondensation

The KCTP reaction has been used historically to synthesize polythiophenes. It was developed independently by both the McCullough and Yokozawa groups to synthesize highly regioregular P3HT with narrow Đ.[132-135] Broadly speaking, a nickel(II)

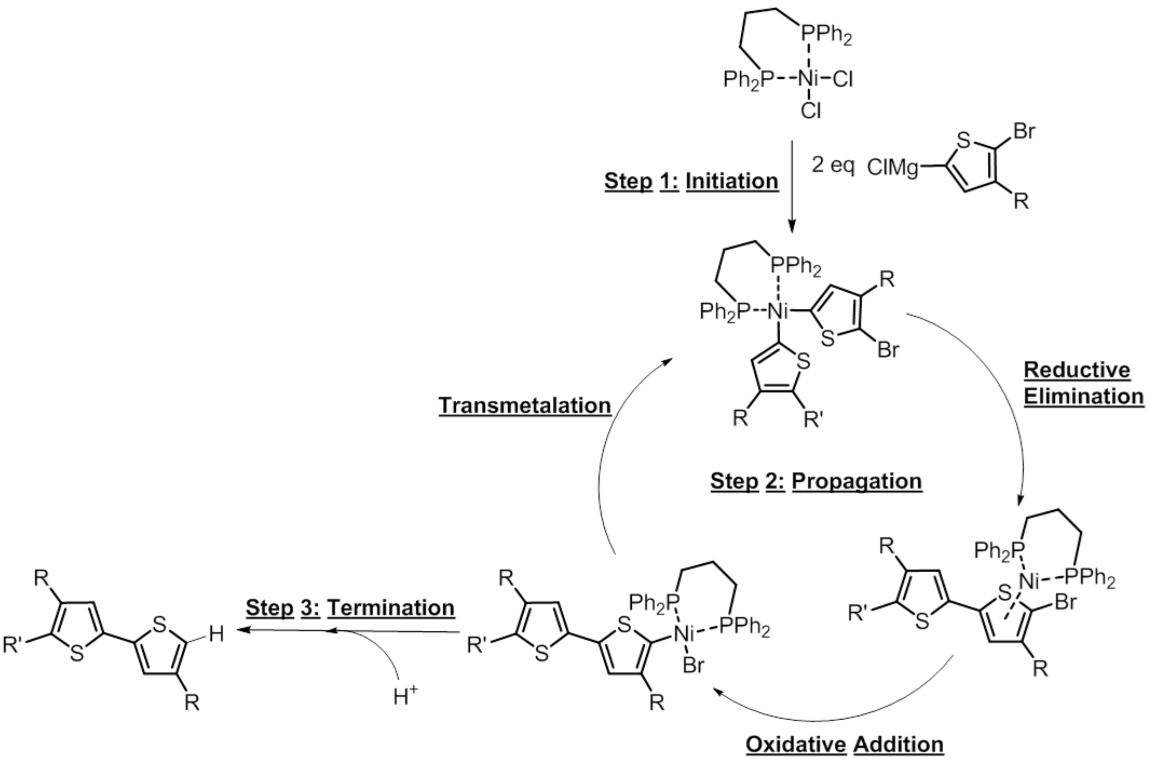

*Figure 1.12: Kumada catalyst transfer polycondensation catalytic cycle*

catalyst is added to a solution of Grignardized thiophene monomer (typically 2-bromo-5-chloromagnesio-3-hexylthiophene). The nickel undergoes two transmetallation steps involving the Grignard-type monomers, followed by a reductive elimination step to yield a thiophene-thiophene bond. From thence, the newly generated nickel(0) species migrates across one thiophene ring and undergoes oxidative addition to the terminal aryl halide bond to complete the catalytic cycle (Figure 1.12).[136] In this way, each nickel atom is associated with a growing P3HT chain in a chain-growth polymerization, keeping Đ characteristically low. Moreover, because one catalyst complex forms one polymer chain, the molecular weight of the P3HT can be predetermined by using different nickel to monomer ratios.[135]

The nature of the nickel catalyst is important to the efficacy of the KCTP polymerization. Bidentate ligands (e.g. 1,2-bis(diphenylphosphino)propane (dppp)) force the two nickel-bound thiophene rings into a *cis* configuration around the metal center which is necessary for reductive elimination.[137-139] Also, the coordination of the nickel atom to the thiophene ring, the subsequent selective intramolecular oxidative addition to the neighboring thiophene-halide bond and the fact that the intramolecular oxidative addition occurs more quickly than the dissociation of the nickel-polymer complex are all essential to realize low Đ and high molecular weights.[136]

# 2. Tunable Light-Harvesting Polymers Containing Embedded Dipolar Chromophores for Organic Photovoltaic Applications

## 2.1 Introduction

As stated above, there are several interconnected requirements for the design of a given electron donating material for an OPV device. A significant amount of research has focused on the molecular engineering of linear D-A copolymers to tune their $E_g$ and energy levels to enhance OPV performance. The characteristics of the monomers dictate the electronic properties of the polymer. Although this method can theoretically be used to optimize the electronic attributes of light-harvesting polymers, it is difficult to predict the characteristics of a polymer comprised of a given combination of electron-rich and –poor monomers. Computer modeling is the best way to predict the characteristics of an unknown monomer combination.[140] Moreover, after a D-A copolymer is synthesized there is no way to systematically fine-tune the energy levels because this would require parallel syntheses of modified donor and/or acceptor monomers and polymerization reactions. Given the poor reproducibility of step-growth polymerizations, this leads to inconsistent electronic properties across different polymer batches.[141]

To address this issue, several groups have explored the development of tunable D–$\pi$-bridge–A polymers for OPV applications.[142-146] The D–$\pi$-bridge–A motif is common to many second-order nonlinear optical (NLO) chromophores. This architecture exploits well-established knowledge of the structure/property relationships and charge transfer in NLO dyes, which can greatly decrease their $E_g$.[147-149] Unlike common D-A copolymers in which the acceptors and donors lie linearly along the backbone of the polymer chain, the acceptors of D–$\pi$-bridge–A polymers terminate the electron-poor side chains, which are connected through a $\pi$-bridge to an electron-rich conjugated backbone.[142-146]

There have been several reports of D–$\pi$-bridge–A polymers consisting of triphenylamine (TPA) donors with vinylene $\pi$-bridges that can be used to fabricate efficient OPVs.[142-146,150-154] In each case, the $\pi$-bridge was terminated with an aldehyde that was further condensed with a range of acceptors after polymerization. Post-functionalization represents a flexible and generally applicable method to easily tune the electronic and optical properties of the polymers and to probe structure/property relationships of the polymers. Despite there being several reports on D–$\pi$-bridge–A polymers, these materials have very similar properties and weaknesses.

Importantly, the phenyl-phenyl backbone linkages of these polymers are inherently problematic because the phenyl-phenyl bonds in the backbone experience severe torsional rotation due to the steric hindrance between phenyl protons.[155] Thus, the electron-rich backbone tends to be electronically isolated from the electron-poor side chain, which leads to a low wavelength $\pi$-$\pi$* transition absorbance that is significantly more intense than the longer wavelength internal charge transfer (ICT) transition absorbance between TPA and the side chain acceptor. The resultant absorbance profile overlaps poorly with the solar spectrum, which decreases OPV performance.[156]

To further investigate the structure-property relationships of these polymers, a new class of D–$\pi$-bridge–A polymer, consisting of a thiophene-TPA backbone with indacenodithiophene $\pi$-bridge (PThTPA-IDT), was synthesized and functionalized with three acceptors (Figure 2.1).[157] It was theorized that inclusion of thiophene in the polymer

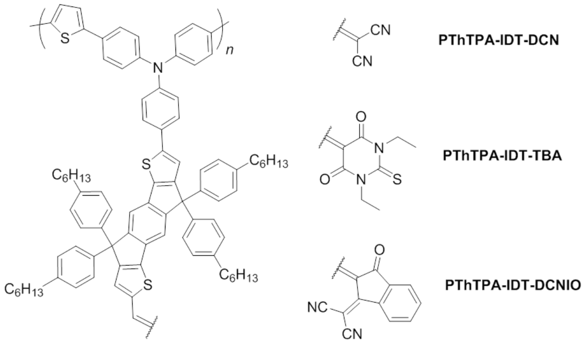

*Figure 2.1: Structure of target side chain polymers*

backbone would increase the planarity of the polymer backbone and thereby increase the relative intensity of the ICT absorbance. Also, since conjugated polymers based on the IDT monomer have previously exhibited high PCE[158-159] and mobilities ($10^{-1}$ to $10^{-2}$ $cm^2$ $V^{-1}$ $s^{-1}$)[160-161], despite the bulky side chains of the IDT donor, it was hoped that incorporating the fused IDT unit as the polymer $\pi$-bridge could provide adequate carrier mobility and charge transfer properties, while also enhancing the polymer solubility through the peripheral hexylbenzyl groups.

## 2.2 Synthesis

General synthesis of the TPA-IDT monomer and PThTPA-IDT are shown in Scheme 1. The IDT unit was prepared as reported previously.[162] The IDT molecule was then monoformylated in moderate yield via the Vilsmeier-Haack reaction and then brominated with NBS to give **2**. Concurrently, triphenylamine was monobrominated using NBS to yield **3**, which was lithiated and quenched with trimethyltin chloride to generate **4**. Then, **2** and **4** were coupled via a Stille reaction to yield **5**, which was then dibrominated with NBS. Copolymer PThTPA-IDT-CHO was synthesized by Stille cross-

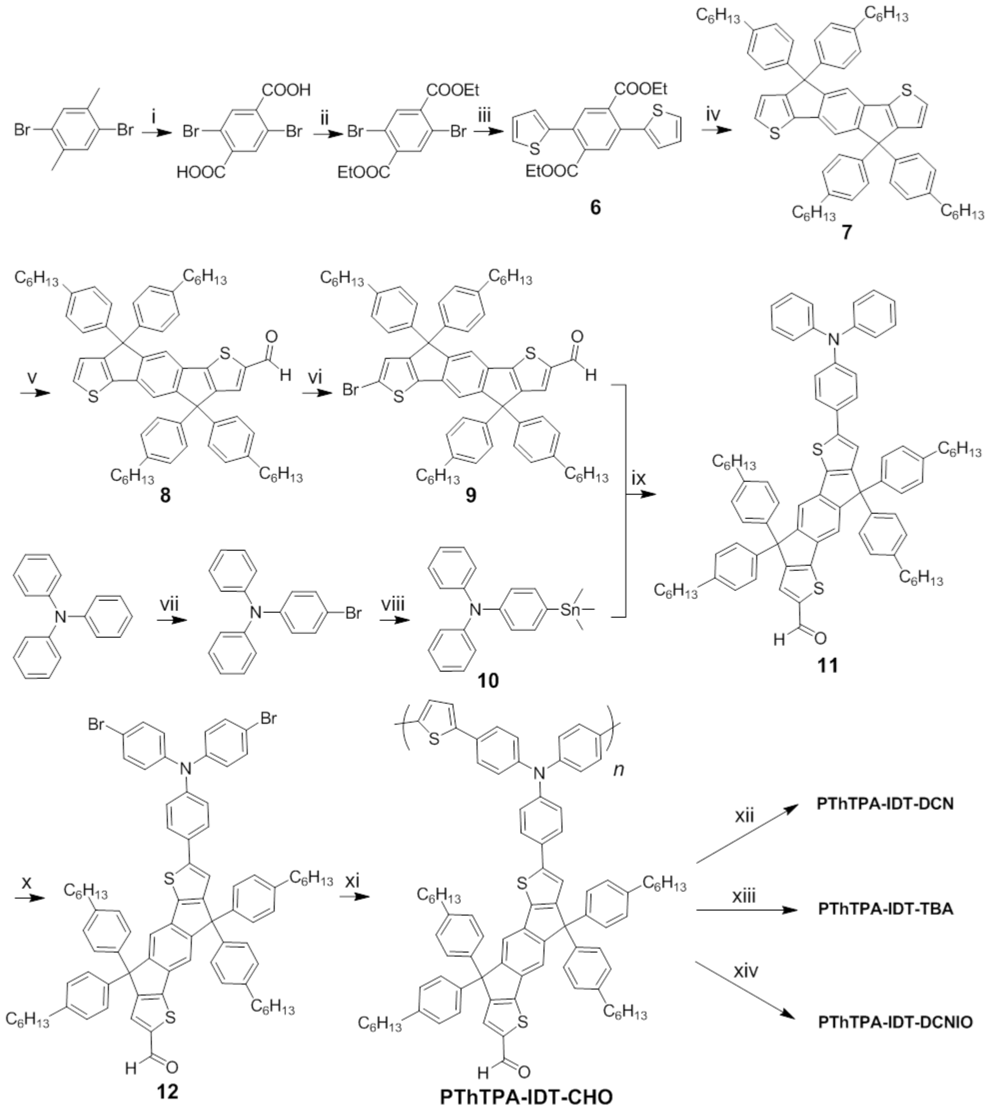

*Scheme 1: Synthesis of PThTPA-IDT polymers. i) $KMnO_4$, $H_2O$, pyridine, reflux, 8h; ii) EtOH, $H_2SO_4$, toluene, reflux, 10h; iii) 2-trimethylstannylthiophene, $Pd_2(dba)_3$, $P(o\text{-}tol)_3$, THF, reflux, 16h; iv) (a) n-BuLi, 4-hexyl-1-bromobenzene, THF, -78˚C, 1h, (b)* ***6****, THF, rt, 16h, (c) $H_2SO_4$, acetic acid, reflux, 2h; v) $POCl_3$, DMF, 0˚C to rt; vi) N-bromosuccinimide, THF, 12h, r.t.; vii) N-bromosuccinimide, THF, 12h, 0˚C; viii) (a) n-BuLi, THF, -78˚C, 1h, (b) $ClSnMe_3$, hexane, 12h; ix)* ***7****, $Pd_2(dba)_3$, $P(o\text{-}tol)_3$, THF, reflux, 16h; x) N-bromosuccinimide, THF, 12h, r.t.; xi) 2,5-bis(trimethylstannyl)thiophene, $Pd(PPh_3)_4$, toluene, DMF, 110˚C, 48h; xii) malononitrile, $CHCl_3$, pyridine, 50˚C, 16h; xiii) 1,3-diethyl-2-thiobarbituric acid, $CHCl_3$, pyridine, 50˚C, 16h; xiv) 3-dicyanomethylene-1-indanone, $CHCl_3$, pyridine, 50˚C, 16h.*

coupling between compound 12 and 2,5-bis(trimethylstannyl)thiophene, using tetrakis(triphenylphosphine)palladium(0) ($Pd(PPh_3)_4$) as a catalyst in a toluene/DMF solution. The polymerization was carried out at 110 °C under nitrogen atmosphere for 48 h. The resulting polymers were collected by precipitating the reaction solution in methanol followed by filtration. After Soxhlet extraction with acetone, hexane and methanol for 12 h each, the final polymer was collected by extraction with $CHCl_3$and the resultant solution was precipitated in methanol. This polymer was then functionalized with malononitrile (DCN), 1,3-diethyl-2-thiobarbituric acid (TBA) and 3-dicyanomethylene-1-indanone (DCNIO) acceptors via a Knoevenagel condensation to yield their respective polymers.

### 2.3 Results and Discussion

#### 2.3.1 Polymer Characterization

The polymers all have good solubility in a wide range of organic solvents including tetrahydrofuran, dichloromethane, chlorobenzene, and dichlorobenzene. The molecular weights of the two polymers were measured by GPC with polystyrene as standard and THF as eluent. The number-average molecular weights ($M_n$) of PThTPA-IDT-DCN, PThTPA-IDT-TBA, and PThTPA-IDT-DCNIO are 22.0, 21.7, and 22.1 kDa with Đ of 1.90, 1.87 and 1.91, respectively. Due to the improved solubility of PThTPA-IDT, $M_n$ is roughly twofold higher than what has previously been reported for D–$\pi$-bridge–A polymers. This improved solubility is attributed to the solubilizing IDT unit.

The thermal properties of these polymers were evaluated using differential scanning calorimetry (DSC, Figure 2.2). All three PThTPA-IDT polymers exhibit two identical glass transition temperatures ($T_g$) around 70 and 100 °C (Figure 2), which correspond to the $T_g$ for the solubilizing alkyl chains and the polymer backbone, respectively. This amorphous behavior is expected based on the propellor-like twist of

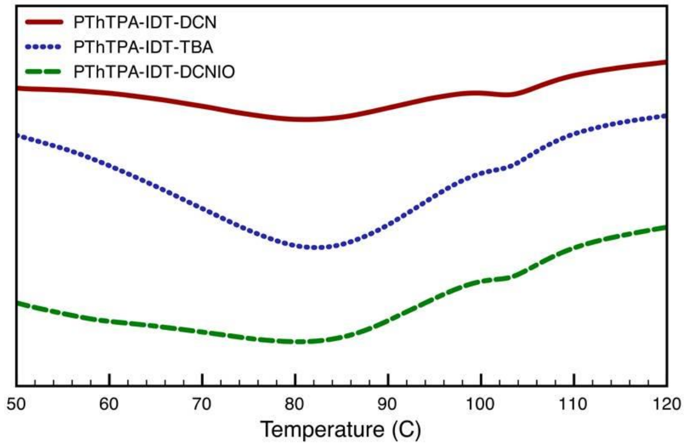

*Figure 2.2: DSC scans for PThTPA-IDT polymers*

the triphenylamine moiety, which inhibits intermolecular *π*-*π* packing and prohibits crystalline behavior.[163]

The UV-visible absorption spectra of the polymers in $CHCl_3$ solutions and thin films are shown in Figure 2.3 and the summarized data is listed in Table 2.1. The absorption maxima in chloroform solution were observed at 445, 581 and 639 nm for PThTPA-IDT-DCN, PThTPA-IDT-TBA, and PThTPA-IDT-DCNIO, respectively. The peaks of the thin film absorption are slightly broadened compared to the solution peaks, but otherwise are identical. As expected for amorphous materials, the spectra show no evidence of strong intermolecular packing. The absorption coefficients were calculated from the solid state absorbance and are $1.11 \times 10^5$ $cm^{-1}$, $0.87 \times 10^5$ $cm^{-1}$ and $0.86 \times 10^5$ $cm^{-1}$for PThTPA-IDT-DCN, PThTPA-IDT-TBA, and PThTPA-IDT-DCNIO, respectively. Two obvious absorption bands are observed for the polymers in films and solutions. The shorter wavelength absorbance can be assigned to the backbone *π*-*π** transition while the longer-wavelength absorption band is attributed to ICT from the electron-rich backbone through the *π*-bridge to the electron-deficient side chain acceptors. Similar to reported

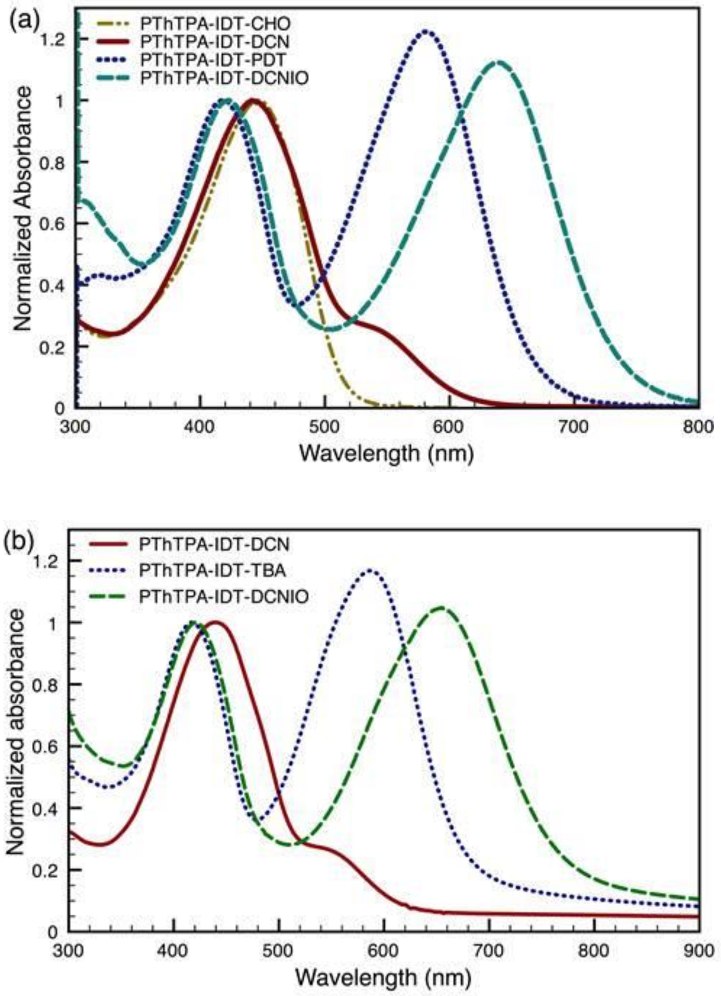

*Figure 2.3: a) Solution absorption spectra (with PThTPA-IDT-CHO in yellow for comparison) and b) thin film absorption spectra of PThTPA-IDT polymers*

D–$\pi$-bridge–A polymers, stronger electron acceptors decrease $E_g$ and redshift the ICT absorption peak by increasing the polymer LUMO level.[142-146,150-154]

Interestingly, PThTPA-IDT-DCN exhibits a very weak ICT shoulder on the main $\pi$-$\pi$* transition peak instead of the full ICT peak as displayed by PThTPA-IDT-TBA and PThTPA-IDT-DCNIO. This unusual phenomenon suggests that the DCN acceptor is not strong enough to pull electrons from the polymer backbone through the $\pi$-bridge and

*Table 2.1: Optical, physical and electronic properties of PThTPA-IDT polymers*

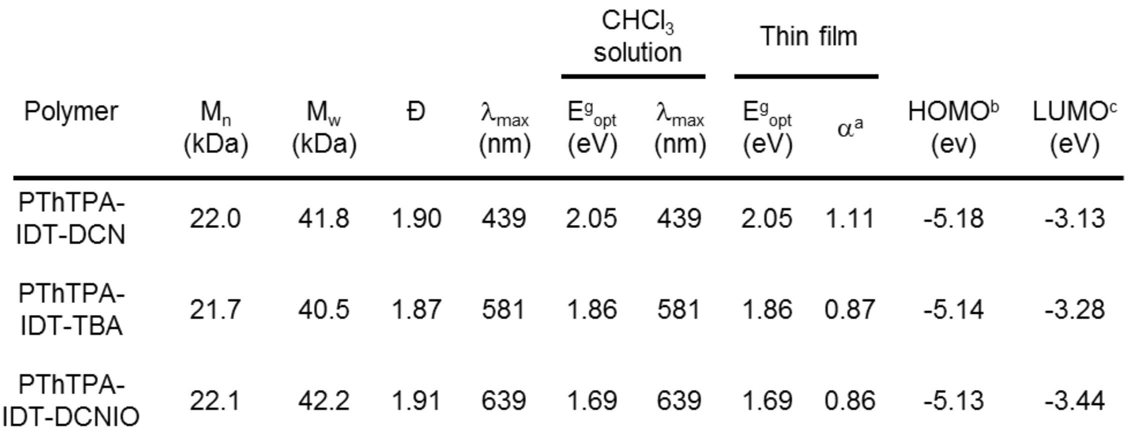

| | | | | | $CHCl_3$ solution | | Thin film | | | |
|---|---|---|---|---|---|---|---|---|---|---|
| Polymer | $M_n$ (kDa) | $M_w$ (kDa) | Đ | $\lambda_{max}$ (nm) | $E^g_{opt}$ (eV) | $\lambda_{max}$ (nm) | $E^g_{opt}$ (eV) | $\alpha^a$ | $HOMO^b$ (ev) | $LUMO^c$ (eV) |
| PThTPA-IDT-DCN | 22.0 | 41.8 | 1.90 | 439 | 2.05 | 439 | 2.05 | 1.11 | -5.18 | -3.13 |
| PThTPA-IDT-TBA | 21.7 | 40.5 | 1.87 | 581 | 1.86 | 581 | 1.86 | 0.87 | -5.14 | -3.28 |
| PThTPA-IDT-DCNIO | 22.1 | 42.2 | 1.91 | 639 | 1.69 | 639 | 1.69 | 0.86 | -5.13 | -3.44 |

[a]*Absorption coefficient of thin films at* $\lambda_{max}$ *(x* $10^5$ $cm^{-1}$*).* [b]*HOMO calculated from the oxidation onset of the cyclic voltammetry curve.* [c]*LUMO calculated from HOMO and optical band gap.*

form a stable ICT state. This is attributed to the high aromatic stabilization energy of the IDT unit, making the formation of an ICT state energetically unfavorable. The absorbance profile suggests that there is a threshold acceptor strength that is sufficient to funnel charge through the IDT *π*-bridge by stabilizing the ICT state and the DCN acceptor does not possess this threshold electron-withdrawing strength. In contrast, both TBA and DCNIO have sufficient electron withdrawing strength to stabilize the ICT state of the IDT *π*-bridge. In addition, both the TBA and DCNIO acceptors blueshift the *π*-*π** transition peak by ~25 nm, while the DCN acceptor does not cause a similar hypsochromic shift. This *π*-*π** peak shift also does not occur in any existing D–*π*-bridge–A polymers. Although this shift is not fully understood, it is attributed to the fact that these acceptors pull electron density away from the electron-rich backbone via the IDT *π*-bridge to form a CT state. This CT state stabilizes the polymer HOMO, effectively increasing the *π*-*π** transition energy. If this is accurate, the shift is not seen in other D–*π*-bridge–A polymers because there is very poor electronic communication between the polymer backbone and the side chain; thus, regardless of its electron-withdrawing strength, the acceptor is unable to pull electrons away from the electron-rich backbone.

Encouragingly, the ratio of the low-energy $\pi$-$\pi$* ICT peak intensity to the high-energy backbone $\pi$-$\pi$* transition peak intensity of PThTPA-IDT-TBA and PThTPA-IDT-DCNIO (~1.2:1) is much larger than that of previous D–$\pi$-bridge–A polymers (~0.5:1), which leads to better overlap with the solar spectrum. This increase in relative ICT intensity is attributed to the inclusion of thiophene in the polymer backbone. It is known that phenyl-thiophene linkages are more planar than phenyl-phenyl bonds due to the minimized steric hindrance between adjacent aromatic protons.[164] In addition, thiophene has a lower aromatic stabilization energy than benzene,[165] which should improve the electron delocalization along the backbone and the electronic communication between the polymer backbone and side chain acceptor.

This hypothesis was corroborated by density functional theory (DFT)[166-168] calculations at the B3LYP/6-31G* level (Figure 4).[169-171] Although DFT often overestimates theoretical energy levels, the B3LYP/6-31G* method has been found to be an accurate formalism for predicting the optical and geometrical properties of conjugated polymers.[172] The optimized geometry (Figure 2.4) shows that the dihedral angle between the thiophene monomer and the TPA phenyl rings is ~22°. Conversely, the phenyl-phenyl linkages of PFTPA exhibit a dihedral angle of ~36°. Due to this twist, the PFTPA HOMO orbitals are interrupted by the fluorene monomers and the polymer has a relatively short effective conjugation length. In contrast, since the thiophene-TPA linkage is relatively planar, the HOMO orbitals delocalize along the polymer backbone and enhance the effective polymer conjugation length.

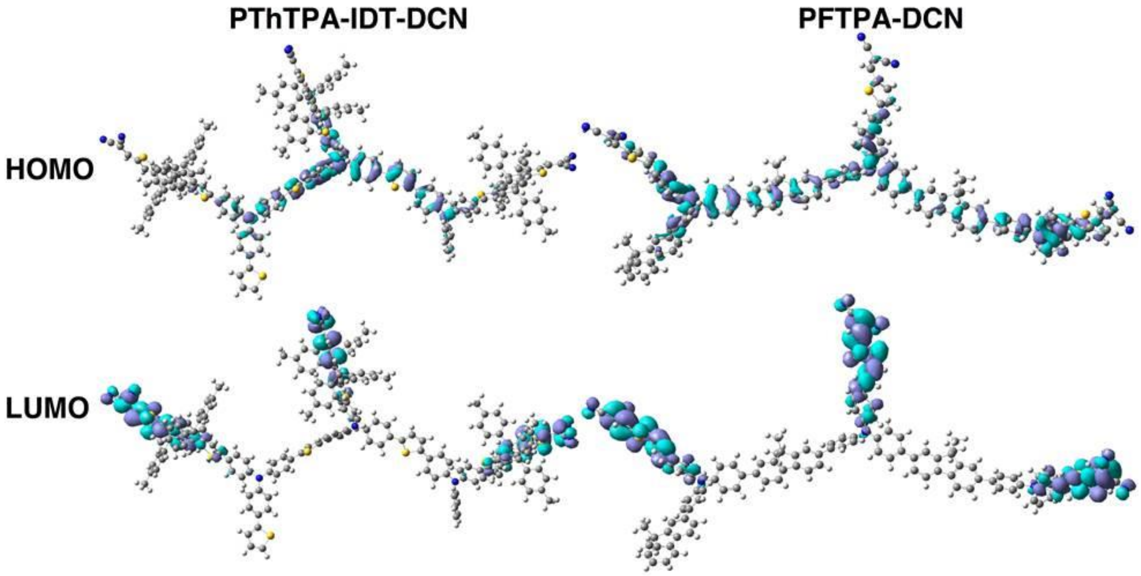

*Figure 2.4: Molecular orbital representations of HOMO and LUMO for PThTPA-IDT-DCN and previously reported PFTPA-DCN*[142]

Contrary to the striking differences in the polymer HOMOs, the LUMO levels are quite similar. In both cases, the LUMO is almost entirely localized on the side chain and acceptor. There is negligible overlap of the HOMO and LUMO orbitals. This poor orbital overlap in the PThTPA-IDT polymers indicates that any change in the electronic nature of the acceptor will have a large effect on the polymer LUMO and a very minimal effect on the polymer HOMO. This poor spatial overlap likely leads to a weak ICT oscillator strength and could explain why the ICT transition is less intense compared to typical linear D-A polymers.[173]

The HOMO and LUMO levels of the PThTPA-IDT polymers were investigated using cyclic voltammetry (CV) of polymer films on indium tin oxide (ITO) substrates in a 0.1 M $Bu_4NPF_6$ acetonitrile solution at a scan rate of 50 mV/s using a platinum electrode and an $Ag/Ag^+$ (0.1 M $AgNO_3$ in acetonitrile) electrode as the work and reference electrodes, respectively. The CV curves are shown in Figure 2.5 and the data is

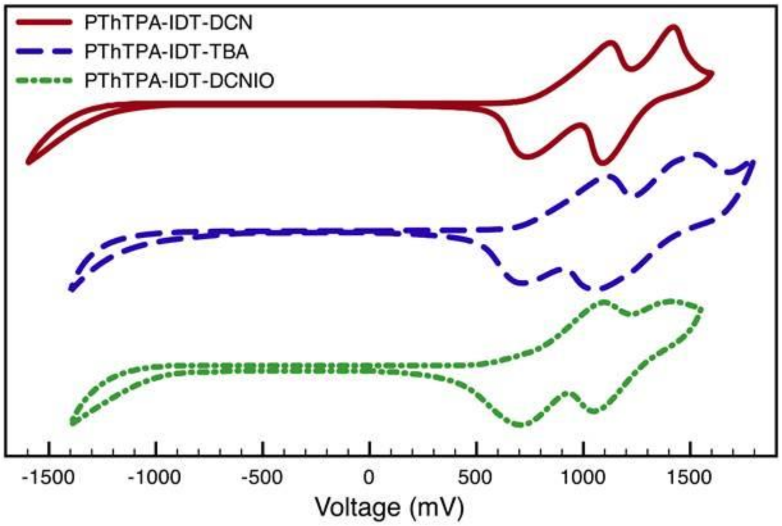

*Figure 2.5: CV scans for the three PThTPA-IDT polymers*

summarized in Table 2.1. All three polymers exhibit two quasi-reversible oxidation processes. The first is attributed to the oxidation of the triphenylamine unit and the second may be due to the oxidation of the fused IDT moiety, which can delocalize and stabilize the resultant charge. The HOMO was calculated from the equation

$$E_{HOMO}\,(eV) = -e(E_{ox} - E_{1/2}(ferrocene) + 4.8\,V)$$

where $E_{ox}$ is the onset oxidation potential of the polymers vs Ag/Ag$^+$. Conversely, the reductive curves were entirely irreversible and changed drastically upon repeated cycles. Therefore, the LUMO was calculated from the optical band edge and HOMO energy level from the equation

$$E_{LUMO} = E_{HOMO} + E_g^{opt}$$

where $E_g^{opt}$ denotes the optical band gaps of the polymers. PThTPA-IDT-DCN, PThTPA-IDT-TBA, and PThTPA-IDT-DCNIO have HOMO levels of -5.18, -5.14, and -5.13 eV and LUMO levels of -3.17, -3.27, and -3.40 eV, respectively. The strength of the acceptor has minimal effect on polymer HOMO, but a significant effect on the LUMO and $E_g$, in agreement with the DFT predictions. Stronger acceptors stabilize the LUMO to a greater extent, which thereby lowers the $E_g$.

### 2.3.2 Field Effect Transistor and Photovoltaic Performance

Finally, the PThTPA-IDT behavior and device performance were evaluated. The device parameters are summarized in Table 2.2. Top-contact OFET devices were fabricated to test the lateral hole mobility of the PThTPA-IDT polymers. Polymer thin films were spin-coated on $Si/SiO_2$ substrates coated with an octyltrichlorosilane (OTS) self-assembled monolayer (SAM), and gold was used for the source and drain electrodes. The OFET devices displayed typical p-channel characteristics. The hole mobilities of PThTPA-IDT-DCN, PThTPA-IDT-TBA, and PThTPA-IDT-DCNIO were $2.63 \times 10^{-4}$, $1.28 \times 10^{-3}$, and $5.30 \times 10^{-4}$ $cm^2\ V^{-1}\ s^{-1}$, respectively. The OFET transfer and output curves are shown in Figure 2.6.

The space charge limited current (SCLC) model was also employed to investigate the vertical hole mobilities. The mobilities were extracted by modeling the dark current in the SCLC region. The calculated vertical hole mobility of PThTPA-IDT-DCN, PThTPA-IDT-TBA, and PThTPA-IDT-DCNIO BHJ films were $6.76 \times 10^{-5}$, $1.15 \times 10^{-4}$, and $1.66 \times 10^{-4}$ $cm^2\ V^{-1}\ s^{-1}$, respectively. The vertical mobilities are roughly one order of

*Table 2.2: OFET and OPV performance parameters for PThTPA-IDT polymers*

| Polymer | $\mu_{FET}$ ($cm^2\ V^{-1}\ s^{-1}$) | $\mu_{SCLC}$ ($cm^2\ V^{-1}\ s^{-1}$) | $V_{oc}$ (V) | $J_{SC}$ ($mA\ cm^{-2}$) | FF | PCE (%) |
|---|---|---|---|---|---|---|
| PThTPA-IDT-DCN | $2.63 \times 10^{-4}$ | $6.76 \times 10^{-5}$ | 0.83 | 3.42 | 0.43 | 1.23 |
| PThTPA-IDT-TBA | $1.28 \times 10^{-3}$ | $1.15 \times 10^{-4}$ | 0.87 | 5.19 | 0.44 | 1.97 |
| PThTPA-IDT-DCNIO | $5.30 \times 10^{-4}$ | $1.66 \times 10^{-4}$ | 0.86 | 5.17 | 0.45 | 1.98 |

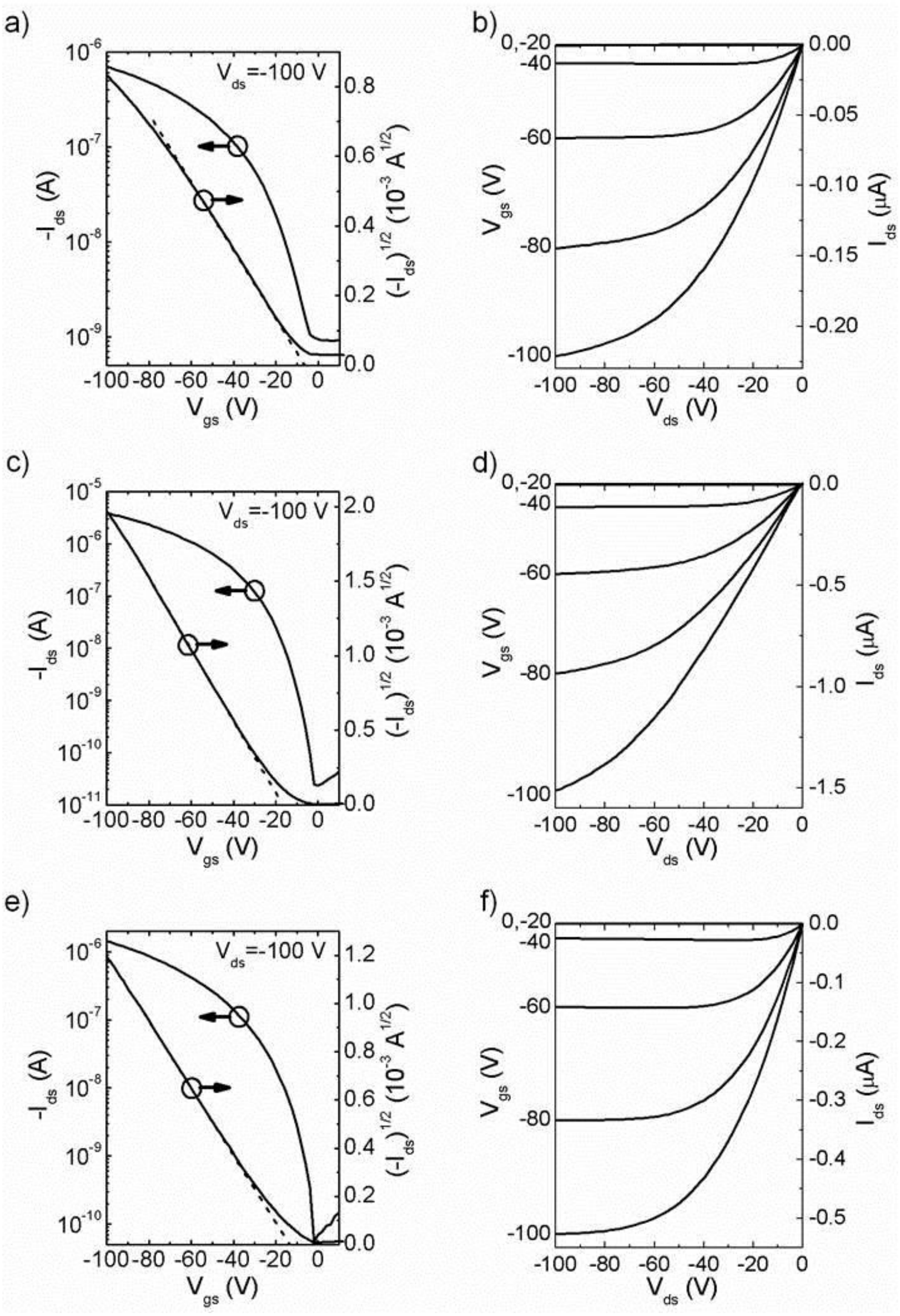

*Figure 2.6: OFET transfer (a, c, e) and output (b, d, f) plots for PThTPA-IDT-DCN (a,b), PThTPA-IDT-TBA (c, d), and PThTPA-IDT-DCNIO (e, f)*

magnitude lower than the horizontal mobilities. This small discrepancy suggests that these polymers exhibit nearly isotropic charge transport characteristics, which can be attributed to the hyperbranched amorphous nature of the polymers. The hole mobilities were largely insensitive to annealing, as expected for amorphous polymers. These mobility values are very similar to the previously reported hole mobilities of other D–$\pi$-bridge–A polymers. [142-146,150-154] Although these mobilities are reasonable for OPV applications, they are lower than those reported for IDT-containing linear D-A polymers, which might lead to increased charge recombination and inefficient charge transfer. It is likely that the mobilities are limited by poor intermolecular charge transport due to weak intermolecular interactions.

The photovoltaic properties of the PThTPA-IDT polymers were tested using $PC_{71}BM$ as the acceptor in the conventional device configuration of ITO/PEDOT:PSS(40 nm)/polymer:$PC_{71}BM$/Ca(30 nm)/Al(100 nm). $PC_{71}BM$, which absorbs more visible light than $PC_{61}BM$,[174] was utilized as the n-type acceptor to efficiently harvest solar output. The BHJ active layer was prepared by spin-coating a chloroform:chlorobenzene (1:1, v/v) solution of polymer:$PC_{71}BM$ on the PEDOT:PSS layer. All the devices were heated at 150 °C for 10 min prior to electrode deposition. Representative J-V curves are depicted in Figure 2.8 and average device parameters are summarized in Table 2. Overall, the best device performances were obtained with a 1:4 blending ratio, which may be due to the optimized electron-hole charge balance and reduced charge recombination.

Photovoltaic devices fabricated from PThTPA-IDT-DCN showed a PCE up to 1.23% with a $V_{oc}$ of 0.83 V, a FF of 0.43 and a $J_{sc}$ of 3.42 mA $cm^{-2}$. Comparatively, PThTPA-IDT-TBA and PThTPA-IDT-DCNIO showed nearly identical FF (0.44 and

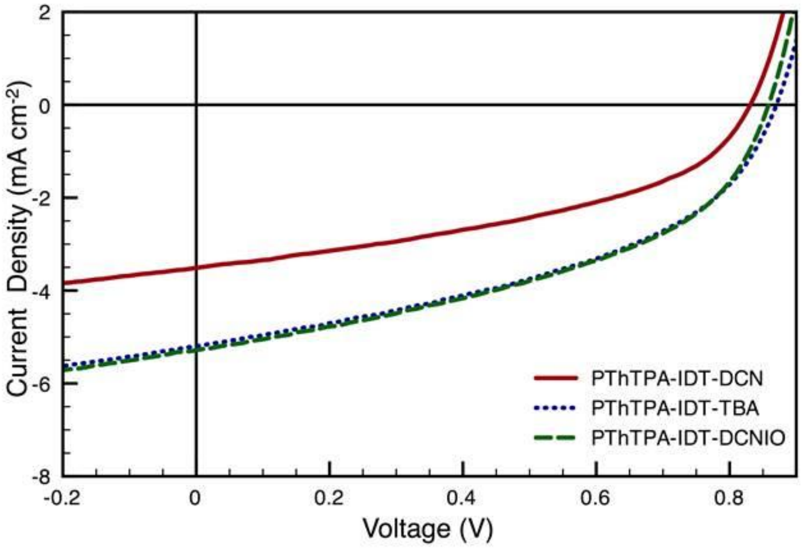

*Figure 2.7: J-V curves for the three PThTPA-IDT polymers*

0.45), $V_{oc}$ (0.87 and 0.86 V), $J_{sc}$ (5.19 and 5.17 mA $cm^{-2}$), and PCE (1.97% and 1.98%). Representative current-voltage curves for the three polymers measured under standard illumination conditions (100 mA $cm^{-2}$, AM 1.5G) are plotted in Figure 2.7. Since the $V_{oc}$ is largely governed by the difference between the polymer HOMO level and the PCBM LUMO and the polymers have nearly identical HOMO levels as measured by CV, the $V_{oc}$ values are expected to be very similar for all the PThTPA-IDT polymers. These $V_{oc}$ values are reasonably high for OPV devices. The FF values of the three polymers are nearly identical as well, suggesting similar loss mechanisms for each polymer. However, despite the improved absorbance profile compared to existing D–$\pi$-bridge–A polymers, each of the PThTPA-IDT devices has comparatively low $J_{sc}$ values, which results in low PCE values. We speculate that the low $J_{sc}$ and FF values are due to the limited external quantum efficiency (EQE) of the polymers (Figure 2.8). All three polymers have EQE values below 30%, which is lower than many high-efficiency D-A polymers. These

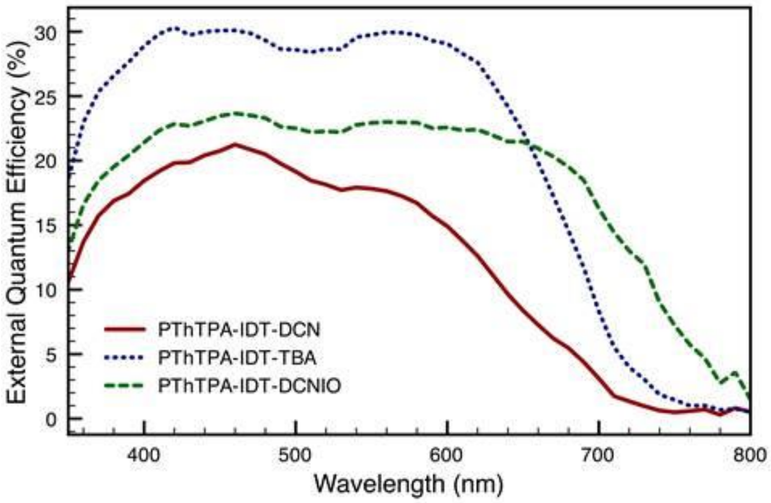

*Figure 2.8: EQE plot for the three PThTPA-IDT polymers*

limited EQE values could be due to several factors. First, the polymers exhibit relatively small absorption coefficients. Based on the limited hole mobilities, geminate recombination is likely a major loss pathway. This is supported by the relatively thin optimized BHJ thicknesses (70-80 nm). Also, the IDT $\pi$-bridge acts as an insulating unit, which may hinder charge transport down the side chain and thereby lead to exciton recombination in the polymer backbone. Finally, higher recombination rates could be due to the undesirable morphology of the polymers (Figure 2.9). Both PThTPA-IDT-DCN and PThTPA-IDT-DCNIO exhibit severe phase segregation with $PC_{71}BM$, which could contribute to exciton recombination before the excitons are able to diffuse to polymer/fullerene interfaces. Conversely, PThTPA-IDT-TBA shows no significant polymer or fullerene domains, which may contribute to increased geminate recombination. The reasons for these striking morphological differences between the three polymers are not known and are currently under investigation.

Interestingly, the device parameters of PThTPA-IDT-TBA and PThTPA-IDT-DCNIO are nearly identical despite the significant differences in their electronic

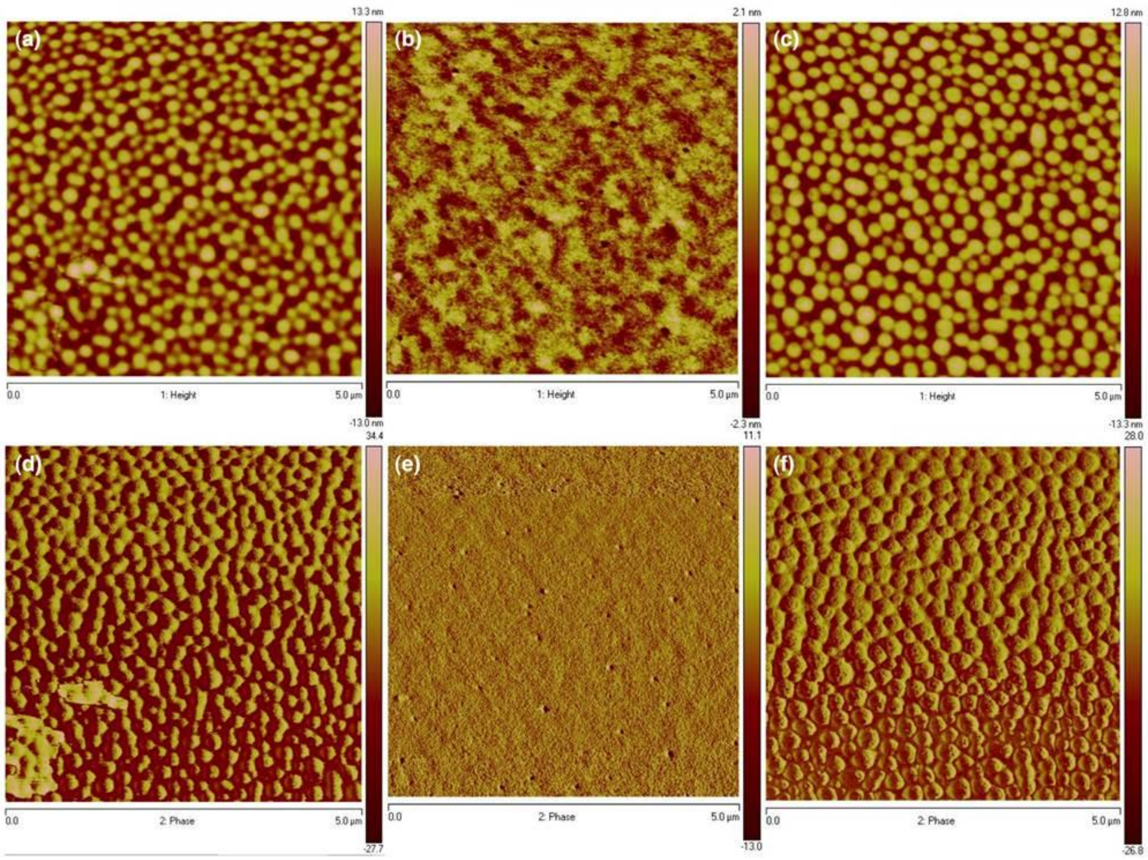

*Figure 2.9: AFM height (a, b, c) and phase (d, e, f) images for PThTPA-IDT-DCN (a,d), PThTPA-IDT-TBA (b, e) and PThTPA-IDT-DCNIO (c, f)*

properties. The EQE for PThTPA-IDT-TBA from 400-625 nm approaches 30%. However, although PThTPA-IDT-DCNIO can harvest photons at longer wavelengths due to its smaller band gap, its EQE from 400-625 nm never surpasses 25%. This is attributed to the undesirable morphology of the $PC_{71}BM$:PThTPA-IDT-DCNIO BHJ, which increases the recombination rate at all wavelengths. However, this increased recombination rate is balanced by an increased photoresponse at longer wavelengths, which generates a similar $J_{sc}$ for PThTPA-IDT-TBA and PThTPA-IDT-DCNIO, despite their inherent chemical and electronic differences.

## 2.4 Conclusion

A new class of tunable light-harvesting polymer (PThTPA-IDT) with dipolar chromophores embedded in the conjugated backbone was designed and synthesized. This precursor polymer was functionalized with three electron-accepting moieties via a Knoevenagel condensation reaction. The thiophene-triphenylamine backbone contributed to enhanced conjugation length and improved ICT characteristics, as seen in the absorbance spectra. The photovoltaic properties of these polymers were investigated and the highest achieved PCEs for PThTPA-IDT-DCN, PThTPA-IDT-TBA, and PThTPA-IDT-DCNIO were 1.23%, 1.97%, and 1.98%, respectively. The PCE was limited by the low $J_{sc}$ and FF of this polymer system, which are attributed to poor morphology and relatively low hole mobilities. The undesirable morphology and low mobilities could contribute to decreased charge separation efficiency and increased recombination rates in the active layer.

## 2.5 Experimental

**Materials:** Unless otherwise specified, all chemicals were purchased from Aldrich or TCI and used without further purification. 3-Bromo-4-iodothiophene,[175,176] N,N-Diphenyl-4-(trimethylstannyl)aniline,[177,178] indacenodithiophene,[162] and 2,5-bis(trimethylstannyl)thiophene[179] were prepared as previously reported. Solvents for synthesis were purified by distillation. All chemical reactions were carried out in a nitrogen atmosphere.

**Quantum mechanical calculations:** All DFT calculations were performed using Gaussian 09(A.02)[168] employing the hybride B3LYP[169,170] exchange-correlation functional with a split valence 6-31G*[171] basis set. Alkyl substituents were replaced by methyl groups for computational simplicity as their replacement with shorter chains does not significantly affect optimized geometry or predicted energy levels of the polymers.

**General measurement and characterization:** UV-visible spectra were tested using a Perkin-Elmer Lambda-9 spectrophotometer. $^1$HNMR and $^{13}$CNMR spectra were collected on a Bruker AV 300 or 500 spectrometers operating at 300 or 125 MHz in deuterated chloroform solution with TMS as reference. HRMS spectra were recorded on an Applied Biosystems QTOF QStar XL Mass Spectrometer. Polymer molecular weights were measured by a Waters 1515 gel permeation chromatograph (GPC) with a refractive index detector at room temperature (THF as the eluent). Cyclic voltammetries of polymer films were conducted on a BAS CV-50W voltammetric system with a three-electrode cell in acetonitrile with 0.1 M of tetrabutylammonium hexafluorophosphate using a scan rate of 100 $mV \cdot s^{-1}$. ITO, Ag/AgCl and Pt mesh were used as working electrode, reference electrode and counter electrode, respectively. The differential scanning calorimetry (DSC) was performed using DSC2010 (TA instruments) under a heating rate of 10 $^oC \cdot min^{-1}$ and a nitrogen flow of 50 $mL \cdot min^{-1}$. The AFM images under tapping mode were taken from the actual devices fabricated for photovoltaic measurement on a Veeco multimode AFM with a Nanoscope III controller.

**Fabrication and characterization of OFET and OPV devices:** The field-effect transistors were fabricated with a bottom-gate, top-contact configuration. The heavily n-doped silicon substrates with a 300 nm thick thermally grown $SiO_2$ dielectric (from Montco Silicon Technologies, Inc.) were first cleaned by sonication in acetone and isopropanol and exposed to air plasma. The cleaned substrates were then treated with hexamethyldisilazane (HMDS) through vapor phase deposition in a vacuum oven (200 mTorr, 100 °C, 3 h). Subsequently, the semiconductor polymer films were spin-coated in a glove box from their 10 mg/mL chloroform solutions which were stired overnight and filtered with 0.2 μm PTFE filter. Interdigitated source and drain electrodes (L=1000 μm, W=12 μm) were deposited by evaporating a 50 nm thick gold film and defined with a shadow mask. The transfer and output characteristics were measured in glove box using an Agilent 4155B semiconductor parameteranalyzer. The saturation field-effect mobility (μ) was calculated from the following equation:

$$I_{ds} = \mu(W/2L)\, C_i(V_{gs} - V_{th})^2$$

where W and L are the channel width and length, respectively. $C_i$ is the capacitance of insulating $SiO_2$ layer per unit, $V_{gs}$ and $V_{th}$ are the gate voltage and the threshold voltage, respectively. The threshold voltage ($V_{th}$) was obtained as the x intercept of the linear section of the plot of $(I_{ds})_{1/2}$ vs $V_{gs}$. The subthreshold swing was estimated by taking the inverse of the slope of $I_{ds}$ vs $V_{gs}$ in the region of exponential current increase.

**Fabrication of photovoltaic and hole-only devices:** To fabricate conventional configuration solar cells, ITO-coated glass substrates (15 Ω/sq.) were first cleaned with detergent, de-ionized water, acetone, and isopropyl alcohol. Subsequently, PEDOT:PSS (Baytron® PVP AI 4083, filtered at 0.45 μm) layer (~45 nm) was spin-coated on the cleaned ITO-coated glass substrates at 5,000 rpm and then annealed at 120 °C for 30 min under ambient conditions. After that, the substrates were loaded into a nitrogen-filled glove-box. Following that, the active layer was spin-coated onto the PEDOT:PSS layer from a homogeneously blended solution of polymer:$PC_{71}BM$.

The solution was prepared by dissolving the polymer and $PC_{71}BM$ with a certain blending weight ratio in *o*-dichlorobenzene (o-DCB) overnight and filtered with a 0.2 μm PTFE filter. Finally, the substrates were transferred into the evaporator with shadow masks to define the active area of the devices (10.08 $mm^2$) and pumped under high vacuum ($< 2 \times 10^{-7}$ Torr). Then calcium (30 nm) and aluminum (100 nm) were sequentially thermally evaporated onto the active layer. The un-encapsulated solar cells were measured in glove box conditions using a Keithley 2400 SMU source measurement unit and an Oriel Xenon lamp (450 W) with an AM1.5 filter as the solar simulator. A reference silicon solar cell with a KG5 filter, which has been previously standardized by the National Renewable Energy Laboratory(NREL), was used to calibrate the light intensity to 100 $mW/cm^2$. To fabricate the hole-only device, the same procedure used to make the photovoltaic devices was followed except $MoO_3$ replaced the calcium.

**Synthesis of compound 1:** IDT (1.51 g, 1.7 mmol) was dissolved in anhydrous DMF (40 mL) and the solution was cooled to 0°C. $POCl_3$ (0.292 g, 1.9 mmol) was added to this dropwise. The solution was gradually warmed to room temperature, heated to 50°C and allowed to stir for 8 h. Then, saturated $NaC_2H_3O_2$ (60 mL) was added and the solution was stirred for a further 30 min. The mixture was extracted with dichloromethane and the combined organic layers were washed repeatedly with saturated NaCl solution. Then, the organic fraction was dried with $Na_2SO_4$, concentrated *in vacuo*, and the crude product was purified by column chromatography (1:1 dichloromethane:hexane) to yield compound **1**, a yellow solid (0.99 g, 64%). $^1$H NMR (300 MHz, $CDCl_3$, ppm): 9.93 (s, 1H), 7.77 (s, 1H), 7.69 (s, 1H), 7.59 (s, 1H), 7.43 (d, J = 6 Hz, 1H), 7.29 (m, 11H), 7.21

(d, J = 3 Hz, 2H), 7.18 (d, J = 3 Hz, 2H), 7.14 (d, J = 6 Hz, 2H), 2.69 (t, J = 6 Hz, 8H), 1.70 (m, 8H), 1.42 (m, 25H), 0.99 (m, 12H). $^{13}$C NMR (500 MHz, $CDCl_3$, ppm): 183.02, 158.13, 154.81, 142.79, 142.15, 141.79, 135.91, 128.31, 128.25, 127.28, 123.90, 118.03, 62.87, 35.49, 31.78, 31.59, 29.50, 22.88, 14.33.

**Synthesis of compound 2:** Compound **1** (0.95 g, 1.0 mmol) was dissolved in THF (50 mL) and cooled to 0°C. NBS (0.199 g, 1.1 mmol) was added in one portion, the solution was gradually warmed to room temperature and stirred overnight. The solution was poured into $H_2O$ and extracted with ethyl acetate. The combined organic layers were dried with $Na_2SO_4$ and concentrated *in vacuo* to yield compound **2**, a yellow solid (0.957 g, 93%). $^1$H NMR (300 MHz, $CDCl_3$, ppm): 9.93 (s, 1H), 7.77 (s, 1H), 7.69 (s, 1H), 7.59 (s, 1H), 7.29-7.13 (m, 17H), 2.69 (t, J = 6 Hz, 8H), 1.70 (m, 8H), 1.42 (m, 24H), 0.99 (t, J = 3 Hz, 12H).$^{13}$C NMR (500 MHz, $CDCl_3$, ppm): 183.10, 158.08, 154.83, 142.84, 142.19, 141.80, 135.91, 128.29, 128.20, 127.29, 123.87, 117.99, 62.88, 35.49, 31.78, 31.59, 29.50, 22.88, 14.33. HRMS calcd for $C_{65}H_{73}BrOS_2$ $[M+H]^+$: 1014.3154; found, 1014.3153.

**Synthesis of compound 5:** Compound **2** (0.911 g, 0.9 mmol) was added to an oven-dried flask and degassed three times. $Pd_2(dba)_3$ (4 mg) and $P(o\text{-tol})_3$ (5 mg) were added to the flask and subsequently **4** (0.441 g, 0.1 mmol) dissolved in toluene (5 mL) was added, the solution was cooled to -78 °C and degassed three more times. The solution was stirred at 100 °C for 24 h. Then, the solution was concentrated, dissolved in dichloromethane and extracted with brine. The combined organic layers were dried with $Na_2SO_4$ and concentrated *in vacuo*. The crude product was purified by column chromatography (1:1 dichloromethane:hexane) to yield compound **5**, a bright yellow solid (0.826 g, 78%). $^1$H

NMR (300 MHz, $CDCl_3$, ppm): 9.82 (s, 1H), 7.67 (s, 1H), 7.58 (s, 1H), 7.47 (d, J = 6 Hz, 3H), 7.31-7.06 (m, 29H), 2.58 (t, J = 9 Hz,, 8H), 1.62 (m, 8H), 1.33 (m, 25H), 0.90 (m, 12H). $^{13}C$ NMR (500 MHz, $CDCl_3$, ppm): 182.75, 158.01, 155.96, 154.93, 153.59, 151.64, 148.33, 147.40, 147.39, 145.10, 141.94, 141.72, 141.48, 141.08, 138.82, 138.17, 133.13, 129.37, 128.71, 128.65, 128.74, 127.88, 127.70, 126.21, 124.55, 123.58, 123.20, 118.82, 118.24, 117.27, 63.11, 62.88, 35.63, 31.79, 31.33, 29.19, 22.60, 14.13. HRMS calcd for $C_{83}H_{87}NOS_2$ $[M+H]^+$: 1178.7233; found, 1178.7231.

**Synthesis of compound 6:** Compound **5** (0.810 g, 0.7 mmol) was dissolved in THF (50 mL) and cooled to 0 °C. NBS (0.269 g, 1.5 mmol) was added in one portion, the solution was allowed to gradually warm to room temperature and stirred overnight. The solution was poured into $H_2O$ and extracted with ethyl acetate. The combined organic layers were dried with $Na_2SO_4$ and concentrated *in vacuo* to yield compound **6**, a bright yellow solid (0.872 g, 95%). $^1H$ NMR (300 MHz, $CDCl_3$, ppm): 9.82 (s, 1H), 7.67 (s, 1H), 7.58 (s, 1H), 7.47 (m, 2H), 7.38 (d, J = 9 Hz, 3H), 7.22-7.09 (m, 20H), 7.04 (d, J = 9 Hz, 2 H), 6.97 (d, J = 9 Hz, 3 H), 2.60 (m, 8H), 1.61 (m, 8H), 1.33 (m, 25H), 0.90 (m, 12H).$^{13}C$ NMR (500 MHz, $CDCl_3$, ppm): 182.72, 158.11, 155.99, 154.90, 153.56, 151.61, 148.39, 147.32, 147.33, 145.12, 141.94, 141.76, 141.50, 141.07, 138.89, 138.20, 133.11, 129.37, 128.71, 128.69, 128.77, 127.86, 127.74, 126.20, 124.58, 123.60, 123.21, 118.84, 118.23, 117.28, 63.14, 62.88, 35.63, 31.79, 31.33, 29.19, 22.60, 14.13. HRMS calcd for $C_{83}H_{85}Br_2NOS_2$ $[M+H]^+$: 1336.5156; found, 1336.5151.

**Synthesis of PThTPA-IDT-CHO:** Compound **12** (0.351 g, 0.26 mmol) and 2,5-bis(trimethylstannyl)thiophene (0.108 g, 0.26 mmol) were added to an oven-dried flask and degassed three times. $Pd(PPh_3)_4$ (7 mg) was added to the flask and subsequently anhydrous toluene (4 mL) and DMF (0.5 mL) were added. The solution was stirred at 110 °C for 36 h. Bromobenzene (0.2 mL, 2 mmol) was added and the solution was stirred at 110 °C for 12 h. Trimethyl(phenyl)tin (0.35 mL, 2 mmol) was added and the solution was stirred at 110 °C for another 12 h. The solution was then cooled to rt, poured into MeOH (100 mL), the precipitate filtered through a Soxhlet thimble and purified by Soxhlet extraction for 12 h with acetone, 12 h with methanol, 12 h with hexanes and collected with $CHCl_3$. The $CHCl_3$ solution was concentrated and precipitated into MeOH. Filtration yielded PThTPA-IDT-CHO, a red solid (71 mg). $^1H$ NMR (300 MHz, $CDCl_3$, ppm): 9.79 (s, 1H), 7.63 (s, 1H), 7.52-7.37 (br, 10 H), 7.22-7.06 (br, 23H), 2.56 (m, 8H), 1.59 (m, 8H), 1.28 (m, 24H), 0.86 (m, 12H). $M_w = 43.1 \times 10^3$ g/mol; Đ = 1.94.

**Synthesis of PThTPA-IDT-DCN:** PThTPA-IDT-CHO (50 mg) was dissolved in THF (20 mL) and ethanol was added until the initial appearance of precipitate. Then, malononitrile (90 mg) was added. After 10 min, pyridine (0.05 mL) was added. The solution was warmed to 50°C and stirred at that temperature for 16 h. The solution was concentrated *in vacuo*, dissolved in a small volume of dichloromethane, precipitated in methanol and filtered to yield PThTPA-IDT-DCN as a deep red solid (47 mg). $^1H$ NMR (300 MHz, $CDCl_3$, ppm): 7.63-7.41 (br, 11H), 7.22-7.06 (br, 24H), 2.55 (m, 8H), 1.28 (m, 25H), 0.86 (m, 12H). $M_w = 42.8x10^3$ g/mol; Đ = 1.90.

**Synthesis of PThTPA-IDT-TBA:** PThTPA-IDT-CHO (50 mg) was dissolved in THF (20 mL) and ethanol was added until the initial appearance of precipitate. Then, 1,3-diethyl-2-thiobarbituric acid (140 mg) was added. After 10 min, pyridine (0.05 mL) was added. The solution was warmed to 50 °C and stirred at that temperature for 16 h. The solution was concentrated *in vacuo*, dissolved in a small volume of dichloromethane, precipitated in methanol and filtered to yield PThTPA-IDT-TBA as a dark solid (55 mg). $^1$H NMR (300 MHz, $CDCl_3$, ppm): 8.64 (s, 1H), 7.73-7.65 (m, 3H), 7.58-7.44 (br, 10H), 7.22-7.06 (br, 21H), 4.58 (m, 4H), 2.56 (m, 8H), 1.28 (m, 30H), 0.86 (m, 12H). $M_w$ = 42.1x$10^3$ g/mol; Đ = 1.87.

**Synthesis of ThTPA-IDT-DCNIO:** PThTPA-IDT-CHO (50 mg) was dissolved in THF (20 mL) and ethanol was added until the initial appearance of precipitate. Then, 3-dicyanomethylene-1-indanone (135 mg) was added. After 10 min, pyridine (0.05 mL) was added. The solution was warmed to 50 °C and stirred at that temperature for 16 h. The solution was concentrated *in vacuo*, dissolved in a small volume of dichloromethane, precipitated in methanol and filtered to yield PThTPA-IDT-DCNIO as a dark solid (53 mg). $^1$H NMR (300 MHz, $CDCl_3$, ppm): 8.87 (d, 1H), 8.65 (d, 1H), 7.88 (m, 2H), 7.72-7.61 (m, 4H), 7.54-7.43 (m, 9H), 7.23-7.07 (m, 22H), 2.56 (m, 8H), 1.28 (m, 25H), 0.86 (m, 12H). $M_w = 42.2 \times 10^3$ g/mol; Đ = 1.91.

# 3. Fully Conjugated Comb Copolymers Comprising a P-type Donor-Acceptor Backbone and Poly(3-hexyl)thiophene Side chains Synthesized Via a "Graft Through" Approach

## 3.1 Introduction

Although the efficiencies of OPVs are increasing, one drawback of conjugated polymers is that they tend to have narrow absorption bandwidths, leading to losses from some combination of excitonic thermalization or sub-bandgap transmission.[180-181] The former occurs when an electron is excited beyond the LUMO of the donor and relaxes toward the LUMO during exciton diffusion by releasing energy in the form of photons or phonons. The latter results when photons with energies smaller than the bandgap of the donor are transmitted through the device; this is a direct consequence of the requirements for energy level alignment between the donor, acceptor and electrodes to achieve efficient charge transfer between materials, which places a finite limit on the size of the donor band gap.

One strategy to address these problems simultaneously is to utilize a tandem solar cell, which is composed of two (or more) photovoltaic cells, typically connected in series (Figure 3.1).[182-191] These two cells possess donor/acceptor materials that exhibit complimentary absorption spectra to cover the majority of the visible spectrum; generally, poly-3-hexylthiophene (P3HT) is used in conjunction with smaller band gap donors. Any higher energy photons are absorbed by P3HT, thereby limiting thermalization losses; conversely, any lower energy photons are absorbed by the low band gap material, which alleviates sub-band gap transmission. However, introducing an interconnecting layer between the two cells introduces its own loss mechanisms and

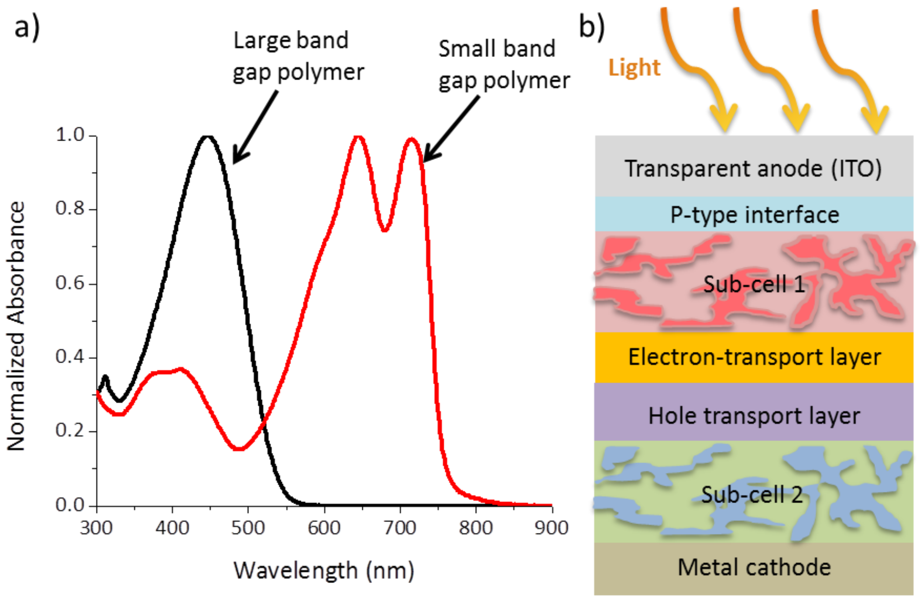

*Figure 3.1: a) Ideal absorption spectra for two light-harvesting compounds in a tandem solar cell and b) typical architecture of a tandem OPV cell*

resistances. In addition, since the cells are connected in series, the $J_{SC}$ is limited by the lower $J_{SC}$ of the two cells. As a result, tandem OPVs are achieving similar champion efficiencies (10.6%)[192] to single-junction OPVs (~10%).[193]

Another strategy to address transmission and thermalization losses without the complicated fabrication inherent to tandem OPVs is to use a ternary blend of materials in a single-junction BHJ (Figure 3.2).[194-199] This method involves adding both a small band gap donor and a wide band gap donor to an n-type acceptor, which is intended to extend the absorption window of the BHJ and thereby improve photon harvesting and the overall $J_{SC}$ of the device. In addition, having a cascade of energy levels between the three BHJ materials has been shown to enhance exciton dissocation efficiencies, which is another major hindrance to achieving high PCE values in OPVs.[200] Such devices have exhibited impressive performances compared to control cells composed of the basis donor materials.[201]

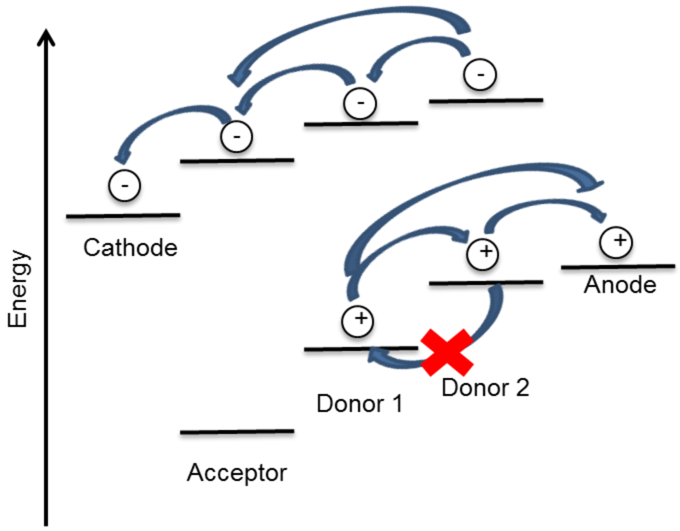

*Figure 3.2: Energy level diagram of a ternary blend OPV cell*

Both small and large band gap donors are essential to tandem and ternary-blend OPVs. Many groups have studied low band gap polymers and small molecules to absorb red/near-infrared photons. Some small molecules, including phthalocyanines and squarines, have shown promise in OPV applications.[191-192] However, the most common conjugated low band gap materials are donor-acceptor (D-A) polymers, which have achieved very high PCE values in OPV cells. Conversely, large band gap materials with promising OPV behavior are less usual; arguably the most heavily studied large band gap conjugated polymer is P3HT.

Since the discovery of P3HT, its synthesis and structure-property relationships have received in-depth attention. However, the early methods of P3HT synthesis were

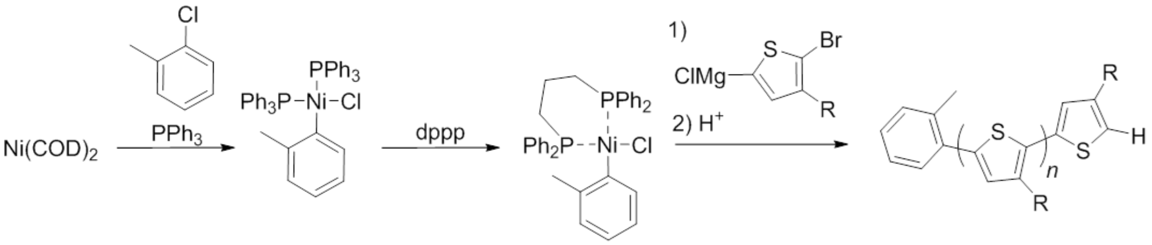

*Figure 3.3: Externally-initiated P3AT synthesis*

limited by the fact that they did not allow P3HT to be initiated from an external functionality. To address this problem, some groups have formed "*ex-situ*" nickel catalysts prior to P3HT growth. The Luscombe group has demonstrated the most reliable and applicable form of this technique by treating bis(cyclooectadiene)nickel(0) (Ni(COD)$_2$) with chlorotoluene followed by bis(diphenylphosphino)propane (dppp) to form a *ex situ* aryl-halide nickel(II) oxidation addition product, which was used to initiate P3HT growth (Figure 3.3). With this method, P3HT chains grew controllably and with low Đ from the toluene initiator, eliminating irregularities at the polymer origin and enabling high levels of regioregularity.[202]

These advances in externally-initiated P3HT synthesis, along with the optical limitations of existing organic polymers, inspired the research contained herein. With the development of a widely applicable method to initiate P3HT from substrates and small molecules, one of the next extensions of P3HT synthesis is to form a fully-conjugated brush copolymer integrating a donor-acceptor polymer with P3HT.

However, conjugated polymers also suffer from inherently low dielectric constants compared to inorganic materials, which lead to high recombination rates. There have been attempts to covalently bond p- and n-type materials through conjugated and aliphatic chains to achieve better exciton separation efficiencies.[203-204] There are few studies focusing on covalently-bound fully conjugated materials able to absorb wide swathes of the visible to near-infrared (IR) spectrum. Covalently grafting a wide band gap light harvester onto a small band gap donor-acceptor polymer might be beneficial to the exciton dissocation efficiency in the BHJ. Like ternary blends, creating a covalent, conjugated linkage between two electronically-active materials with sufficiently offset

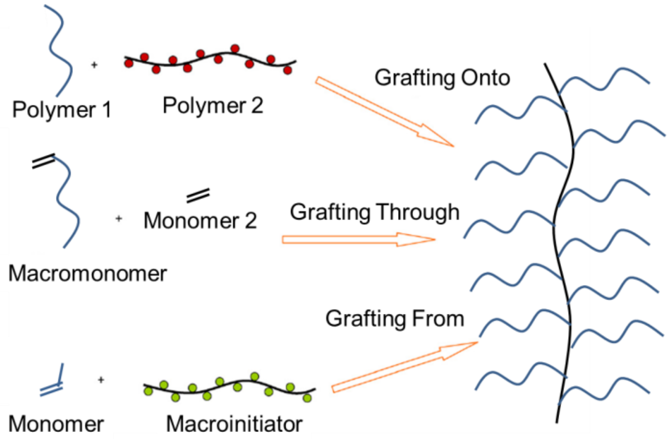

*Figure 3.4: Illustration of grafting methods*

energy levels could enhance exciton dissociation via stepwise charge separation, but without having to rely on random exciton diffusion processes to promote exciton dissociation. Moreover, if these two materials had complimentary absorption profiles, thermalization and sub-band gap transmission issues could simultaneously be mitigated. To the best of the author's knowledge, there have been no reports of direct conjugation between two covalently-linked p-type polymers with complimentary absorption.

In order to covalently bond two conjugated polymers, one can utilize several grafting methods: "grafting onto", "grafting from" or "grafting through" (Figure 3.4). Grafting onto involves synthesizing the polymers separately, then linking them via a chemical reaction. This method is prone to low grafting efficiency due to steric congestion and is not often used.[205] Grafting from involves the initiation and growth of a polymer from an initiator polymer. If the order of and conditions for the polymerizations are carefully selected, grafting from can yield complex well-defined products. However, depending on the reactivity of the initiator polymer, results from this method vary. Finally, grafting through involves the polymerization of a "macromonomer" (a reactive monomer functionalized with a pendant polymer). The polymacromonomers resulting

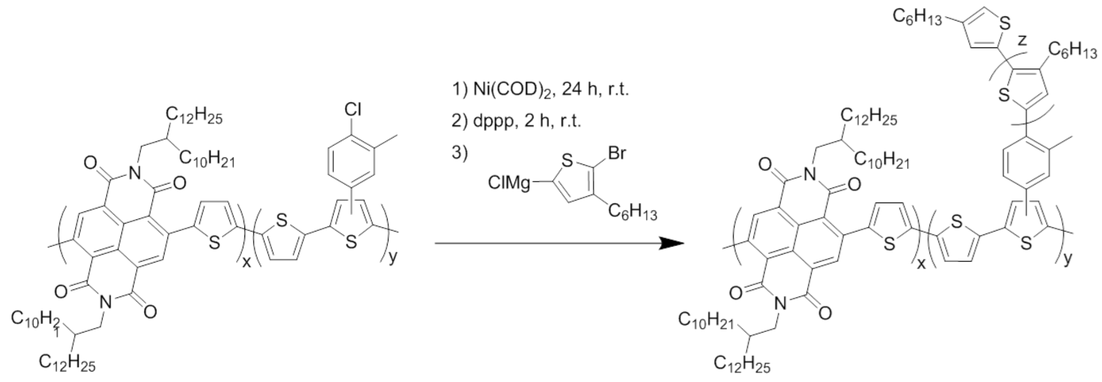

*Figure 3.5: First example of a fully-conjugated graft copolymer*[207]

from this method have necessarily high grafting densities, but often have a low degree of polymerization (DP, or the number of repeat units) due to the steric hindrance of the pendant polymer and low concentration of polymerizable groups on the macromonomer.[206]

Until recently, there had been no examples of KCTP as a tool to synthesize a fully-conjugated comb copolymer. The first report of a fully-conjugated brush copolymer was published during the following studies by Wang, J. et al.[207] In this publication, the authors synthesized an n-type napthalenediimide-thiophene copolymer functionalized with a chlorotoluene moiety from which P3HT was grafted (Figure 3.5). Using chemistry pioneered by the Luscombe group, the copolymer was treated with a nickel(0) complex to form a series of nickel(II) catalysts on the polymer backbone, which were used to initiate P3HT growth. The resultant graft copolymers exhibit optical properties of both P3HT and the NDI-thiophene copolymer, but possess only p-type characteristics with a lower hole mobility (~$10^{-2}$ $cm^2/Vs$) than P3HT (up to $10^{-1}$ $cm^2/Vs$).[208]

Similarly, the studies contained herein involve the synthesis of a donor-acceptor polymer with pendant P3HT chains, but the aim and hypothesis differ. The project was

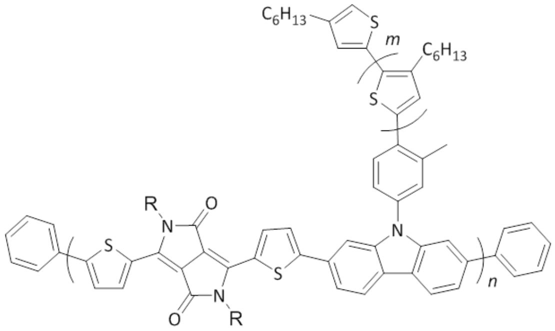

*Figure 3.6: First reported fully-conjugated graft copolymer between two p-type polymers*

predicated on the idea that it is possible to functionalize a low-band gap p-type donor-acceptor polymer with P3HT chains to yield a fully-conjugated brush copolymer that has broadband absorbance across the visible spectrum. Of particular interest was the largely unexplored synthetic chemistry involved with generating such a polymer, as well as the eventual effects on the optoelectronic characteristics of the final polymer and whether it would adopt the characteristics of the donor-acceptor polymer, P3HT, or would conflate properties of the individual polymers.

Herein, a fully-conjugated comb copolymer comprised of a carbazole (Cbz)/diketopyrrolopyrrole (DPP) backbone and P3HT side chains is reported (Figure 3.6). The polymer was synthesized via a "graft through" approach, wherein a series of boronic ester-functionalized Cbz-P3HT macromonomers with different degrees of P3HT polymerization were synthesized and subsequently polymerized with a DPP comonomer by a Suzuki coupling reaction. The physical, optical, and electrochemical properties of the macromonomers and resultant comb copolymers are reported, as well as organic field effect transistor (OFET) performances.[209]

The parent D-A copolymer from which to graft P3HT was chosen based on two requisites: 1) complementary absorption to P3HT and 2) minimal electronic communication between the backbone of the D-A copolymer and the P3HT chain. The former was important to realize broadband absorption, while the latter was necessary to avoid conflation of the properties of the D-A copolymer and P3HT, or dominance of one set of traits over the other. Ultimately, a Cbz-DPP copolymer was chosen because it has an absorption max ($\lambda_{max}$) ca. 650 nm in solution[210] and a chlorotoluene initiator can easily be affixed to the Cbz group. In addition, it has been shown that there is little electron delocalization from the Cbz system to the pendant phenyl ring in *N*-phenylcarbazoles due to the torsional twist (ca. 60°) between the fused Cbz system and the pendant phenyl ring, as well as the partial break in conjugation through the central nitrogen.[211] It was hoped that this would preserve the individual characteristics of the D-A copolymer and P3HT in the final graft polymer, and avoid the conflation or dominance of the properties of the respective polymers. This break in conjugation is also important due to the limitations of the formation of the nickel catalyst complex used for external initiation. Previous studies have determined that including either electron-donating or electron-withdrawing functionalities *para* to the nickel site decreases the rate of oxidative addition and increases the likelihood of disproportionation reactions.[212] Finally, Cbz-DPP exhibits reasonable organic field effect transistor (OFET) hole mobilities ($\sim10^{-2}$ $cm^2/Vs$) and mediocre OPV performance (~1.6%), limited by a low $J_{sc}$ (5.2 $mA/cm^2$) and FF (~40%).[205] It was hypothesized that grafting P3HT on a Cbz-DPP copolymer (Figure 10b) would boost the $J_{sc}$ associated with the Cbz-DPP copolymer. It was also hoped that this design would have interesting effects on exciton dissociation in OPVs and further improve the device performance.

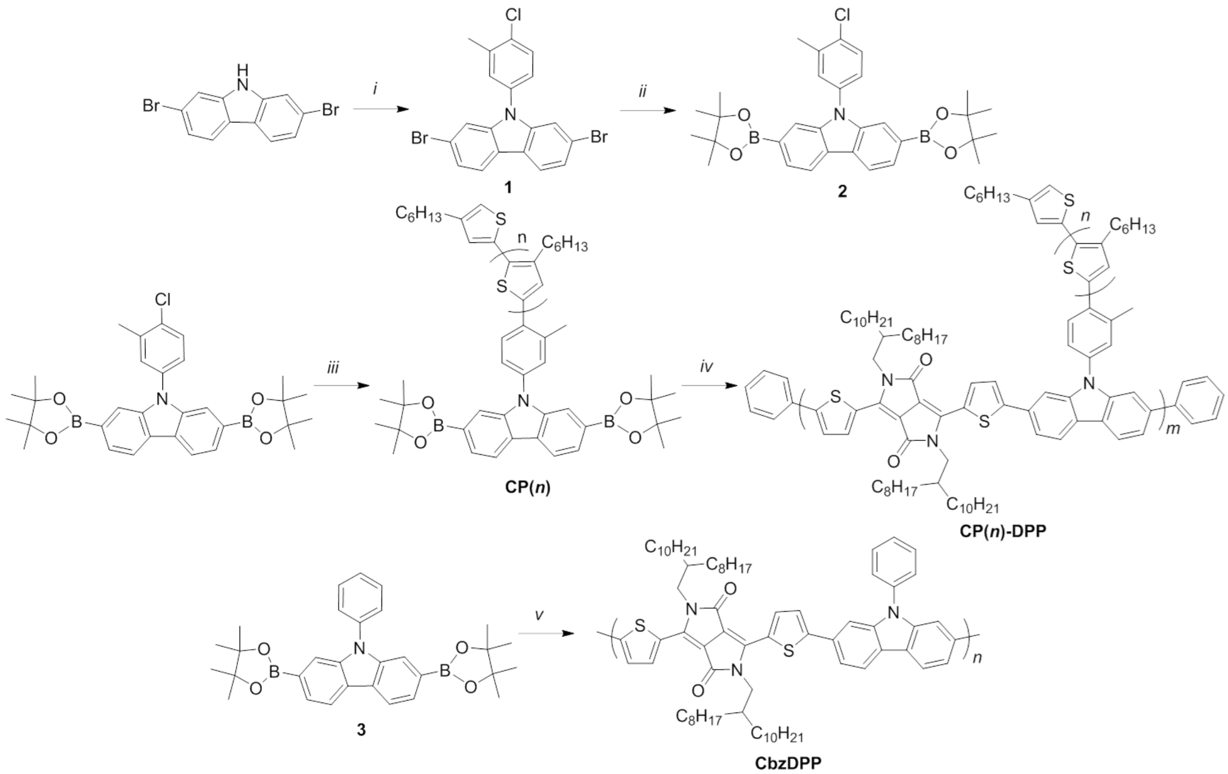

*Scheme 2: Synthesis of graft copolymer. i) CuI, 1-chloro-4-iodo-2-methylbenzene, 1,10-phenanthroline, $K_2CO_3$, DMF, 125 °C, 16 h, 38%; ii) a) n-BuLi, THF, -78 °C, 1 h, b) 2-isopropoxy-4,4,5,5-tetramethyl-1,3,2-dioxaborolane, r.t., overnight, 76%; iii) a) $Ni(COD)_2$, $PPh_3$, toluene, 50 °C, 3 d, b) 1,3-bis(diphenylphosphino)propane, r.t., 3 h, c) 2-bromo-5-magnesium chloride-3-hexylthiophene; iv) a) 3,6-bis(5-bromothiophen-2-yl)-2,5-bis(2-octyldodecyl)pyrrolo[3,4-c]pyrrole-1,4(2H,5H)-dione, 18-crown-6, Aliquat 336, $Pd(PPh_3)_4$, toluene, 2M $K_2CO_3$, 110 °C, 3 d, b) phenylboronic acid, 110 °C, 12 h, c) bromobenzene, 110 °C, 12 h. v) a) 3,6-bis(5-bromothiophen-2-yl)-2,5-bis(2-octyldodecyl)pyrrolo[3,4-c]pyrrole-1,4(2H,5H)-dione, 18-crown-6, Aliquat 336, $Pd(PPh_3)_4$, toluene, 2M K2CO3, 110 °C, 3 d, b) phenylboronic acid, 110 °C, 12 h, c) bromobenzene, 110 °C, 12 h.*

## 3.2 Synthesis

Synthesis of the 9-(4-chloro-3-methylphenyl)-2,7-bis(4,4,5,5-tetramethyl-1,3,2-dioxaborolan-2-yl)-9*H*-carbazole monomer (**2**, Scheme 2) began with the standard 2,7-dibromocarbazole synthesis.[213] From here, an Ullman-type copper-catalyzed amination[214] furnished **1** in modest yield, which was converted to **2** by lithiation and quenching with 2-isopropoxy-4,4',5,5'-tetramethyldioxaborolane. Concurrently, the P3HT and DPP monomers were synthesized according to established protocols.[215-216]

The first attempt at comb polymer synthesis involved a "graft from" approach. First, the Cbz-DPP copolymer was synthesized from **2** and the DPP monomer. Traditional external initiation catalyst formation conditions (room temperature, 24 h) were used to form the *ex situ* nickel(II) catalyst. Unfortunately, $^{31}$P-NMR revealed that the oxidative addition reaction of the Ni(COD)$_2$ to the aryl-Cl bond did not occur. Even allowing the oxidative addition reaction to occur at higher temperatures (50 °C) and extended times (72 h) showed no evidence of nickel insertion.

At this juncture, it was of interest to determine if the oxidative addition could be accomplished using the boronic ester-functionalized Cbz monomer. Again, traditional *ex situ* catalyst formation conditions showed no evidence of the oxidative addition product. It was ascertained that heating to 50 °C for three days was necessary to promote the oxidative addition; the $^{31}$P-NMR spectrum (Figure 3.7a) shows a singlet occurring at 20 ppm, which is indicative of the oxidative addition product. The subsequent ligand exchange with 1.5 equivalents of 1,3- dppp went rapidly after stirring for two hours at room temperature. The $^{31}$P NMR spectrum (Figure 3.7b) shows the disappearance of the NiCbz(PPh$_3$)$_2$Cl peak, and the emergence of doublets at 20.09 and -6.09 ppm (*J* = 114

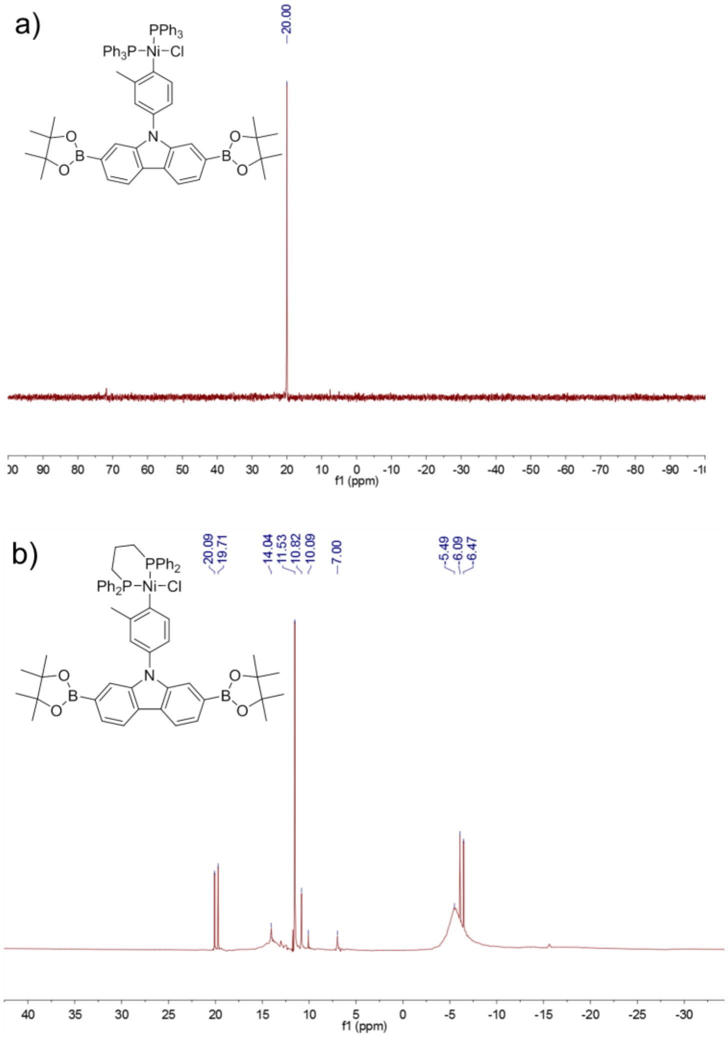

*Figure 3.7: a) ${}^{31}$P-NMR of nickel catalyst oxidative addition product and b) after ligand exchange with dppp*

Hz), corresponding to the two phosphine ligands, and a narrow singlet at 11.53 ppm and broad singlet at -5.49 ppm, respectively corresponding to Ni(dppp)$_2$ and displaced PPh$_3$. The Ni(dppp)$_2$ likely forms from Ni(PPh$_3$)$_4$, which remains in solution as a result of the slow oxidative addition reaction. This solution was then injected into Grignardized 2-bromo-3-hexyl-5-iodothiophene (25 eq to Ni(COD)$_2$) at 0 °C, warmed to room temperature, stirred for 5 h and finally quenched with 5 M hydrochloric acid. After precipitation and Soxhlet extraction, ${}^1$H NMR revealed that P3HT was grown from the

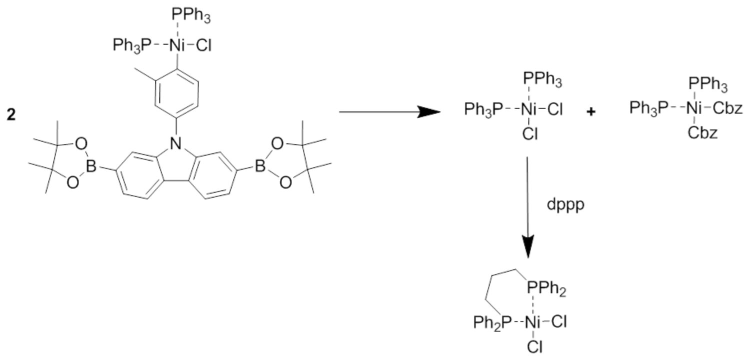

*Figure 3.8: Proposed disproportionation during oxidative addition reaction*

carbazole initiator (as shown by the shift in carbazole aromatic peaks and appearance of characteristic P3HT aromatic/aliphatic peaks) and the boronic esters were left intact to form the CP macromonomer. It is important to note that the generation of catalytically inactive Ni(dppp)$_2$ skewed the calculated nickel:monomer ratio, consistently yielding P3HT with twofold higher DP than expected.

Unfortunately, thin layer silica ($SiO_2$) chromatography revealed the presence of non-externally initiated P3HT as a result of these reactions. The most likely reason for this byproduct is disproportionation reactions during catalyst formation. Disproportionation reactions involve the exchange of ligands between two catalyst complexes and have been identified as a major source of side reactions during P3HT synthesis. *Para*-substituted Aryl-Ni($PPh_3$)$_2$-X complexes are known to be especially unstable to disproportionation.[217] If disproportionation is the source of the non-externally-initiated P3HT, it is likely occurring during the oxidative addition reaction when two NiCbz($PPh_3$)$_2$Cl complexes disproportionate to form NiCbz$_2$($PPh_3$)$_2$ and Ni($PPh_3$)$_2$Cl$_2$, which go on to form NiCbz$_2$(dppp) and Ni(dppp)Cl$_2$ (Figure 3.8). The latter complex is the catalyst historically used for P3HT synthesis, which would explain the presence of P3HT in the polymer mixture.[218]

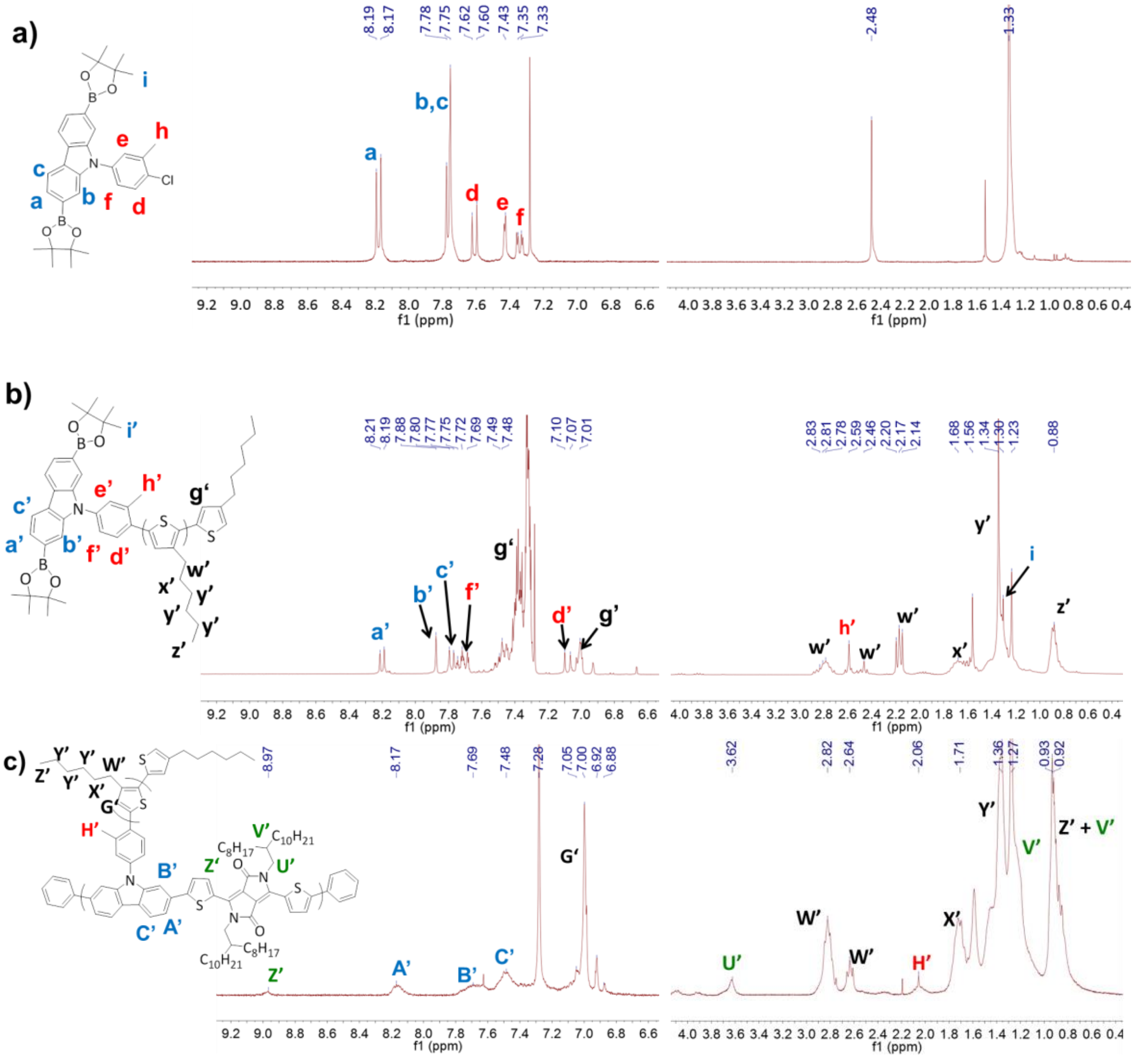

*Figure 3.9. a) $^1$H NMR spectrum of carbazole initiatior, b) $^1$H NMR spectrum of CP(25), and c) $^1$H NMR spectrum of CP(25)-DPP, with characteristic protons labeled.*

With the confirmed synthesis of a CP macromonomer, the next step was to synthesize a series of CP macromonomers. Four macromonomers were synthesized with degrees of polymerization (DP) ranging from ~10 (CP(10)) to ~75 (CP(75)). To aid characterization of the macromonomers, CP(10) and CP(20) were purified on short $SiO_2$ columns to separate the carbazole-bound and free P3HT; CP(40) and CP(75) were too long to purify by column chromatography and were subjected to Soxhlet extraction, which necessarily meant that both CP and P3HT comprised the polymer mixture. The identity of the macromonomers was verified by $^1$H NMR (Figure 3.9b). In each case, the $^1$H NMR spectra showed slight shifts for the aromatic carbazole protons and tolyl protons (from 2.52 to ~2.65), verifying covalent P3HT attachment. Interestingly, the aromatic and alkyl thiophene peaks for the chromatographed CP and Soxhlet extracted CP are significantly different. Typically, $^1$H NMR spectra of tolyl-initiated P3HT possesses a singlet at 7.00 ppm representing the P3HT aromatic proton and a triplet at ~2.80 ppm corresponding to the two alkyl protons alpha to the thiophene rings (along with a smaller triplet slightly upfield due to the terminal thiophene).[197] These shifts are seen for the longer CP macromonomers. However, in the case of the chromatographed macromonomers, both the thiophene aromatic (7.30 to 7.45 ppm) and aliphatic peaks (2.20 to 2.85 ppm) exhibit a series of chemical shifts that appear to vary by either the length of the P3HT chain or the proximity of the thiophene rings to the carbazole initiator. Similar NMR shifts that vary based upon the distance from a given proton to a functional group have been observed in other polythiophenes; for example, polythiophenes terminated with thiols, selenols, dithiocarbamates, and perfluoroalkyl chains experienced strong proximity-dependent NMR shifts.[219-220]

## 3.3 Macromonomer characterization

The DP of the macromonomers was estimated using $^1$H NMR, GPC and MALDI-TOF and the data is summarized in Table 3.1. The DP was determined from the $^1$H NMR spectra in an analogous way to the method published by Bronstein and Luscombe.[197] In the case of the CP molecule, the sum of the integration of the various peaks from 2.20-2.95 ppm (less the integration of the tolyl peak at 2.63 ppm) was divided by the

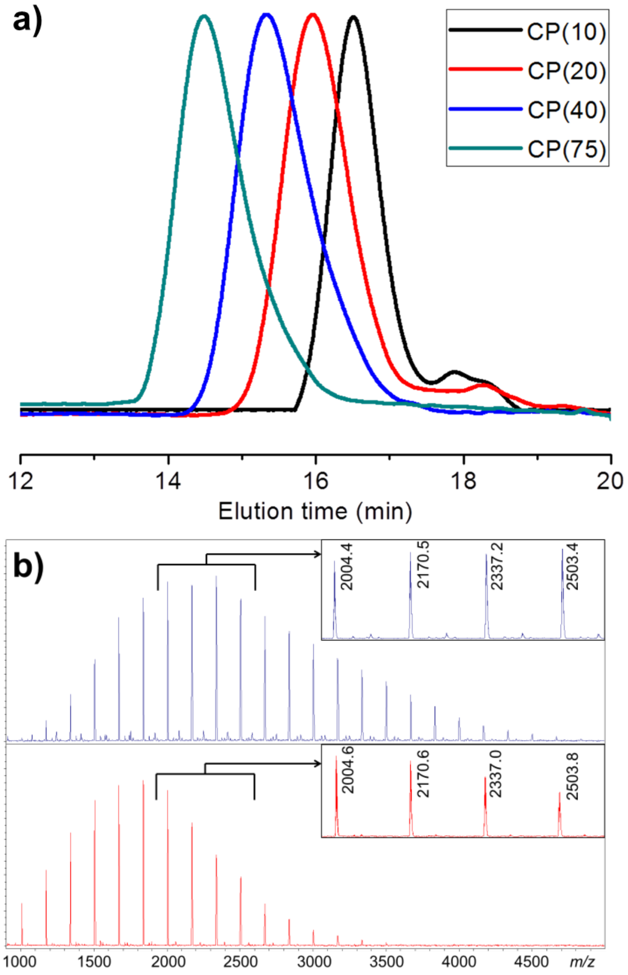

*Figure 3.10: a) GPC traces for macromonomers, b) MALDI-TOF spectra for CP(20) (top) and CP(10) (bottom)*

*Table 1: Physical, optical and electronic characterization of CP macromonomers*

| Polymer | $M_{n,GPC}$ (kDa) | Đ GPC | $M_{n,NMR}$ (kDa) | $M_{n,MALDI\text{-}TOF}$ (kDa) | $\lambda_{max}$ (nm) | $E_{ox}{}^{a}$ (V) | $E_{red}{}^{b}$ (V) | $E_{HOMO}$ (eV) | $E_{LUMO}$ (eV) |
|---|---|---|---|---|---|---|---|---|---|
| CP(10) | 2.1 | 1.34 | 2.6 | 1.8 | 312 | 0.56 | -1.75 | -5.31 | -3.00 |
| CP(20) | 4.1 | 1.41 | 4.4 | 2.8 | 439 | 0.51 | -1.68 | -5.26 | -3.07 |
| CP(40) | 7.7 | 1.53 | 11.3 | - | 446 | 0.47 | -1.63 | -5.22 | -3.12 |
| CP(75) | 13.3 | 1.51 | 15.4 | - | 451 | 0.44 | -1.55 | -5.19 | -3.20 |

[a] *As determined from oxidation onset found by cyclic voltammetry*

[b] *As determined from reduction onset found by cyclic voltammetry*

integration of the tolyl peak, and then multiplied by 1.5 to account for the differing number of protons. Unfortunately, it proved difficult to determine accurate integrations due to the overlapping peaks. As a way to corroborate these $M_n$ values, gel permeation chromatography (GPC) was used. The GPC traces (Figure 3.10a) show a clear progression of the elution time for the four molecules, reflecting the decreasing DP of the macromonomers. Finally, the MALDI-TOF spectra (Figure 3.10b) of CP(10) and CP(20) reveal several insights. As expected, the peaks exhibit the weights of P3HT chains grown from boronic ester-functionalized carbazoles, which are 508.25 g/mol + (166.1 g/mol)*n + 1 g/mol, where n is the number of P3HT repeat units. This confirms that P3HT was grown from the tolyl initiator. In addition, the spectra show nearly complete end-group conversion following acid quenching, with negligible bromine-terminated chains. The MALDI-TOF spectra of CP(40) and CP(75) inaccurately reflected the DP of the polymers. This could be due to the difficulty of volatilizing longer polymers. It has also been reported that MALDI-TOF is inaccurate for polymers with dispersities ($Đ$) > 1.40.[221] The estimated DP of CP(10) and CP(20) based on the MALDI-TOF spectra were 8 and 12, respectively. Given the precise nature of MALDI-TOF, it is expected that the $M_n$ values estimated from those spectra are the most accurate of the three methods used to determine DP. Both the NMR and GPC DP values were higher than the MALDI-TOF values. These discrepancies are likely the result of two main things. GPC has been reported to inflate the weights of conjugated polymers due to their rigid-rod structure compared to the polystyrene standard typically used to calibrate the GPC.[222] In addition, determining the DP from $^1$H NMR is inherently problematic as a result of the overlapping

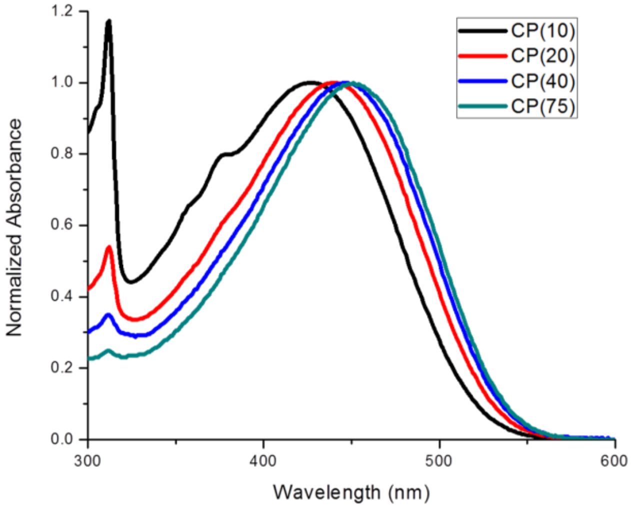

*Figure 3.11: UV-visible spectra of CP(n) macromonomers*

NMR peaks from 2.20-2.95 ppm. Regardless, the DP values are in rough agreement.

Following physical characterization, the optical and electronic properties of the macromonomers were probed using UV-visible spectroscopy and cyclic voltammetry (CV). The UV-visible spectra (Figure 3.11) showed two main transitions corresponding to the π-π* transitions of carbazole and P3HT at ~310 nm and ~450 nm, respectively. The P3HT peak experienced a progressive bathochromic shift as the DP increased, corresponding to the increase in conjugation length. Additionally, increasing the DP of P3HT resulted in a relatively less intense π-π* transition of carbazole, since the carbazole accounts for a smaller proportion of the absorbance of the total macromonomer. The CV spectra (Figure 3.12) show that as the macromonomer DP is increased, the HOMO and LUMO increase and decrease, respectively, generating a smaller bandgap. This is an expected result of increasing the P3HT conjugation length, and corroborates the UV-visible spectra.

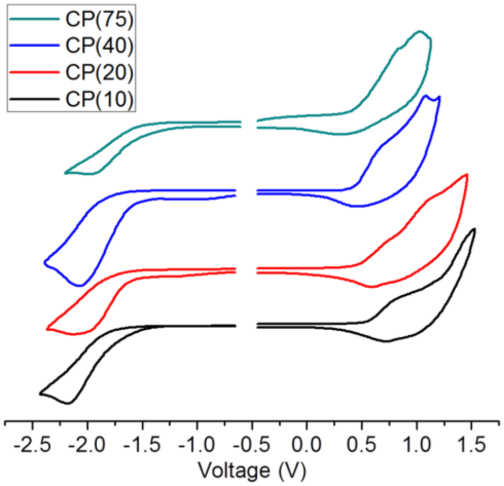

*Figure 3.12: CV scans of CP macromonomers*

### 3.4 Synthesis of Grafted Comb Copolymers

With this series of CP macromonomers in hand, the next step was to determine the conditions necessary for the graft through Suzuki polymerization. Initial attempts utilizing common Suzuki coupling conditions (refluxing toluene or THF, $Pd(PPh_3)_4$, 2 M $K_2CO_3$) yielded mainly starting monomers and some short oligomers. Increasing the reaction duration had no effect on polymer formation. The most plausible reason for this involves the hydrophobicity of the CP macromonomer. Most mechanisms invoked for the Suzuki reaction include the activation of a boronic acid/ester by an aqueous anion. Since the CP molecule is highly hydrophobic, this likely decreases its propensity (and, even more so, the propensity the increasingly hydrophobic coupling products) to enter the aqueous phase, which hindered the activation of the terminal boronic esters. The use of phase-transfer catalysts (Aliquat 336) and water-miscible organic solvents with relatively high boiling points (dioxane) slightly improved the polymerization. However, 18-crown-6, a cyclic ether, was the single most important cocatalyst for the polymerization.

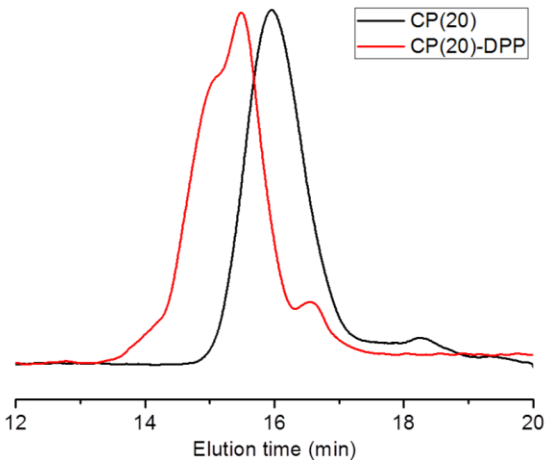

*Figure 3.13. GPC elution profiles for CP(20) and CP(20)-DPP*

### 3.5 Characterization of Grafted Comb Copolymers

Subsequently, the four CP macromonomers were copolymerized with DPP using identical conditions, followed by Soxhlet extraction. A CbzDPP D-A copolymer was synthesized using the same conditions for reference. The resultant polymers were again characterized with $^1$H NMR, GPC, MALDI-TOF, UV-visible spectroscopy and CV and the results are summarized in Table 3.2. The NMR spectrum of CP(20)-DPP (Figure 3.9c) exhibits a new peak at ~9.0 ppm, representing the thiophene proton adjacent to the diketopyrrolopyrrole unit, which confirms the covalent attachment of the DPP monomer; this signal is also present in reference polymer CbzDPP and the other comb copolymers. As can be seen from the CbzDPP spectrum, the multiplet of peaks from 7.30-7.75 ppm in the comb copolymer spectra arise from the carbazole moiety. Interestingly, the thiophene aromatic protons consistently shift upfield to 7.00 ppm for all the comb copolymers. Also, the series of multiplets in the CP(10) and CP(20) spectra from 2.20 to 2.95 ppm coalesce into a single triplet centered at 2.82 ppm in the spectra of CP(10)-DPP and CP(20)-DPP. Another notable feature of the NMR is the shift of the tolyl protons from

*Table 3.2: Physical, optical and electronic characterization of CP-DPP comb copolymers*

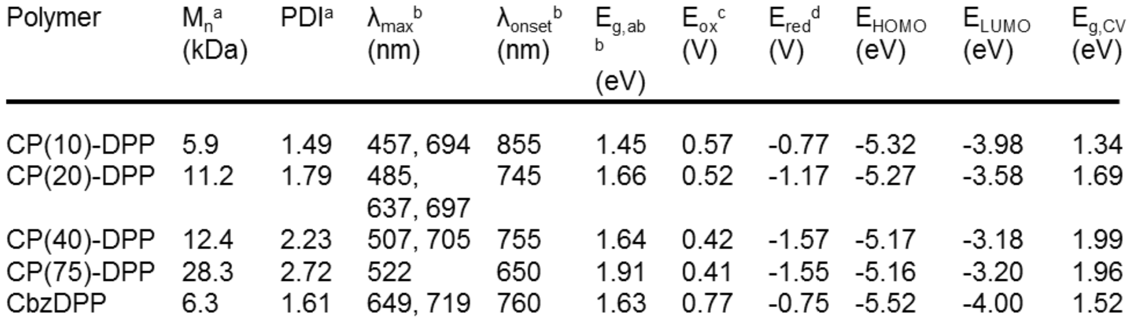

| Polymer | $M_n$[a] (kDa) | PDI[a] | $\lambda_{max}$[b] (nm) | $\lambda_{onset}$[b] (nm) | $E_{g,ab}$[b] (eV) | $E_{ox}$[c] (V) | $E_{red}$[d] (V) | $E_{HOMO}$ (eV) | $E_{LUMO}$ (eV) | $E_{g,CV}$ (eV) |
|---|---|---|---|---|---|---|---|---|---|---|
| CP(10)-DPP | 5.9 | 1.49 | 457, 694 | 855 | 1.45 | 0.57 | -0.77 | -5.32 | -3.98 | 1.34 |
| CP(20)-DPP | 11.2 | 1.79 | 485, 637, 697 | 745 | 1.66 | 0.52 | -1.17 | -5.27 | -3.58 | 1.69 |
| CP(40)-DPP | 12.4 | 2.23 | 507, 705 | 755 | 1.64 | 0.42 | -1.57 | -5.17 | -3.18 | 1.99 |
| CP(75)-DPP | 28.3 | 2.72 | 522 | 650 | 1.91 | 0.41 | -1.55 | -5.16 | -3.20 | 1.96 |
| CbzDPP | 6.3 | 1.61 | 649, 719 | 760 | 1.63 | 0.77 | -0.75 | -5.52 | -4.00 | 1.52 |

2.63 to 2.05 ppm. This shift reveals the sharp triplet at 2.64 ppm, corresponding to the α-protons of the terminal thiophene ring. Calculating the DP based on the integration of the α-protons at 2.82 and 2.64 ppm and the tolyl protons at 2.05 ppm reveals a DP of ~18, as expected. The $^1$H NMR spectra for the comb copolymers (Figures S8-S11) show nearly identical shifts of the carbazole/P3HT aromatic/aliphatic protons and broadly similar features. Unfortunately, the integration of the DPP protons reveal that the DPP monomer is not incorporated stoichiometrically; generally, the carbazole to DPP ratio ranges from 2:1 to 4:1. This suggests that the Suzuki polymerization did not work optimally. As predicted by the Carrothers equation, the achievable DP of step-growth polymerizations are dictated by how precisely the monomers can be measured stoichiometrically. Both the difficulty of determining a precise molecular weight for the CP macromonomers and their Gaussian distribution of molecular weights make it nearly impossible to achieve maximal DP.

The GPC traces of the polymers exhibit shoulders at shorter elution times, which are characteristic of higher molecular weight molecules created by step-growth polymerizations. CP(10)-DPP and CP(20)-DPP (Figure 3.13) elute significantly more quickly than their precursor macromonomers; conversely, the elution profiles of CP(40)-

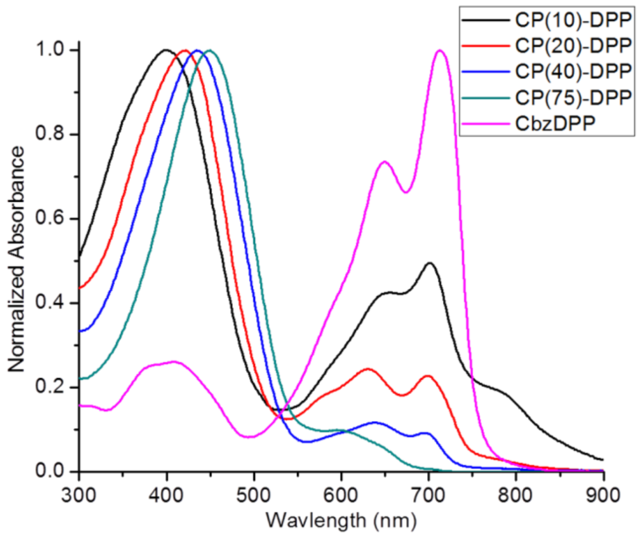

*Figure 3.14: UV-visible $CHCl_3$ solution spectra for CP-DPP comb copolymers and CbzDPP reference*

DPP (Figure S13) and CP(75)-DPP overlap more closely with that of their precursor macromonomers. These results can be explained by the fact that CP(40)-DPP and CP(75)-DPP contain P3HT from the macromonomer synthesis, which remains unmodified after the Suzuki polymerization.

The absorbance characteristics of the comb copolymers were characterized by UV-visible spectroscopy in solution (Figure 3.14) and thin film (Figure 3.15), with the solution spectrum of the CbzDPP copolymer for reference in each case. Generally, each comb copolymer possesses a P3HT π-π* transition around 400-450 nm and a CbzDPP donor-acceptor ICT peak from 550-800 nm. The ICT peak of the linear CbzDPP polymer has two main peaks (ca. 650 and 710 nm), which is also reflected in the bimodal ICT peaks of the comb copolymers (except CP(75)-DPP, which shows a small ill-defined ICT peak). Thus, as hypothesized, the carbazole produces a sufficient break in conjugation to realize the optical properties of both components.

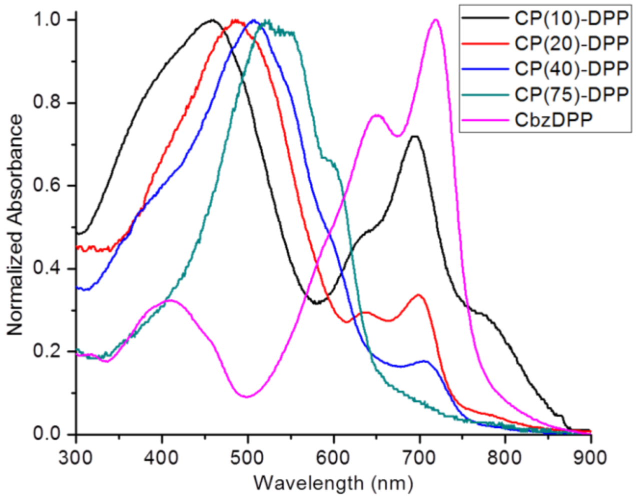

*Figur 3.15: Thin film absorption spectra for comb copolymers and CbzDPP. Films were dropcast from $CHCl_3$ solutions.*

There is a clear trend in the intensity, shape and onset of the ICT peak in the comb copolymers as the P3HT length is varied. As the P3HT side chain was shortened, the ratio of the P3HT π-π* transition intensity to the donor-acceptor ICT peak decreased; conversely, the longer P3HT chains resulted in a more intense P3HT π-π* transition. This phenomenon is similar to the inverse relationship seen between the carbazole and P3HT absorption intensities in the macromonomers. There could be several explanations for this. First and foremost, the CP(40)-DPP and CP(75)-DPP polymers contain P3HT which accounts for some of their absorption around 450 nm. As stated above, this P3HT also results in non-equimolar monomers, which limits the polymerization length and the resultant ICT intensity. It is also possible that the relative amount of P3HT and donor-acceptor polymer dictates the absorption profile – i.e., as the P3HT chain becomes shorter and the π-π* transition becomes weaker, the donor-acceptor peak becomes more prominent and *vice versa*. The longer CP macromonomers undoubtedly produce more

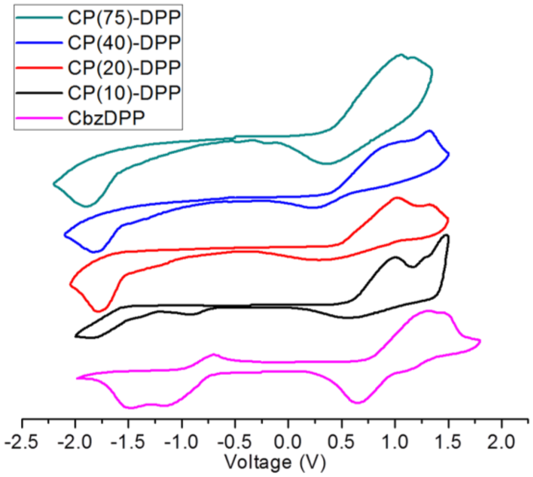

*Figure 3.16: Cyclic voltammetry of CP-DPP comb copolymers and CbzDPP*

steric congestion during the Suzuki polymerization and limit the length of the donor-acceptor polymer.

Regardless, there is clearly an inverse relationship between the length of the CP macromonomers and the onset and relative intensity of the ICT peak in the comb copolymers. This trend is supported by results from recent studies on D-A copolymers incorporating thienylated benzodithiophene donors, which have shown that adding pendant thiophene rings to the donor generates an increasingly strong electronic transition around 400 nm.[223-225] Also of interest is that the ICT peaks of CP(10)-DPP and CP(20)-DPP both exhibit a shoulder at longer wavelengths. The thin film absorbance showed similar trends compared to the solution measurements, with slight broadening of the peaks and bathochromic shifts of both the P3HT π-π* transition and ICT peaks.

The electronic behavior and energy levels of the comb copolymers were further investigated by CV (Figure 3.16). The formation of the CbzDPP backbone changes the electronics of the graft polymers compared to their macromonomers. Generally, each comb copolymer exhibits electronic characteristics of both P3HT and CbzDPP, with the electronic processes of P3HT being much more significant than those of CbzDPP.

Additionally, the greater the relative proportion of CbzDPP in the final comb copolymer, the more drastic the changes in the CV scan contours. Thus, while the scans for CP(75)-DPP appear nearly identical to the CP(75) macromonomer scans in both shape and position, the copolymers with shorter P3HT chains showed a significant departure from their macromonomer CV scans. In all cases, the redox processes of P3HT and CbzDPP seem to be largely independent from each other. For example, both CP(10)-DPP and CbzDPP have reduction onsets that are nearly identical and possess two reduction peaks ca. -0.75 V and -1.25 V. However, CP(10)-DPP still exhibits a large P3HT reduction at nearly the same potential as the CP(10) macromonomer. The covalent attachment of DPP has a much smaller effect on the reduction scans of the other comb copolymers, appearing as a slight change in the slope of the reduction curve; this change of slope is nearly absent from CP(75)-DPP. The onset oxidation potentials of the comb copolymers are nearly identical to those of their respective macromonomer. This can be explained by the fact that the P3HT oxidation occurs at lower potentials than carbazole, so the onset potential of the comb copolymer is dictated by the P3HT chain. Unlike the macromonomers, the comb copolymers all have two or more quasi-reversible oxidation events, presumably corresponding to the sequential oxidation of the P3HT side chains and CbzDPP backbones. Finally, the band gap energies calculated from the oxidation/reduction onsets are in rough agreement with the band gap energies calculated from the thin film absorption onsets. The one exception is that of CP(40)-DPP; although the UV-visible spectrum shows a clear ICT peak, the reduction is so slight in the CV spectrum that the P3HT reduction potential was used to calculate the LUMO level.

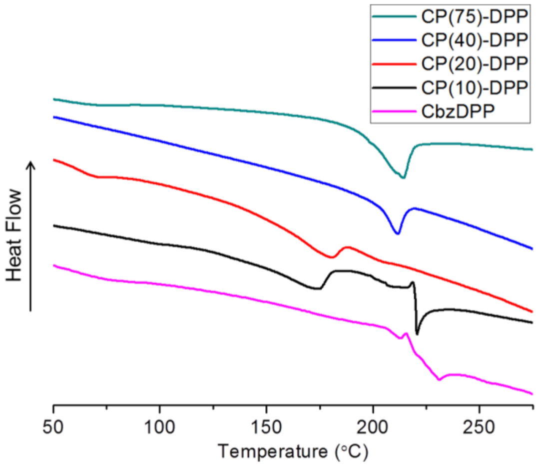

*Figure 3.17: Differential scanning calorimetry of CP-DPP comb copolymers and CbzDPP*

The thermal behaviors of the polymers were characterized by differential scanning calorimetry (DSC). Figure 3.17 shows typical thermograms of each material. CbzDPP shows a melting point ($T_m$) of 231 °C. The CP-DPP polymers show decreasing P3HT $T_m$ of 217, 211, 180, and 174 °C with decreasing P3HT length. It is known that longer P3HT chains exhibit stronger intermolecular interactions than shorter P3HT chains, which would explain the increasing $T_m$ values with increasing molecular weight.[226] This stronger intermolecular interaction is also reflected in the thin film absorption spectra. As the P3HT chain increases in length, a more defined low-energy vibronic shoulder appears on the main P3HT π-π* transition, which results from ordered packing in the solid state. Also of note is that CP(10)-DPP possesses a second $T_m$ at 215 °C, which is likely due to the higher proportion of CbzDPP in the final comb polymer.

### 3.6 Field Effect Transistor Performance of Grafted Comb Copolymers

Finally, the free-charge carrier mobilities of each polymer were determined from organic field effect transistors (OFETs) and the microstructures of the optimized OFETs were characterized by atomic force microscopy (AFM) (see Figures 8.1 to 8.5 in

Appendix). To fabricate optimized OFET devices, the spincoating solvent, spincoating speed, and annealing temperature were varied. Optimized devices were processed from chloroform, spun at 2000 rpm, with the comb copolymers and CbzDPP being annealed at 65 °C and 155 °C, respectively. AFM images and the OFET transfer and output curves for CP(75)-DPP, CP(10)-DPP and CbzDPP are shown in Figures 3.18 to 3.22.

The optimized OFET mobilities seem to reflect the polymer composition. The device properties of the comb polymers with P3HT suffered relative to those of the neat CbzDPP polymer. Both CP(10)-DPP and CbzDPP exhibit similar ambipolar properties, with the addition of the small amount of P3HT only slightly reducing the hole mobility from $7 \times 10^{-3} \pm 2 \times 10^{-3}$ $cm^2V^{-1}s^{-1}$ for CbzDPP to $5 \times 10^{-3} \pm 3\times10^{-3}$ $cm^2V^{-1}s^{-1}$ for CP(10)-DPP. They both have similar electron mobilities of $7 \times 10^{-4} \pm 2 \times 10^{-4}$ $cm^2V^{-1}s^{-1}$ for CbzDPP and $7 \times 10^{-4} \pm 3 \times 10^{-4}$ $cm^2V^{-1}s^{-1}$ for CP(10)-DPP. The surface morphology of these materials shows reduced domain sizes for CP(10)-DPP relative to CbzDPP; this is expected due to an increase in disorder in the P3HT containing system. Further increasing the concentration of P3HT to CP(20)-DPP and CP(40)-DPP results in devices that do not work well for transistor applications; CP(20)-DPP did not turn on and CP(40)-DPP yielded devices with barely measurable output curves (not shown). Further increasing the P3HT concentration to CP(75)-DPP results in p-type transistors with mobilities of $6 \times 10^{-4} \pm 1 \times 10^{-4}$ $cm^2V^{-1}s^{-1}$. This likely arises due to favorable π-π interactions between the longer P3HT chains, and minimal contribution from the CbzDPP copolymer. These films also show domains with dimensions similar to those of CP(10)-DPP. Overall, it appears that there is a general trend of transport properties being derived from the CbzDPP backbone with short P3HT chains, followed by a disruption in the electronic structure with increasing P3HT lengths, before the transport properties become dominated by P3HT interactions.

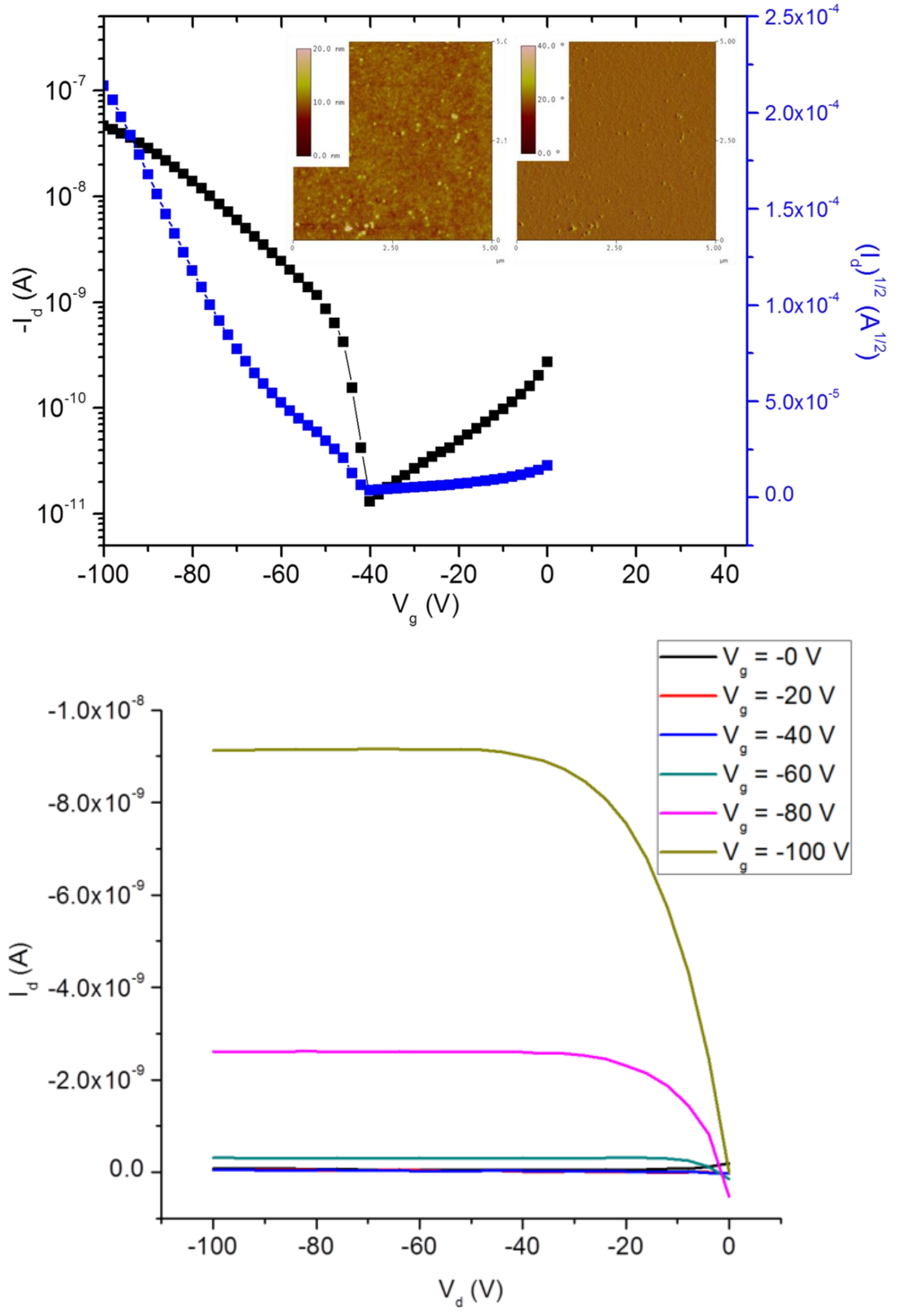

*Figure 3.18: Top: transfer curves for CP(75)-DPP. Inset: height (left) and phase (right) AFM images. Bottom: output curves for CP(75)-DPP*

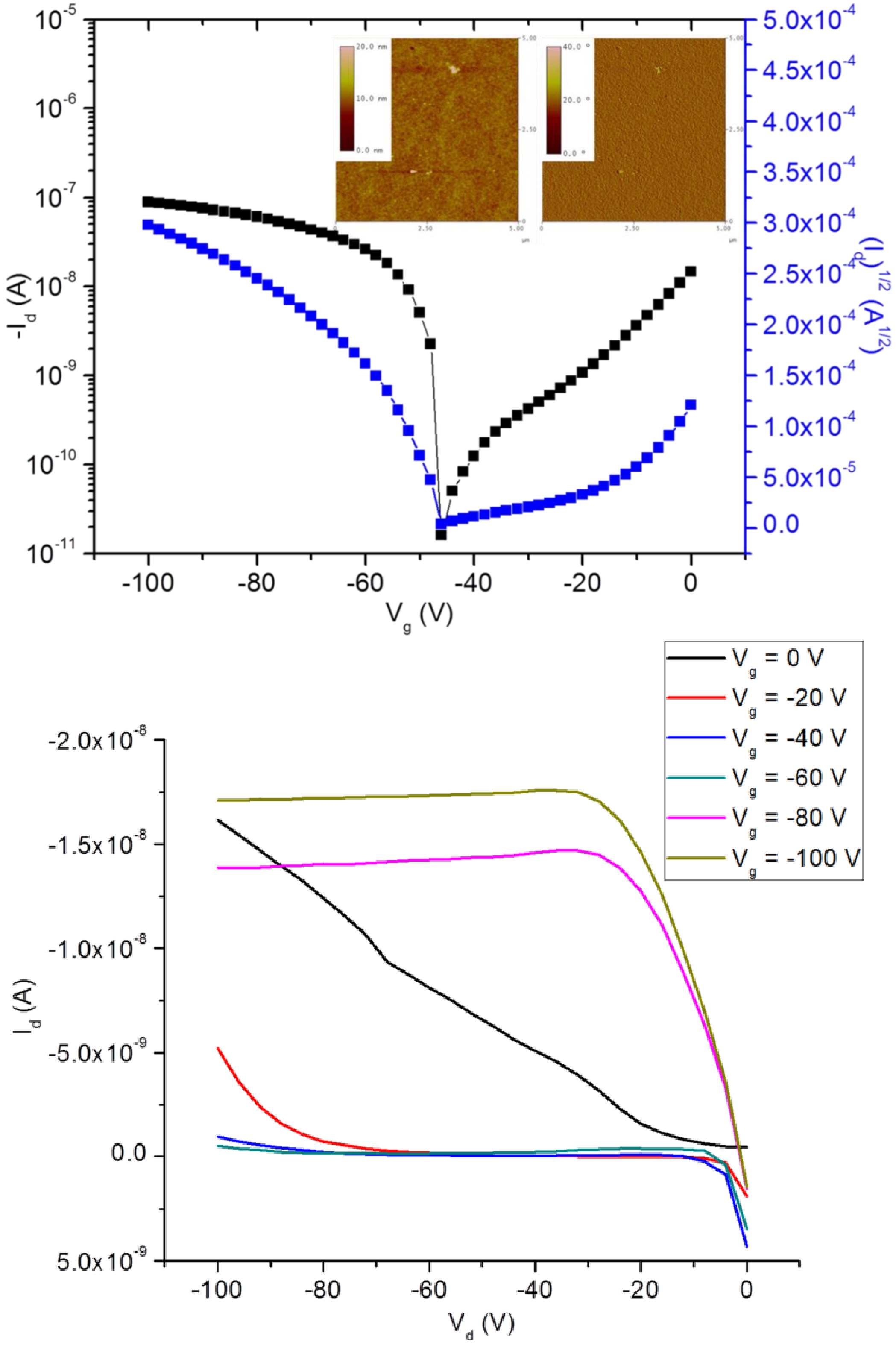

*Figure 3.19: Top: p-type transfer curves for CP(10)-DPP. Inset: height (left) and phase (right) AFM images. Bottom: p-type output curves for CP(10)-DPP*

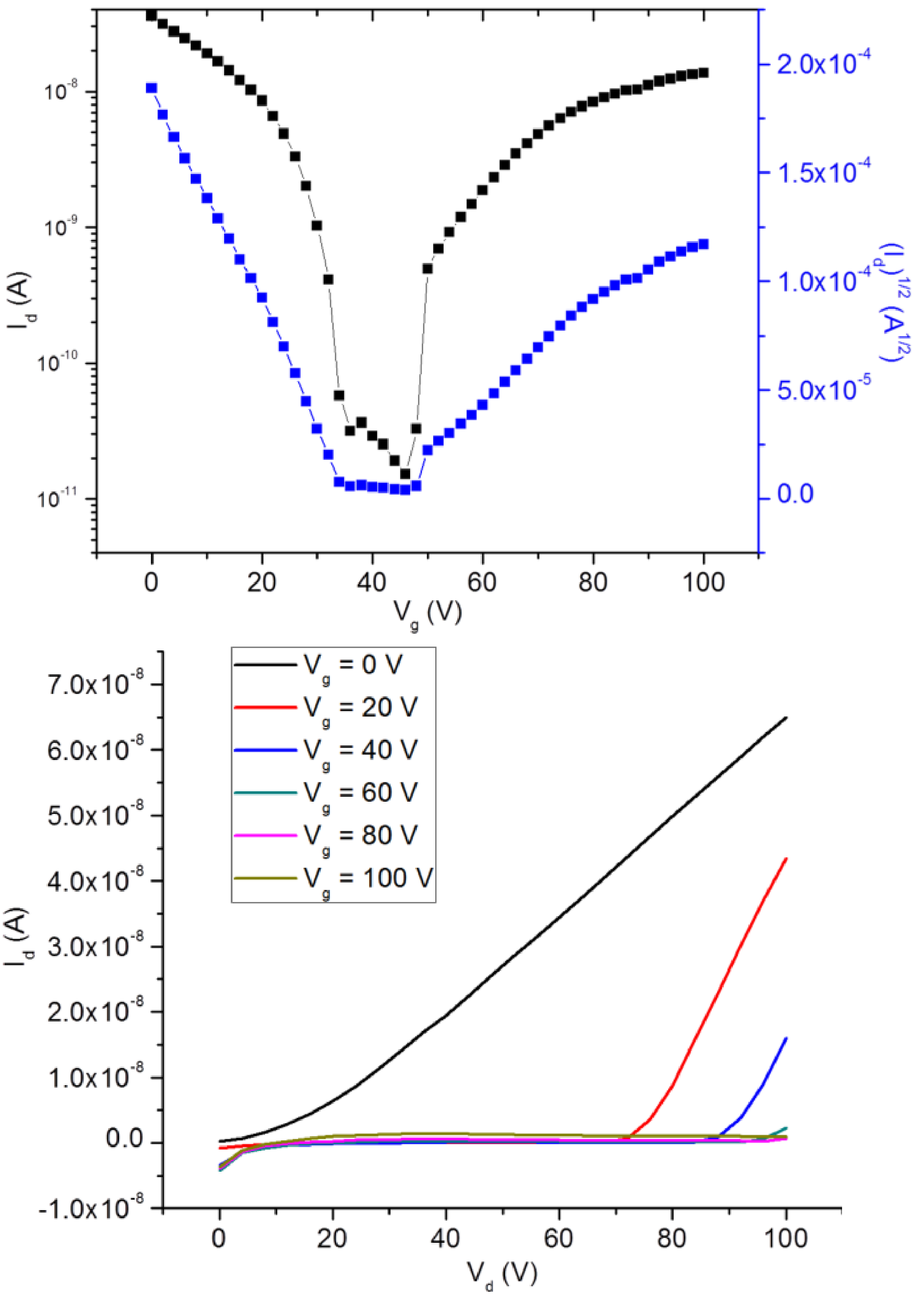

*Figure 3.20: Top: n-type transfer curves for CP(10)-DPP. Bottom: n-type output curves for CP(10)-DPP*

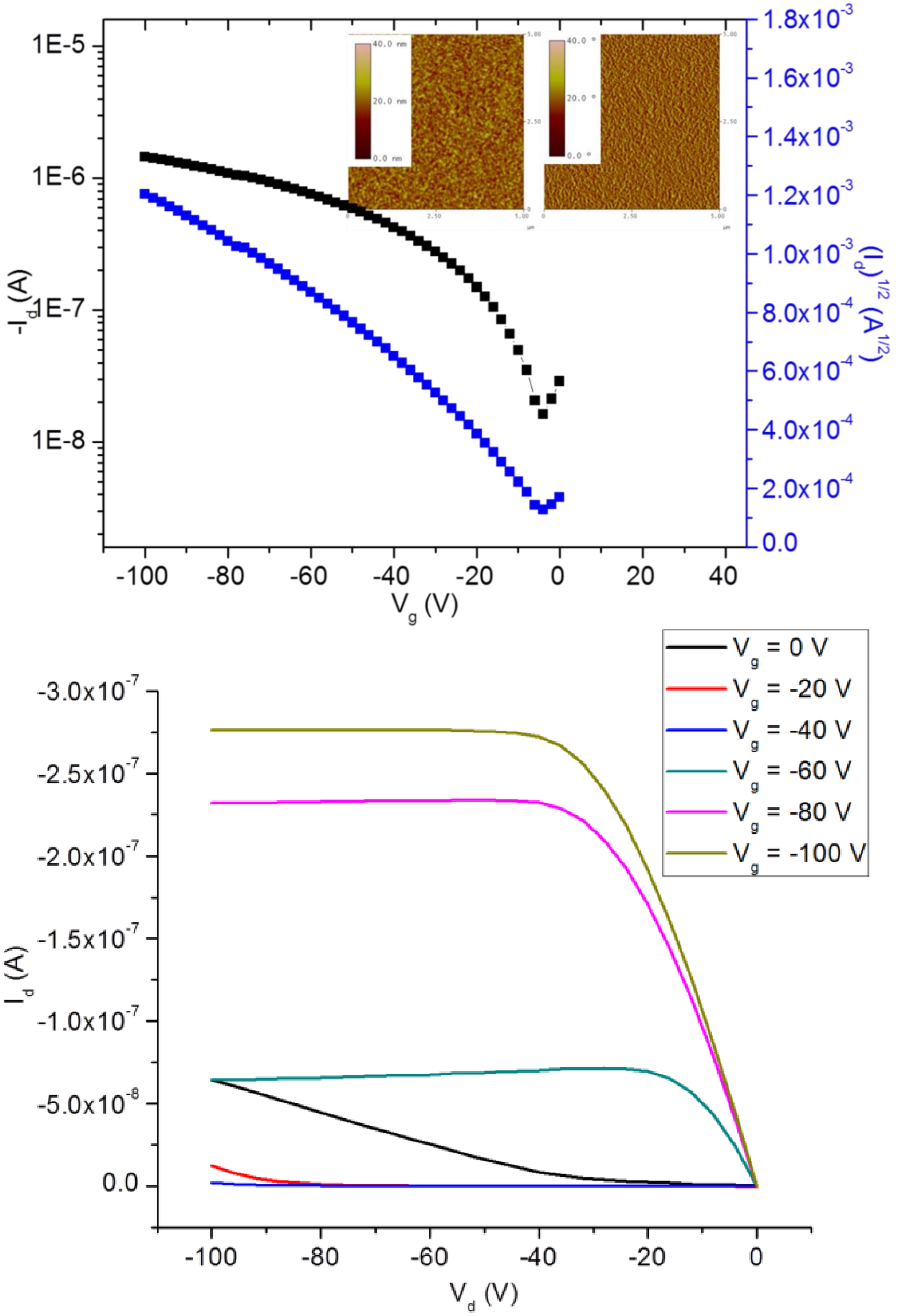

*Figure 3.21: Top: p-type transfer curves for CbzDPP. Inset: height (left) and phase (right) AFM images. Bottom: p-type output curves for CbzDPP.*

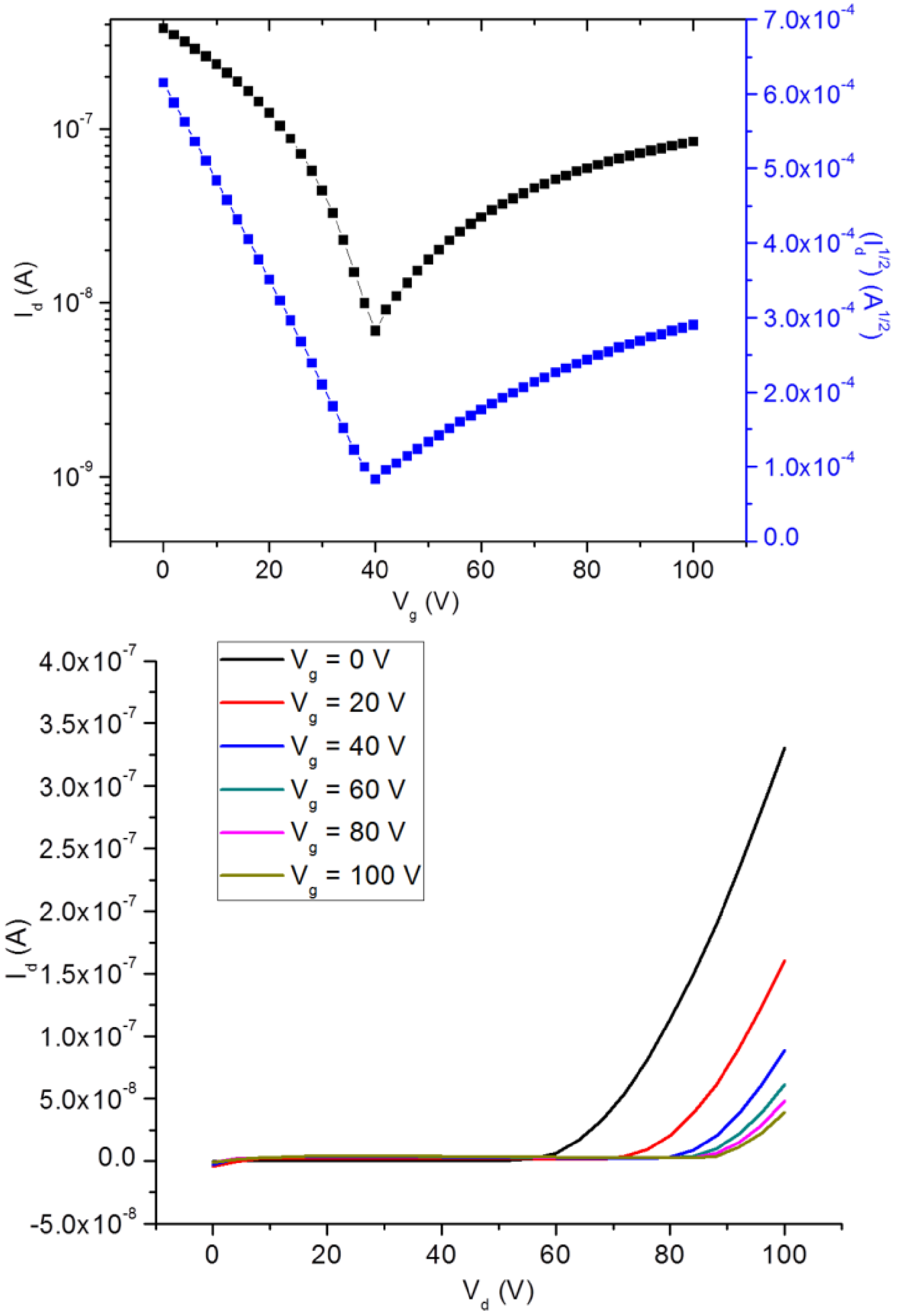

*Figure 3.22: Top: n-type transfer curves for CbzDPP. Bottom: n-type output curves for CbzDPP.*

### 3.7 Conclusions

A synthetic methodology was pioneered and optimized to realize the first example of a “graft through” approach to attain conjugated comb co-polymers. In addition, a new carbazole-based external initiating moiety was discovered for P3HT synthesis, which resulted in controllable growth of P3HT. A Suzuki polymerization involving this carbazole-P3HT macromonomer and a diketopyrrolopyrrole acceptor was optimized. Thereafter, four iterations of a carbazole-P3HT-diketopyrrolopyrrole comb copolymer were synthesized, differing by the degree of polymerization of the P3HT chain. The final polymers exhibit two major absorption peaks due to the P3HT π-π* transition and ICT between carbazole and diketopyrrolopyrrole units. Moreover, the relative intensities of peaks were proportional to the relative amount of P3HT and donor-acceptor copolymer.

Clearly, the main two drawbacks of this approach are: 1) the conditions required to realize the oxidative addition reaction during the *ex situ* catalyst formation and 2) the mandatory use of a graft through polymerization. Both of these limitations are a result of the initiator design. The functionalized carbazole has a large electronic effect at the site of the oxidative addition, thereby disfavoring the reaction. In the case of the boronic-ester functionalized carbazole, this generates byproducts during catalyst formation and ultimately leads to a P3HT impurity, as well as P3HT lengths that differ significantly from the predicted lengths; alternatively, in the case of the graft from approach, the carbazole-diketopyrrolopyrrole D-A polymer is sufficient to completely retard the oxidative addition reaction. Unfortunately, the graft from approach is preferable to the graft through approach in this system because of the nature of step-growth and chain-growth polymerizations. The macromonomers for the graft through approach necessarily have a Gaussian distribution of molecular weights, which makes achieving a perfect 1:1 stoichiometric ratio during the Suzuki polymerization nearly impossible. This thereby limits the efficiency and reproducibility of the Suzuki polymerization. If such systems could be designed to improve the efficiency of the catalyst formation and P3HT grafting reaction, it would be interesting to utilize other conjugated molecules as initiators in P3HT synthesis to probe the way they affect the optical, electronic, and self-assembly properties of conjugated materials.

### 3.8 Experimental

**Materials and Characterization.** Unless otherwise specified, all chemicals were purchased from Aldrich and used without further purification. Solvents for synthesis were purified by distillation. All chemical reactions were carried out in a nitrogen atmosphere. 2,7-dibromocarbazole,[227] 1-iodo-2-octyldodecane,[228] 3,6-bis(5-bromothiophen-2-yl)-2,5-bis(2-octyldodecyl)pyrrolo[3,4-c]pyrrole-1,4(2H,5H)-dione[228] and 9-phenyl-2,7-dibromocarbazole[227] were prepared according to published procedures. UV-visible spectra were tested using a Perkin-Elmer Lambda-9 spectrophotometer. $^{1}$H-NMR and $^{13}$C-NMR spectra were collected on Bruker AV 300 or 500 spectrometers operating at 300 or 500 MHz in deuterated chloroform solution with TMS as reference. Polymer molecular weights were measured by a Waters 1515 gel permeation chromatograph (GPC) with a refractive index detector at room temperature (THF as the eluent). Cyclic voltammetries of polymer films were conducted on a BAS CV-50W voltammetric system with a three-electrode cell in acetonitrile with 0.1 M tetrabutylammonium hexafluorophosphate ($Bu_4NPF_6$) using a scan rate of 50 $mV \cdot s^{-1}$. ITO, Ag/AgCl and Pt wire were used as working electrode, reference electrode and counter electrode, respectively. Differential scanning calorimetry was performed with a TA Instruments Auto Q20 using a heating rate of 5 °C/min. All AFM images were recorded in tapping mode on a Nanoscope II Scanning Probe Microscope (Digital Instruments). All spectra were plotted using OriginPro 8.

**OFET device fabrication**. Organic field-effect transistors were fabricated in a top-contact bottom-gate device geometry on heavily doped p-type silicon <100> wafers with a 300 nm thermal oxide layer, purchased from Montco Silicon Technologies. Substrates were cleaned by sequential ultrasonication twice with fresh acetone, followed by isopropyl alcohol for 15 min each. They were then dried under a stream of nitrogen and treated by air plasma for 15 min before passivating the oxide layer with a thin divinyltetramethyldisiloxane-bis(benzocyclobutene) (BCB, Dow Chemicals, Inc.) buffer layer. A precursor solution of 1 wt% BCB in toluene was spin coated in air at 4000 rpm for 60 s on the oxide layer. The substrates were subsequently annealed at 250 °C overnight in a glove box. Solutions of each polymer were prepared in chloroform ($CHCl_3$) and chlorobenzene (CB) at concentrations of 5 mg/mL and allowed to stir in a glovebox over night before filtering with a 0.2 um PTFE filter. Filtered solutions were then spin coated on BCB passivated substrates at 2000, 3000, or 4000 rpm for 60 s. The best device performances were found for OFETs made in $CHCl_3$ and spin coated at 2000 rpm. These thin films were annealed at 65, 95, 125, and 155 °C for 10 min under nitrogen prior to electrode deposition in order to determine their optimal device performance conditions. Gold source and drain electrodes were thermally evaporated through a shadow mask at a base pressure of $7 \times 10^{-7}$ Torr at a rate of 1 Å/s to a thickness of 50 nm. The output and transfer characteristics of all transistors were measured in a nitrogen atmosphere using an Agilent 4155B semiconductor parameter analyzer. The field-effect mobility (μ) was determined from a linear fit of $(I_{ds})^{1/2}$ vs $V_{gs}$ in the saturation regime. The threshold voltage ($V_t$) was estimated from the x-intercept of the linear region of $(I_{ds})^{1/2}$ vs $V_{gs}$. All devices had a channel length of 100 μm and a channel width of 1000 μm.

**Synthesis of 2,7-dibromo-9-(4-chloro-3-methylphenyl)-9H-carbazole (1).** 2,7-dibromocarbazole (1.56 g, 4.8 mmol), 1-chloro-4-iodo-2-methylbenzene (3.65 g, 14.5 mmol), copper(I) iodide (0.14 g, 0.7 mmol), 1,10-phenanthroline (0.13 g, 0.7 mmol), and potassium carbonate (1.00 g, 7.2 mmol) were added to a 100 mL one-neck flask. Then, DMF (20 mL) was added and the mixture was warmed to 125 °C and stirred overnight. After cooling to room temperature, the mixture was poured into water and washed with ether. The combined organic extracts were dried with $Na_2SO_4$ and evaporated under vacuum. The residue was purified via silica gel chromatography (1:40 dichloromethane:hexanes) to yield a white powder (0.81 g, 38%). $^1$H NMR (300 MHz, $CDCl_3$, *δ*): 7.97 (d, 2H, *J* = 9 Hz), 7.85 (d, 1H, *J* = 6 Hz), 7.58-7.68 (m, 2H), 7.35-7.50 (m, 4H), 2.53 (s, 3H). $^{13}$C NMR (500 MHz, $CDCl_3$, *δ*): 130.8, 129.5, 125.9, 123.8, 121.7, 121.5, 118.87, 114.3, 113.0, 70.1, 69.2, 20.2.

**Synthesis of 9-(4-chloro-3-methylphenyl)-2,7-bis(tetramethyl-1,3,2-dioxaborolan-2-yl)-9H-carbazole (2).** Compound 1 (0.68 g, 1.5 mmol) was dissolved in THF (20 mL) and cooled to -78 °C. Then, *n*-butyl lithium (1.26 mL, 3.1 mmol) was added dropwise. The solution was stirred for 1 h. Then, 2-isopropoxy-4,4,5,5-tetramethyl-1,3,2-dioxaborolane (0.59 g, 3.2 mmol) was added in one portion and the mixture was allowed to warm to room temperature and stir overnight. The solution was then washed with water, dried with $Na_2SO_4$ and evaporated under vacuum. The residue was purified via silica gel chromatography (1:1 dichloromethane:hexanes) to yield a white powder (0.62 g, 76%). $^1$H NMR (300 MHz, $CDCl_3$, $\delta$): 8.18 (d, 2H, $J$ = 6 Hz), 7.77 (d, 1H, $J$ = 9 Hz), 7.75 (s, 2H), 7.61 (d, 1H, $J$ = 6 Hz), 7.43 (s, 1H), 7.35 (d, 1H, $J$ = 6 Hz), 2.52 (s, 3H), 1.38 (s, 24H). $^{13}$C NMR (500 MHz, $CDCl_3$, $\delta$): 141.1, 138.1, 136.0, 133.6, 130.6, 130.2, 126.7, 126.1, 125.5, 120.0, 116.0, 83.8, 24.9, 20.3.

**Synthesis of CP macromonomers.** Compound 2 (10 mg, 0.02 mmol), $Ni(COD)_2$ (2.5 mg, 0.01 mmol), and triphenylphosphine (10 mg, 0.04 mmol) were dissolved in toluene (1 mL) in a glovebox. The mixture was heated to 50 °C and stirred at that temperature for 3 days. After cooling to room temperature, 1,3-bis(disphenylphosphino)propane (11 mg, 0.025 mmol) was added and the solution was stirred at r.t. for 3 h. Meanwhile, 2-bromo-5-iodo-3-hexylthiophene was added to a Schlenk flask, and dissolved in THF. After cooling to 0 °C, isopopylmagnesium chloride was added dropwise and the solution was stirred for a further hour. Then, the catalyst solution was transferred out of the glovebox, and injected to the thiophene monomer solution in a single portion. The ice bath was removed and the solution was warmed to r.t. and stirred for 5 h. 5 M HCl was added to quench the reaction. For CP(75) and CP(40), the solution was then poured into MeOH, and the precipitate was filtered. The polymers were then Soxhlet extracted with methanol (12 h), acetone (12 h), hexanes (12 h) and finally $CHCl_3$ (12 h). The $CHCl_3$ fraction was concentrated *in vacuo*, redissolved in $CHCl_3$ and precipitated in MeOH. CP(20) and CP(10) solutions were extracted with $CHCl_3$ and the residue was purified on a short silica gel column (50% DCM:Hexanes to 100% DCM) to yield the final macromonomers.

*CP(10):* Orange tacky solid. Yield: 27%. $^1$H NMR (300 MHz, CDCl$_3$, $\delta$): 8.20 (d, $J$ = 6 Hz), 7.88 (s), 7.79 (d, $J$ = 6 Hz), 7.70 (m), 7.48 (m), 7.45-7.30 (m), 7.10 (d, $J$ = 9 Hz), 7.00 (m), 2.83 (m), 2.64 (s), 2.60 (m), 2.20 (t, $J$ = 9 Hz), 1.70-1.60 (m), 1.5-1.3 (m), 0.93 (m).

*CP(20):* Red solid. Yield: 22%. $^1$H NMR (300 MHz, CDCl$_3$, $\delta$): 8.20 (d, $J$ = 6 Hz), 7.87 (s), 7.75 (m), 7.70 (m), 7.49 (m), 7.45-7.30 (m), 7.10 (d, $J$ = 9 Hz), 7.00 (m), 2.83 (m), 2.63 (s), 2.50 (m), 2.20 (t, $J$ = 9 Hz), 1.75-1.60 (m), 1.5-1.3 (m), 0.94 (m).

*CP(40):* Dark solid. Yield: 65%. $^1$H NMR (300 MHz, CDCl$_3$, $\delta$): 8.20 (d, $J$ = 6 Hz), 7.87 (s), 7.79 (d, $J$ = 6 Hz), 7.72 (d, $J$ = 9 Hz), 7.48 (m), 7.1 (m), 7.00 (s), 6.92 (m), 2.83 (t, $J$ = 6 Hz), 2.64 (s), 1.73 (m), 1.5-1.3 (m), 0.94 (m).

*CP(75):* Dark solid. Yield: 71%. $^1$H NMR (300 MHz, CDCl$_3$, $\delta$): 8.20 (d, $J$ = 6 Hz), 7.87 (s), 7.70 (m), 7.45 (mz), 7.26 (m), 7.00 (s), 2.83 (t, $J$ = 6 Hz), 2.63 (m), 1.73 (m), 15-1.25 (m), 0.94 (m).

**Synthesis of CP-DPP polymers.** The appropriate CP macromonomer (1.0 mmol, based on M$_n$ determined by MALDI-TOF for CP(10) and CP(20) or GPC for CP(40) and CP(75)), DPP monomer (1.0 mmol), 18-cown-6 (2.0 mmol), and Aliquat 336 (20 mol %) were added to a flask and degassed three times. Then, degassed toluene (5 mL) and 2M K$_2$CO$_3$ (0.5 mL) were added, followed by Pd(PPh$_3$)$_4$ (5 mol %). The solution was heated to 110 °C and stirred for 3 days. The solution was cooled to room temperature and poured into MeOH. The precipitate was filtered and the polymers were then Soxhlet extracted with methanol (12 h), acetone (12 h), hexanes (12 h) and finally CHCl$_3$ (12 h). The CHCl$_3$ fraction was concentrated *in vacuo*, redissolved in CHCl$_3$ and precipitated in MeOH

*CP(10)-DPP:* Dark solid. Yield: 73%. $^1$H NMR (300 MHz, $CDCl_3$, $\delta$): 9.00 (s), 8.20 (m), 7.75-7.40 (m), 6.99 (s), 6.92 (s), 2.82 (m), 2.64 (m), 2.06 (s), 1.80-1.10 (m), 0.93 (m).

*CP(20)-DPP:* Dark solid. Yield: 69%. $^1$H NMR (300 MHz, $CDCl_3$, $\delta$): 8.97 (s), 8.17 (m), 7.75-7.60 (m), 7.55-7.35 (m), 7.00 (s), 6.92 (s), 2.82 (t, $J$ = 6 Hz), 2.64 (t, $J$ = 6 Hz), 2.06 (s), 1.80-1.57 (m), 1.50-1.00 (m), 0.93 (m).

*CP(40)-DPP:* Dark solid. Yield: 86%. $^1$H NMR (300 MHz, $CDCl_3$, $\delta$): 8.97 (s), 8.20-8.10 (m), 7.80-7.60 (m), 7.55-7.40 (m), 7.00 (s), 6.92 (s), 2.82 (t, $J$ = 6 Hz), 2.63 (t, $J$ = 6 Hz), 2.06 (s), 1.80-1.55 (m), 1.50-1.00 (m), 0.93 (m).

*CP(75)-DPP:* Dark solid. Yield: 83%. $^1$H NMR (300 MHz, $CDCl_3$, $\delta$): 8.97 (s), 8.16 (m), 7.65-7.45 (m), 7.00 (s), 6.93 (s), 2.82 (t, $J$ = 6 Hz), 2.06 (s), 1.80-1.60 (m), 1.50-1.20 (m), 0.93 (m).

**Synthesis of 9-phenyl-2,7-bis(4,4,5,5-tetramethyl-1,3,2-dioxaborolan-2-yl)-9H-carbazole (3).** 9-phenyl-2,7-dibromocarbazole (0.41 g, 1.0 mmol) was dissolved in THF (15 mL) and cooled to -78 °C. Then, *n*-butyl lithium (0.86 mL, 2.1 mmol) was added dropwise. The solution was stirred for 1 h. Then, 2-isopropoxy-4,4,5,5-tetramethyl-1,3,2-dioxaborolane (0.42 g, 2.2 mmol) was added in one portion and the mixture was allowed to warm to room temperature and stir overnight. The solution was then washed with water, dried with $Na_2SO_4$ and evaporated under vacuum. The residue was purified via silica gel chromatography (1:1 dichloromethane:hexanes) to yield a white powder (0.42 g, 83%). $^1$H NMR (300 MHz, $CDCl_3$, $\delta$): 8.16 (d, 2H, $J$ = 6 Hz), 7.81 (s, 2H), 7.75 (d, 1H, $J$ = 9 Hz), 7.65-7.50 (m, 1H, $J$ = 6 Hz), 1.33 (s, 24H). $^{13}$C NMR (500 MHz, $CDCl_3$, $\delta$): 140.5, 138.6, 135.8, 131.1, 129.6, 128.9, 126.4, 125.5, 120.0, 116.0, 85.9, 25.1.

**Synthesis of CbzDPP.** Cbz monomer (0.24 g, 0.5 mmol), DPP monomer (0.49 g, 0.5 mmol), 18-cown-6 (0.256 g, 1.0 mmol), and Aliquat 336 (0.04 g, 0.1 mmol) were added to a flask and degassed three times. Then, degassed toluene (3 mL) and 2M $K_2CO_3$ (0.25 mL) were added, followed by $Pd(PPh_3)_4$ (0.03 g, 0.02 mmol). The solution was heated to 110 °C and stirred for 3 days. The solution was cooled to room temperature and poured into MeOH. The precipitate was filtered and the polymer was Soxhlet extracted with methanol (12 h), acetone (12 h), hexanes (12 h) and finally $CHCl_3$ (12 h). The $CHCl_3$ fraction was concentrated *in vacuo*, redissolved in $CHCl_3$ and precipitated in MeOH to give a dark solid. Yield: 81%. $^1$H NMR (300 MHz, $CDCl_3$, $\delta$): 8.98 (s), 8.16 (br), 7.75-7.45 (m), 1.40-1.05 (m), 0.83 (m).

# 4. Design and Synthesis of Dyes for Energy-Harvesting Electrochromic Windows

## 4.1 Introduction

Around the same time that OPV cells started receiving widespread attention, the first modern dye-sensitized solar cell (DSSC) was made by Brian O’Regan and Michael Grätzel.[229] Much like OPV devices, DSSCs are attractive alternatives to conventional inorganic solar cells. They are less expensive than inorganic cells, easy to fabricate using roll-to-roll processing, and reasonably efficient.[230]

Essentially, a modern DSSC consists of several parts (Figure 4.1). One electrode is a transparent conducting inorganic material (generally fluoride-doped tin oxide) which is coated with a layer of titanium dioxide nanoparticles that have been sintered together to generate a continuous pathway for electrons. This forms a highly porous film with a high surface area. Since $TiO_2$ has a very large $E_g$, it is then coated with a dye (typically ruthenium-based), which, through a carboxyl group, adsorbs onto the $TiO_2$ surface. This electrode is then hermetically sealed with a metal electrode, thereby leaving an interstitial space between the $TiO_2$/dye and metal electrode. This space is infused with a solution containing a redox mediator, which is able to shuttle electrons back and forth between the dye molecules and metal electrode.[231]

During DSSC operation, light enters the cell through the transparent electrode and is absorbed by the dye molecules. Electrons are excited within the dye molecule and are rapidly injected into the conduction band of the $TiO_2$ particles. After the free charge carriers enter the $TiO_2$ particles, they percolate through the film to the transparent conducting electrode. Once they are collected, the charges travel around the circuit and eventually reach the metal electrode. Concurrently, redox mediator molecules diffuse

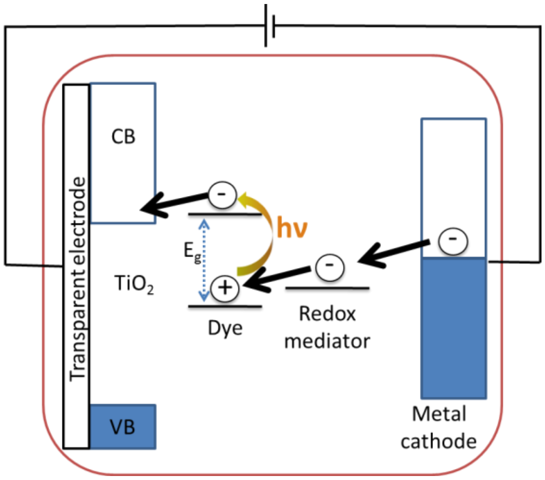

*Figure 4.1: Schematic of DSSC operation*

toward the metal electrode, and are reduced by the free electron. Subsequently, the reduced mediator diffuses back toward the oxidized dye molecules. After encountering an oxidized dye molecule, the redox mediator donates its electron to the dye molecule, returning the molecule to its neutral state.[232-233]

Similar to OPV devices, energy level alignment between the various components is crucial for device function. The dye must have a LUMO above the conduction band edge of $TiO_2$ for efficient dye injection; it must also possess a HOMO below that of the redox potential of the mediator molecule, so the redox mediator can donate an electron to the oxidized dye molecules.[232]

The aim of this project is to use the DSSC architecture to make a bifunctional energy-harvesting electrochromic window (Figure 4.2). The cell would function normally as a DSSC; reversing the current flow would generate an electrochromic color change, thereby making the cell nearly transparent. Practically, this would enable the replacement of windows in buildings with these bifunctional devices. On a sunny day, they could be used to harvest sunlight via DSSC function and limit the use of blinds given their tinted nature; on a cloudy day, an applied bias would activate the electrochromic window and

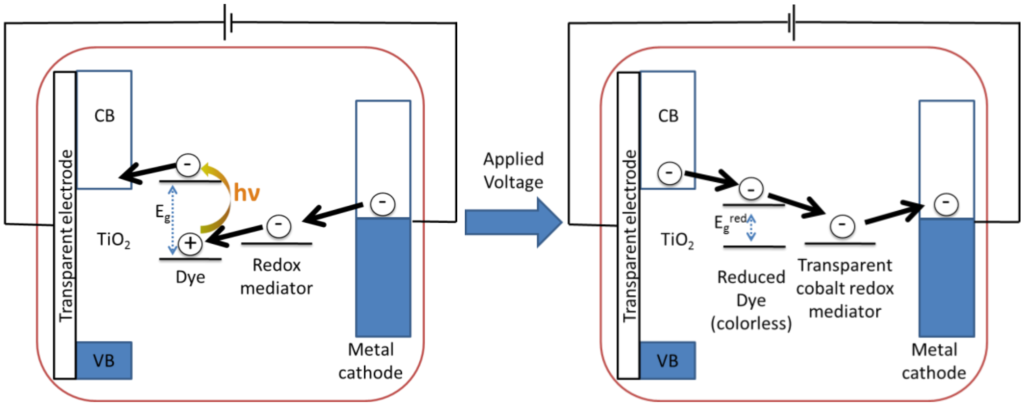

*Figure 4.2: Schematic of bifunctional energy-harvesting electrochromic window, with DSSC function at left and electrochromic window function under applied voltage at right*

allow passive solar heating and lighting of the building. This would negate the squandered energy when blinds reflect solar radiation into space, generating energy instead of wasting it. Only one group has succeeded in fabricating such a bifunctional device, which consisted of a standard DSSC ruthenium dye with a layer of electrochromic $WO_3$ over the cathode. Although this was a proof-of-concept experiment, the resultant devices showed poor PCE values (~0.5%).[234]

However, our goal was significantly more complicated. We sought to discover a bifunctional dye with both light-harvesting ability and electrochromic behavior. This required the design and synthesis of a dye that fulfills the following requirements: 1) the dye must absorb strongly in the visible spectrum when it is in its ground state, 2) the dye must be electrochromic upon reduction, 3) the dye must transition from a tinted state to a nearly transparent state upon reduction, 4) the dye should be stable to repeated oxidation and reduction cycles, and 5) the dye should be bulky to retard aggregation at the $TiO_2$ surface, thereby reducing recombination rates. To do this, a number of dyes were designed and tested for electrochromic behavior, including perylene-, Methylene Blue- and phthalocyanine-based dyes. Thin films of the perylene and Methylene Blue derivatives showed minimal electrochromic behavior. However, of the two phthalocyanine dyes synthesized, one showed electrochromic behavior and one showed near-IR absorbance. The former showed a transition from green to purple in its ground and reduced states, respectively. Unfortunately, the introduction of a chemical anchor proved synthetically challenging. The latter was incorporated into a DSSC for preliminary testing. Although the $V_{oc}$ and FF of the cell were reasonable, the $J_{sc}$ was quite poor (~$10^{-1}$ mA/cm$^2$), which led to trifling PCE values. This likely had to do with a lack of overlap between the dye absorption profile and the incident solar energy spectrum.

### 4.1.1 Redox mediators

As stated above, the role of the redox mediator is to shuttle electrons from the metal cathode to the oxidized dye molecules. The redox diffusion is largely controlled by concentration gradients. Historically, the most common redox electrolyte has been iodide/triiodide ($I^-/I_3^-$).[233,235] However, this electrolyte is intensely colored and almost entirely opaque, which limits its application in an electrochromic window. As a result, the Grätzel group pioneered the use of cobalt complex redox mediators, which are nearly transparent.[236]

### 4.1.2 Dye Sensitizers

There are three main classes of sensitizers for DSSCs: metal-organic complex, organic and quantum dot dyes.[231,237-238] Each dye has several requirements, among which are efficient light absorption (both in terms of absorption coefficient and wavelength distribution), stability to oxidation, and ability to bind to $TiO_2$, as well as inject electrons

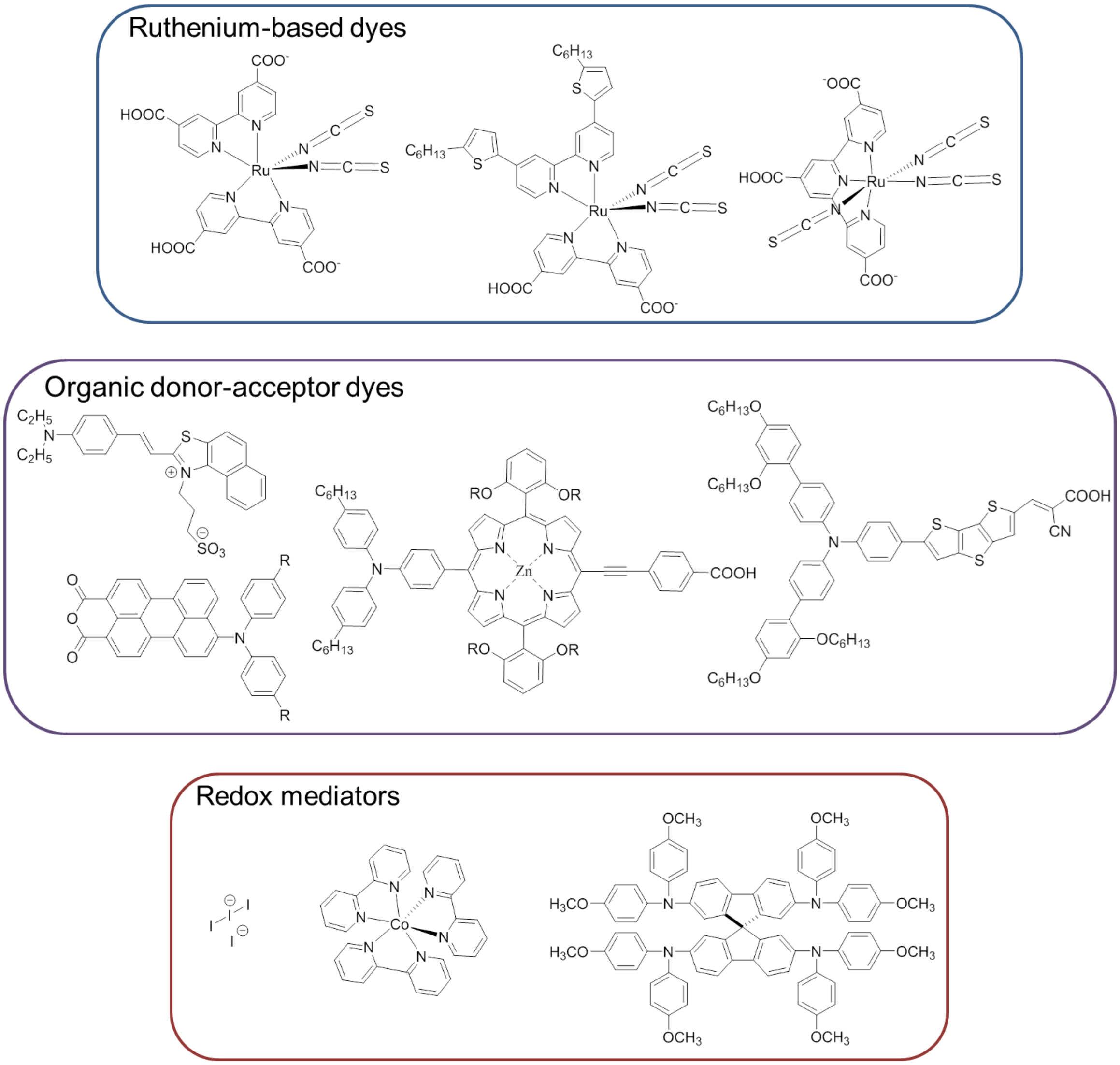

*Figure 4.3: Survey of high-efficiency DSSC dyes and redox mediators*

into the $TiO_2$ conduction band. All three requirements are controlled by the location of the HOMO and LUMO levels of the dye, which determine which wavelengths the dye will absorb, whether the dye will be p-type or not, and whether the excited electron will easily pass from the dye LUMO to the conduction band of $TiO_2$. Additionally, for a robust covalent attachment to the $TiO_2$ surface, the dye must possess a chemical anchor, which usually consists of a carboxylic acid or carboxylate functional group.[231,237]

Both metal-organic complexes and organic dyes rely on charge transfer complexes to realize a desirable absorption profile. The former utilize ligand-to-metal charge transfer (LMCT). LMCT complexes result from the transfer of electrons from the molecular orbitals of one or multiple ligands to the d-orbitals of the metal center.[230] The latter utilize ICT, which generally requires a D-π-bridge-A structure. Quantum dots utilize quantum confinement to achieve visible absorption.[229] Finally, it is important to minimize the interaction between dye molecules; if there is a significant electronic interaction, excited electrons can be quenched by neighboring dye molecules before they can be injected into the $TiO_2$ conduction band.[231] A survey of high-efficiency dyes and redox mediators is included in Figure 4.3.

### 4.1.3 Electrochromic dyes

Electrochromic materials have the ability to change color upon experiencing a redox process. This color change can occur during oxidation or reduction, depending upon the material. There are many compounds that exhibit electrochromic behavior, but to be commercially useful, the compound must have a high contrast ratio between the oxidation states, a high stability to repeated electronic cycling and rapid coloration.[240]

The main classes of electrochromic materials are metal oxide films, conjugated small molecules and polymers, and metal coordination complexes. Given the scope of this treatise, only conjugated organic materials will be discussed here.

Within this umbrella, a number of electrochromic organic dyes have been explored.[241] Generally, their electrochromic behavior arises from the effect of placing or removing a charge from a conjugated system, thereby changing the $E_g$ of the system drastically. Some examples of electrochromic organic dyes are polythiphenes,[242-245]

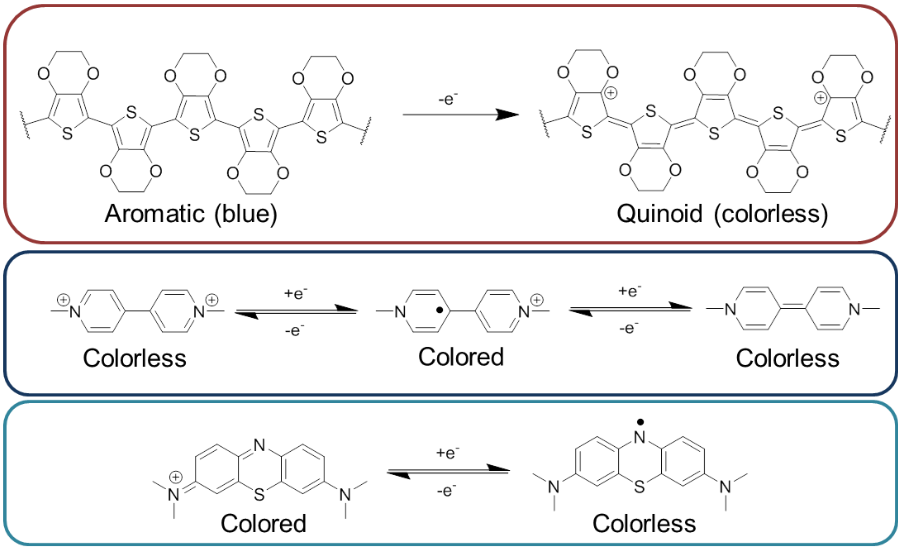

*Figure 4.4: Electrochromism of PEDOT, bipyridinium and Methylene Blue*

phthalocyanines,[246-247] bipyridilium compounds,[248] and Methylene Blue-type dyes[249] (Figure 4.4). For example, polythiophenes are intensely colored in their ground state, however, oxidation introduces a radical cation which forces the adoption of a quinoid structure over an aromatic structure. This quinoid structure greatly diminishes the $E_g$ and the compound absorbance is redshifted. Conversely, the electrochromism of bipyridilium and Methylene Blue-based dyes arises from the generation (or elimination) of a D-A type nature. For example, in its ground state, bipyridilium has two cations and is colorless. Upon reduction to the radical cation, the compound becomes a D-A type dye, with one quaternized nitrogen (acceptor) and one neutral nitrogen (donor); this molecule is intensely colored. Finally, a second reductive process generates a neutral compound, which is, again, colorless. Methylene Blue, on the other hand, has a D-A type ground state, with one positively-charged and one neutral amine on either side of a phenothiazine core. Upon reduction, the ammonium salt is converted to an amine and the dye loses its coloration. However, these dyes are unusual electrochromic materials. Most organic compounds are electrochromic upon oxidation; indeed, given the notorious limited n-type

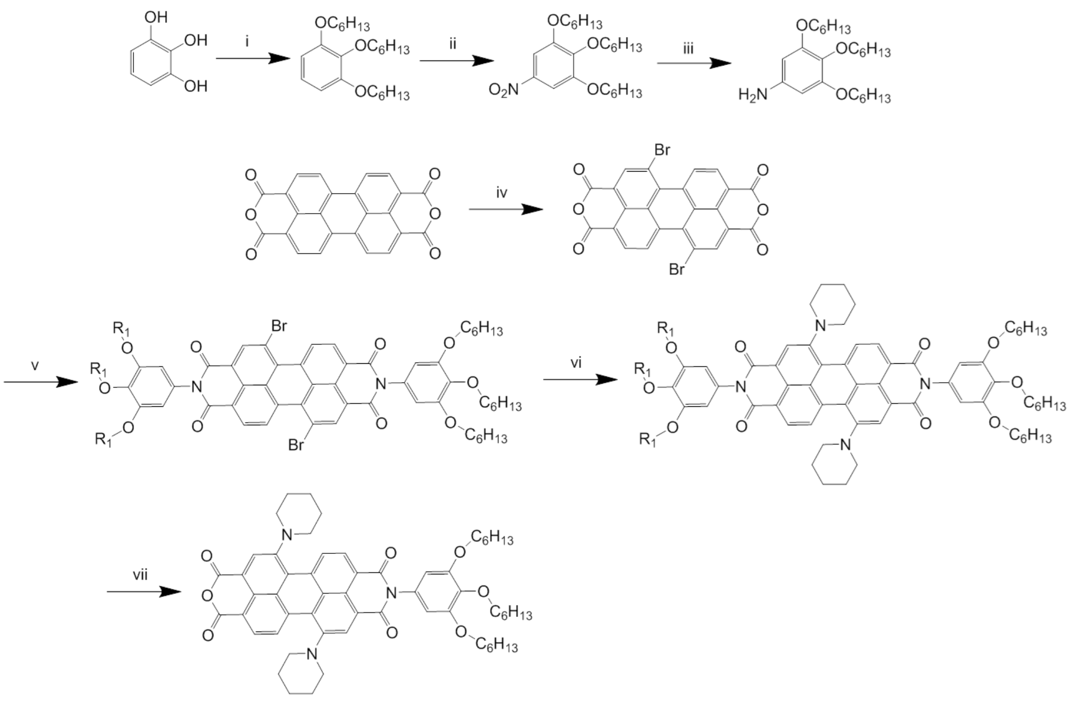

*Scheme 3: Synthesis of PDI dye. i) 1) $K_2CO_3$, DMF, 2) Br-$C_6H_{13}$, 72%; ii) $HNO_3$, $NaNO_2$, $CH_2Cl_2$, 83%; iii) $H_2$, Pd/C, 95%; iv) 1) $H_2SO_4$, $I_2$, 2) $Br_2$, reflux, 24 h, quant.; v) 3,4,5-trihexyoxy-aminobenzene, propionic acid, reflux, 20 h, 86%; vi) piperidine, 24 h, 31%; vii) $^t$BuOH, KOH, 32%*

stability of organic molecules, it is difficult to find compounds that are not only stable to reduction, but also show electrochromic behavior upon reduction. Moreover, requiring the dye to transition from a tinted state to a transparent state upon reduction makes it even more challenging to design.

### 4.2 Design and Synthesis of Perylene Diimide-based Dye

The first compound that was designed was based on a perylene diimide (PDI) core. PDI molecules are known to be exceptionally stable to reduction[250], to exhibit electrochromic behavior[251] and have also been used in DSSCs[252]. First, the PDI molecule was brominated (Scheme 3). Then, to imbue the naturally insoluble PDI with processability, imidization reactions were carried out with a 3,4,5-trihexoxy-

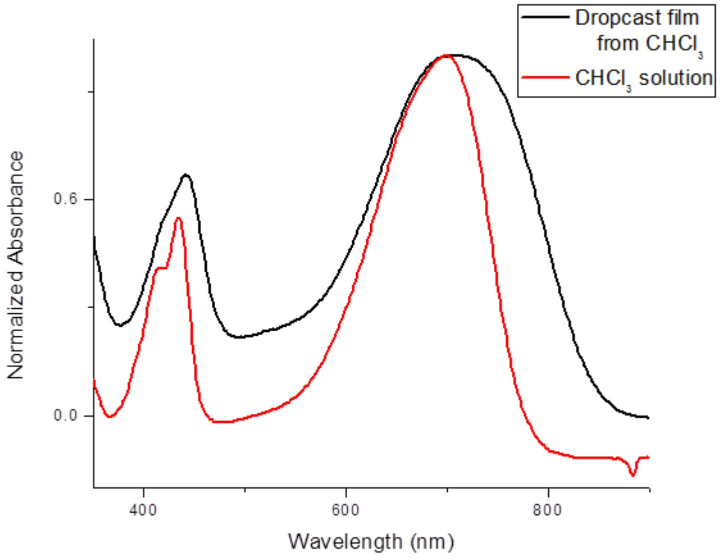

*Figure 4.5: Solution and thin film UV-visible spectra for PDI dye*

aminobenzene. To give the molecule strong visible absorbance, amination reactions using piperidine were carried out at the bay positions; such compounds are known to have exceptional absorptive properties.[252] These piperidine moieties also contribute to the bulkiness of the molecule, thereby limiting aggregation at the $TiO_2$ surface. Finally, to introduce an anchoring point on the molecule, one of the imides was hydrolyzed back to the anhydride. Since the PDI imides have little electronic communication with the PDI core, anhydrides have been shown to provide a good electronic contact between the PDI unit and $TiO_2$, which allows efficient electron injection into the $TiO_2$ conduction band.[252]

Following confirmation of the identity of the product, the solution and thin film absorption were evaluated (Figure 4.5). The dye shows similar absorbance to those reported for structurally-related compounds.[252] The ICT of the thin film absorption has a larger full-width half-max compared to the solution spectra, which is due to inhomogenous broadening.

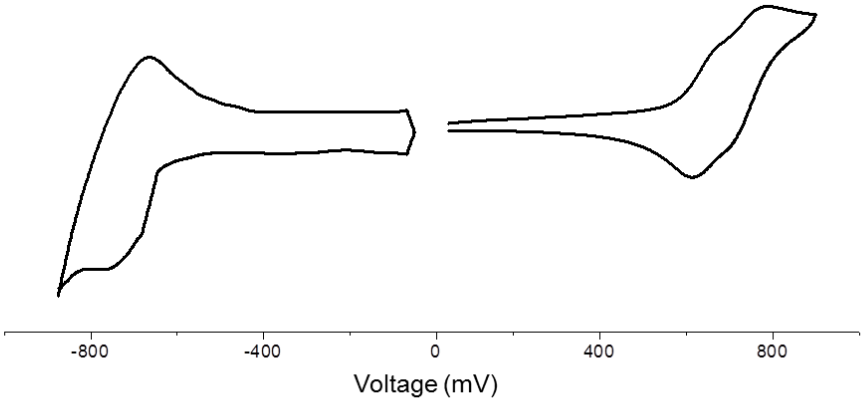

*Figure 4.6: CV scans of PDI dye*

Subsequently, the electronic properties of thin films of the dye were evaluated using CV (Figure 4.6). The dye shows reversible oxidation and reduction peaks, which is a necessary requirement for the dye. The dye possesses oxidation and reduction potentials of 0.6 V and -0.85 V, respectively. Accounting for the redox potential of ferrocene, these

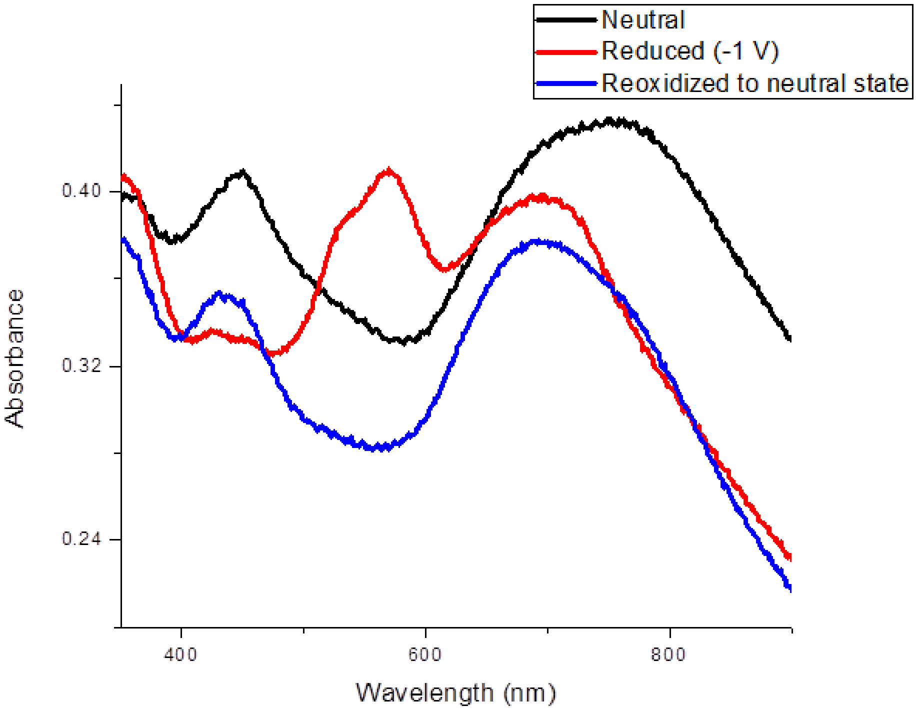

*Figure 4.7: Spectroelectrochemical spectra of PDI dye*

correspond to a HOMO and LUMO of -5.2 eV and -3.6 eV, respectively, and an overall $E_g$ of 1.4 eV. This is in agreement with the thin film absorption onset energy.

Finally, spectroelectrochemistry was executed on thin films of the dye to quantify the absorbance following reduction (Figure 4.7). Unfortunately, the absorbance changes little upon reduction. Qualitatively, the dye changes from a deep green color to a blue-green color. This makes it unsuitable for the project goals.

### 4.3 Design and Synthesis of a Methylene Blue-based Dye

Following the PDI dye, it was considered prudent to design the dye from a molecule that is known to have electrochromic properties upon reduction. To this end, a structure based on Methylene Blue was decided upon. Not only does this dye show electrochromic behavior upon reduction, it also has a desirable absorbance spectrum with a $\lambda_{max}$ around 675 nm.[253]

The traditional way to synthesize Methylene Blue-type molecules is to oxidize phenothiazine with iodine. From there, a nucleophilic substitution reaction with a secondary amine serves to aminate the positions *meta* to the sulfur atom. Methylene Blue has dimethylamine substituents; to make the dye suitable for the DSSC architecture, carboxylic acids needed to be introduced as $TiO_2$ anchors. To this end, 4,4'-iminobis-benzoic acid was used for the amination reaction.

The synthesis (Scheme 4) began with the oxidation of phenothiazine in good yield. Concurrently, a diarylamine was synthesized. Starting from 4-aminobenzoic acid, the acid was protected as a methyl ester. Subsequently, the amine was coupled to 4-chlorobenzoic acid under Buchwald-Hartwig amination conditions. From here, the amination of the oxidized phenothiazine occurred reasonably well. Unfortunately, the

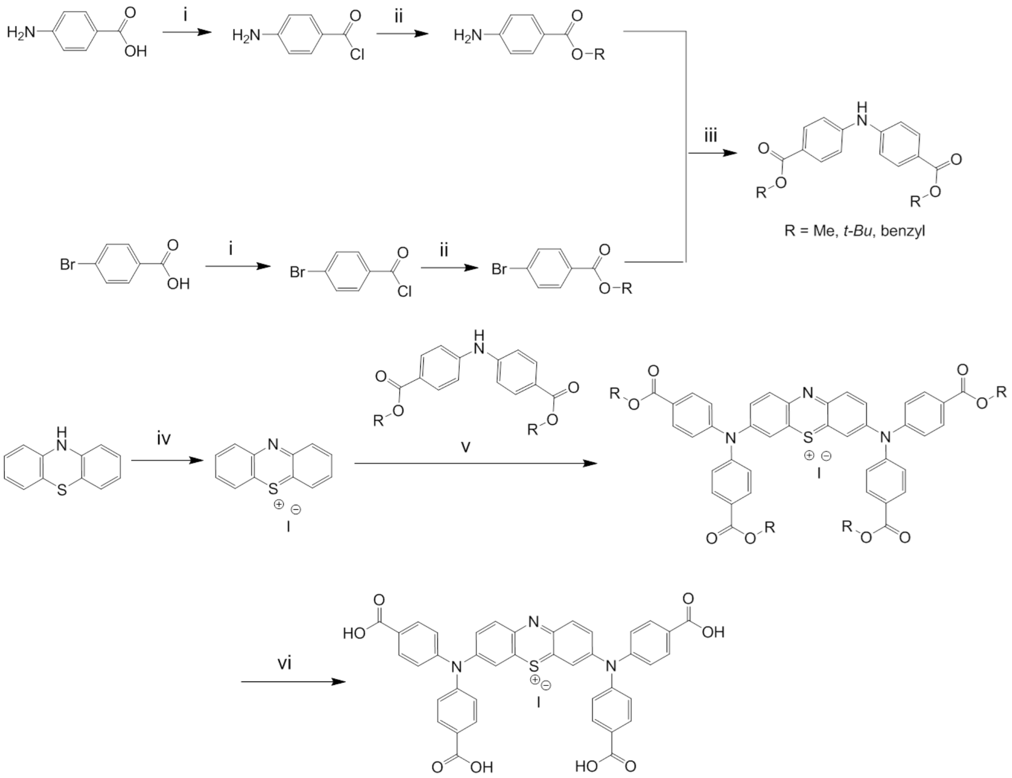

*Scheme 4: Synthesis of Methylene Blue-based dye. i) $SOCl_2$, DCM, 60 °C, 12 h; ii) methanol, t-Butanol, or benzyl alcohol, r.t., 12 h, 74-87%; iii) $Pd_2(dba)_3$, BINAP, $K_3PO_4$, DME, reflux, 24 h, 55-69%; iv) $I_2$, DCM, r.t., 3 h, quant.; v) MeOH, r.t., 8 h, 10-15%; vi) $H_2$, Pd/C, 20 h, 95% (unable to protect methyl and t-butyl esters)*

deprotection of the methyl ester proved to be difficult. A number of conditions were attempted ($HCl/H_2O$, $NaOH/H_2O/MeOH$, $H_2SO_4/H_2O$, $NaBH_4/I_2/CHCl_3$) but none yielded the deprotected tetra-acid. To address this deprotection issue, two new diarylamines were synthesized with *tert*-butyl and benzyl ester protecting groups. The former was chosen because it is more labile than methyl esters, the latter was attractive due to its deprotection via hydrogenation. Ultimately, the *tert*-butyl ester suffered the same problems as the methyl ester. However, the benzyl ester was removed in nearly quantitative yield under standard hydrogenation conditions ($H_2$/palladium on carbon).

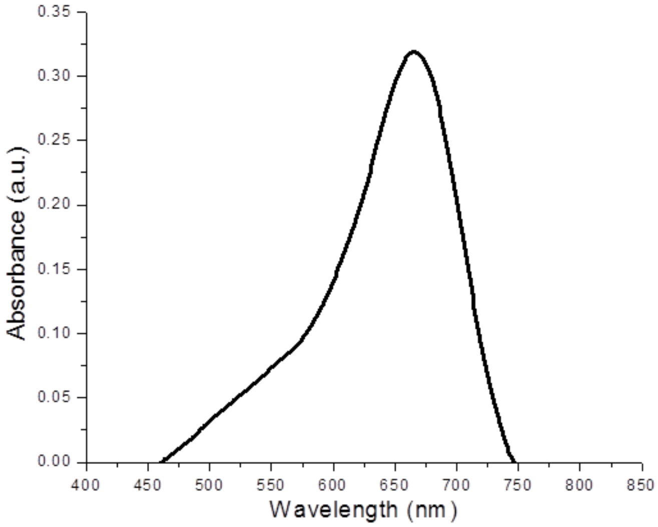

*Figure 4.8: UV-visible spectra of Methylene Blue-based dye*

The final compound was characterized by UV-visible spectroscopy (Figure 4.8). The compound possessed a strong ICT band with a $\lambda_{max}$ ca. 650 nm, which is in good agreement with the literature. Sadly, CV measurements (not shown) on the compound showed no visual electrochromic behavior.

### 4.4 Design and Synthesis of Phthalocyanine Dyes

Following this failure, a new class of dyes were designed and synthesized. These consisted of phthalocyanine cores, which are known to have electrochromic properties.[247-248] By itself, unadorned phthalocyanine is a p-type material with little processability due to its poor solubility in all solvents.[254] Thus, to lower the HOMO and LUMO levels of phthalocyanine in order to make it stable to reduction, two methods were used. Each centered on fusing an electron-withdrawing ring to the phthalocyanine arms. The first target was designed with electron-deficient pyrazine rings fused to the peripheral benzene rings on the phthalocyanine; the second target possessed succinimide rings fused to the same peripheral benzene rings, similar to common n-type materials like naphthalene and perylene diimides. Finally, there are many metal ions that can be used to coordinate with the phthalocyanine skeleton. The electronic properties of phthalocyanines vary widely based on the coordinating metal atom.[255] That being said, zinc was chosen as the metal center for both derivatives because zinc phthalocyanines have often been cited for their electrochromic behavior. Additionally, zinc and copper phthalocyanines are often used in organic electronic devices due to their desirable electronic properties.[256-259]

### 4.4.1 Synthesis and Characterization of Pyrazine-Phthalocyanine Dye

The synthesis of the pyrazine-phthalocyanine was relatively straightforward. Two dyes were made – with and without carboxylic acid anchors (Scheme 5). The synthesis of both materials used similar intermediates. First, *ortho*-phenylenediamine was protected with tosyl groups and then brominated at the 4 and 5 positions. Deprotection yielded the free bases, which oxidized quickly even when stored under nitrogen. This was condensed with benzil to yield the diphenyl quinoxaline. To synthesize the carboxylic acid derivative, 4-formylbenzoic acid was protected as a methyl ester. Then, a potassium cyanide-mediated homocoupling yielded the alpha-hydroxyketone, which was oxidized to the diketone. This diketone intermediate was doubly condensed with the diamine to furnish the quinoxaline compound. Following the synthesis of these two quinoxaline intermediates, the bromines were substituted with cyano groups to generate the final intermediate. These compounds were converted to the analogous zinc phthalocyanines using zinc acetate, 1,8-diazabicyclo[5.4.0]undec-7-ene and 1-pentanol as the solvent.

Generally, the absorbance spectrum (Figure 4.9) of the dye has two bands that are characteristic of phthalocyanines: a Soret band at high energy (~375 nm) and a Q band at

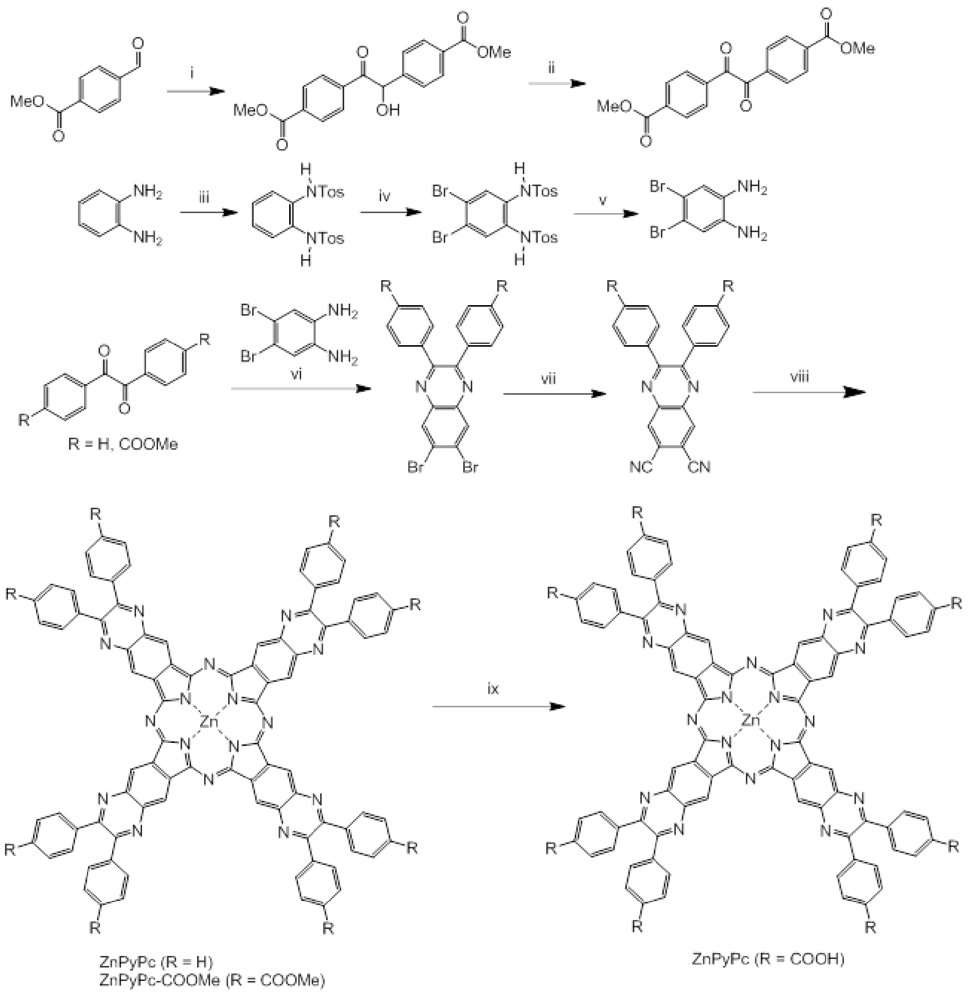

*Scheme 5: Synthesis of pyrazine-phthalocyanine dyes. i) KCN, EtOH, $H_2O$, reflux, 20 h, 63%; ii) HBr, DMSO, r.t., 16 h, 78%; iii) TosCl, pyridine, 0 °C to r.t., overnight, 87%; iv) $Br_2$, AcOH, $CHCl_3$, 100 °C, 16 h, 75%; v) $H_2SO_4$, 120 °C, 24 h, 82%; vi) AcOH, reflux, 20 h, 73% (R=H), 65% (R=COOMe); vii) CuCN, DMF, 100 °C, 41% (R=H), 22% (R=COOMe); viii) $Zn(Ac)_2$, DBU, pentanol, 120 °C, 24 h, 14% (R=H), 15% (R=COOMe); ix) NaOH, MeOH/$H_2O$, r.t., overnight, 84%*

lower energy (~760 nm). Both of these absorption processes result from a π-π* transition.[260] What is unusual about these phthalocyanines is that their Soret band is significantly more intense than the Q band; typically, phthalocyanines have intense Q

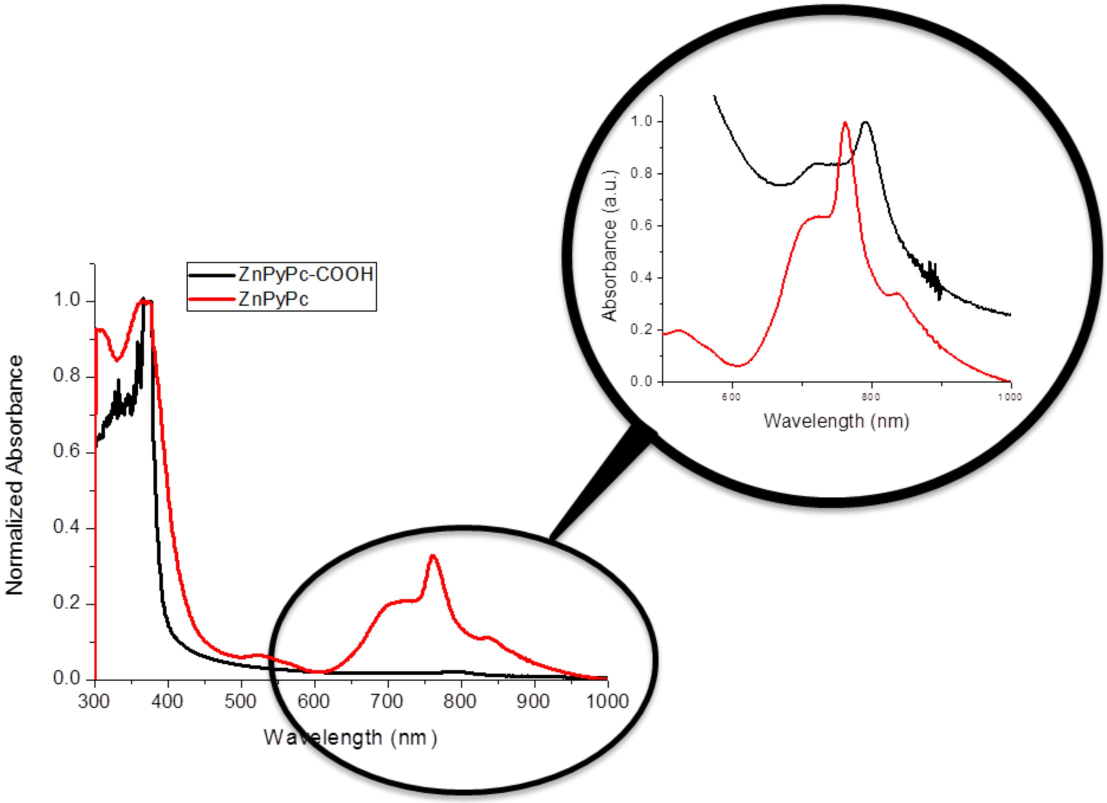

*Figure 4.9: UV-visible spectrum of ZnPyPc and ZnPyPc-COOH dyes. Inset: absorption normalized to ICT peak*

band absorption compared to the Soret band. Interestingly, the carboxylic acid derivative has a barely perceptible Q band. However, when the spectra are normalized to the Q band absorbance maximum, it is clear that they have nearly identical absorption processes for the Q band peak. It is possible that the excited state orbitals for the Q band are localized on the pyrazine moieities and have little overlap with the HOMO orbitals, which tend to be localized in the core of the molecule. This limited spatial overlap between ground state and excited state molecular orbitals could contribute to a weak Q band absorption.[261] With the attachment of the carboxylic acids, the excited state orbitals of the Q band presumably shift even further outward, leading to less overlap. This would explain the decrease in Q band intensity upon attaching the carboxylic acids.

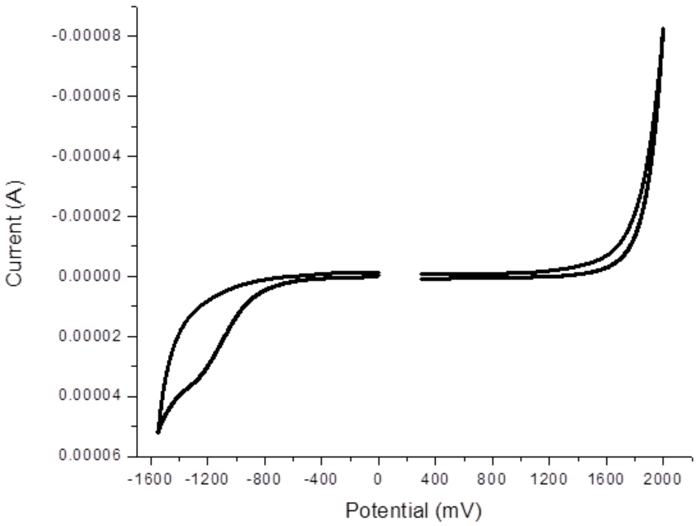

*Figure 4.10: CV scan of ZnPyPc-COOH*

The electronic characteristics of the carboxylic acid derivative were also determined using CV (Figure 4.10). The dye has completely irreversible oxidation and reduction processes, with onsets of 1.75 V and -0.84 V, respectively. These correspond to HOMO and LUMO levels of -6.2 eV and -3.7 eV. Obviously, given the large $E_g$ (2.5 eV) determined by CV, the major electronic process is reflected by the Soret band; the Q band absorption process contributes little to the electronic behavior of the dye. This is in agreement with the extremely low intensity of the Q band.

Regardless of the irreversibility of the redox processes and the limited near-IR absorption, the fact that the molecule has near-UV and near-IR absorption bands makes it nearly transparent to visible light. Moreover, the HOMO and LUMO energy levels accounting for the UV-absorption process suggested that the dye should be capable of efficient electron injection into the $TiO_2$ conduction band. Thus, it was hypothesized that

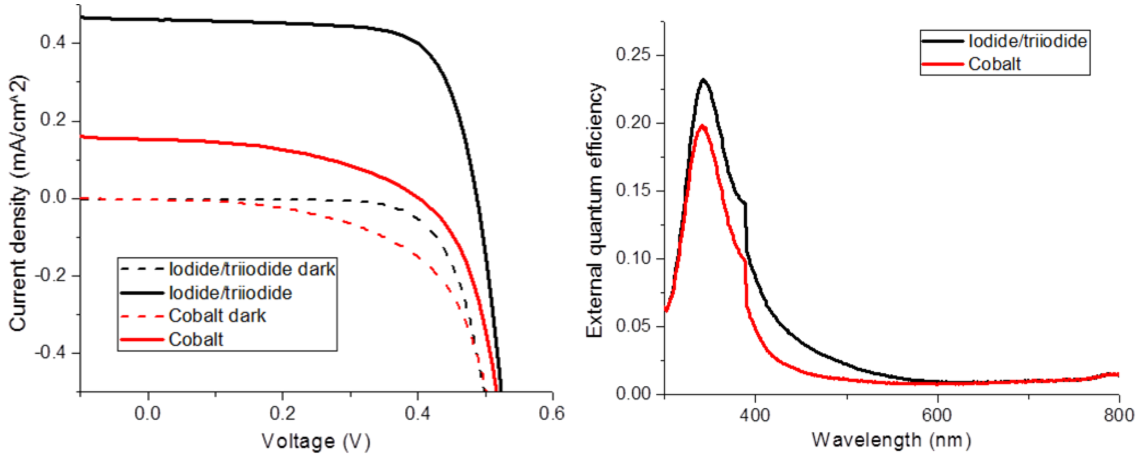

*Figure 4.11: J-V curve (left) and EQE plot (right) for DSSCs made using ZnPyPc-COOH with iodide/triiodide and cobalt redox mediators*

the dye could be used in conjunction with a separate electrochromic layer, thereby simplifying the requirements for the dye.

To test this hypothesis, the dye was first incorporated into a DSSC to investigate its inherent performance. Two classes of DSSCs were fabricated using iodide/triiodide and cobalt redox mediators. Both cells show poor performance (Figure 4.11), although the iodide/triiodide mediator exhibited much better performance. Although the $V_{oc}$ and FF were reasonable for both redox mediators, the $J_{sc}$ was extremely low in both cases and limited the overall PCE of the DSSCs. There are several possible reasons for this. The most likely is that the major absorption process in the dye occurs at very high energy; few incident photons have energies larger than 2.5 eV.[262] As can be seen in the IPCE plot, all of the photocurrent occurs from photons with wavelengths less than 400 nm. This poor overlap between the solar output and the absorption profile of the dye is one major reason why the dye produces poor $J_{sc}$ values. Another possible explanation for the low PCE values is that recombination rates are high at the $TiO_2$ surface. Phthalocyanines are extremely planar molecules and tend to pack very efficiently. Although the pendant

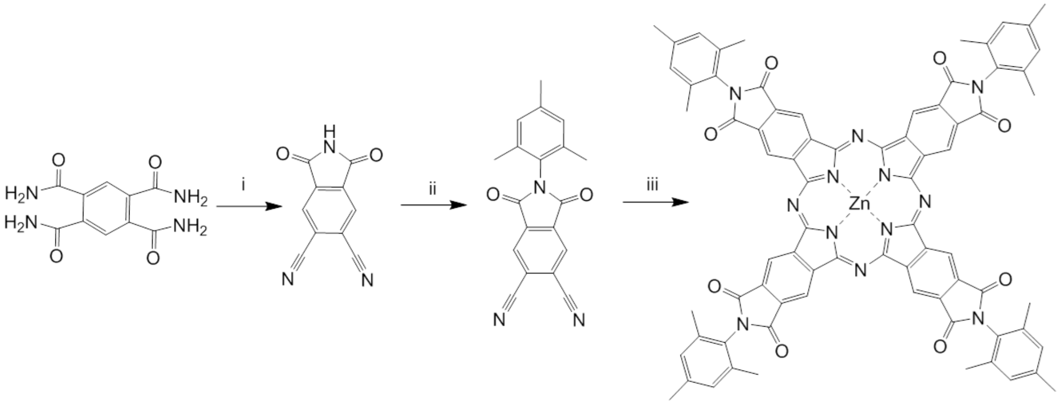

*Scheme 6: Synthesis of S-Pc. i) $SOCl_2$, DMF, 65 °C, 7 h, 31%; ii) mesitylene, $PhI(OAc)_2$, 34%, iii) $Zn(Ac)_2$, DBU, pentanol, 120 °C, 24 h, 43%*

phenyl rings sit nearly perpendicular to the plane of the phthalocyanine core, this does not preclude packing at the $TiO_2$ surface. However, neither of these explanations suffice to elucidate why the $J_{sc}$ is higher when using the iodide/triiodide redox mediator. It could be that the colored iodide/triiodide absorbs light and contributes to the photocurrent as a sensitizer itself or that it is less bulky than the cobalt mediator and is able to diffuse more quickly and penetrate deeper into the $TiO_2$ matrix. Regardless, given the poor PCE values, further research on this dye was halted.

### 4.4.2 Synthesis and Characterization of Succinimide-Phthalocyanine Dye

Synthesis of the succinimide-phthalocyanine dye (ZnSPc) began with 1,2,4,5-benzenetetracarboxamide (Scheme 6). Treatment with thionyl chloride in DMF at elevated temperature yielded a mixture of diimide, dicyanoimide and tetracyanobenzene; the dicyanoimide was purified by silica gel chromatography in modest yield. Given the lack of electrochromism in the previous dyes, as well as the synthetic difficulty of introducing a carboxylic acid onto the imide, it was decided that a proof-of-concept synthesis was in order to probe the electronic and electrochromic properties of the

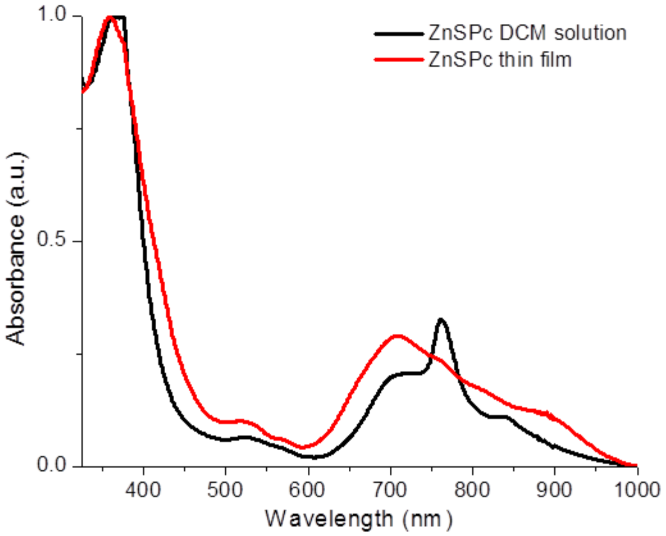

*Figure 4.12: Solution and thin film UV-visible spectra of ZnSPc*

material before determining whether the extra synthetic difficulty of introducing a carboxylic acid was worthwhile. To this end, treatment of this intermediate with mesitylene under oxidative conditions furnished the mesitylene-imide. Finally, identical phthalocyanine formation conditions generated the final zinc phthalocyanine.

Again, the absorbance spectrum of the dye (Figure 4.12) exhibits a Soret band at <300 nm and a Q band at ~700 nm. Additionally, the Q band has a lower intensity than the Soret band, which is very similar to the pyrazine phthalocyanine. This lends credence to the idea that, upon attaching strong electron-withdrawing groups to the phthalocyanine core, the excited state orbitals for the Q band are shifted to the periphery of the molecule and have little overlap with the HOMO orbitals, producing a weak low energy transition. Again, the electronic characteristics of the dye were investigated using CV (Figure 4.13). Interestingly, despite the prediction that the dye would have reversible n-type properties, the reduction curve is entirely irreversible, while the oxidation curve shows quasi-

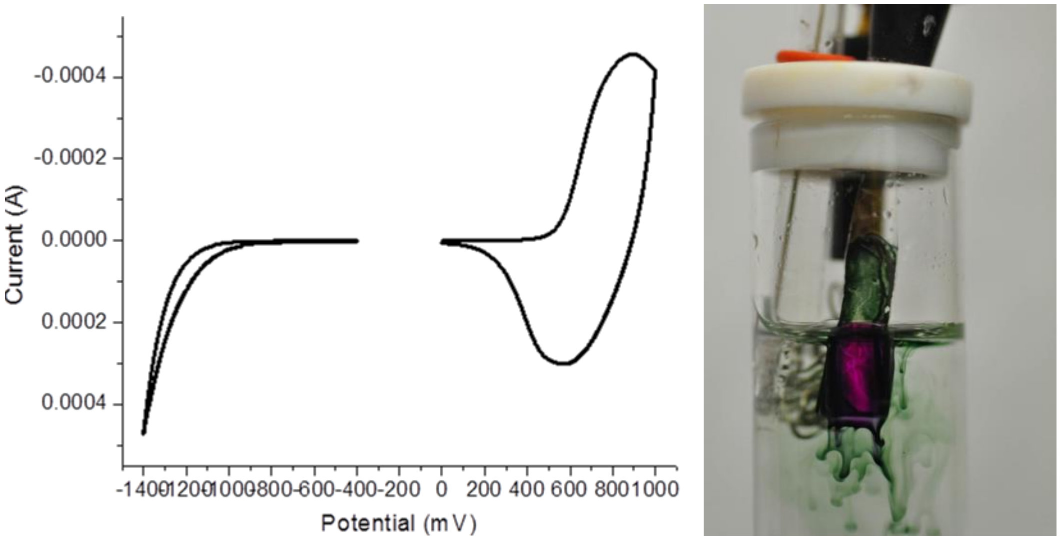

*Figure 4.13: CV scan of ZnSPc (left) and image of ZnSPc electrochromism in CV cell upon reduction (right)*

reversible behavior. The onsets of the oxidation and reduction processes are 0.62 V and -0.75 V, respectively, which correspond to HOMO and LUMO levels of -5.2 eV and -3.8 eV. Hence, it seems that the Q band absorbance is significant enough to dictate the $E_g$ of the molecule.

However, the most interesting feature of this dye is that it exhibits electrochromism upon reduction at a potential of -1 V (Figure 4.13). Unfortunately, the dye transitions from a deep green in its ground state to a bright magenta in its reduced state, making it largely impractical for use in an electrochromic window. Moreover, the dye is only partially stable to repeated reduction scans; it eventually degrades to a brown compound that does not possess electrochromic behavior. Regardless, taking the electrochromism by itself, this is an achievement, as there are few organic dyes that exhibit electrochromism upon reduction.

### 4.5 Conclusions

Four dyes were designed and synthesized to fulfill two general functions in the DSSC architecture: to serve as light-harvesting sensitizers for energy-harvesting and to exhibit tinted to transparent electrochromic behavior upon reduction for the DSSC to double as an electrochromic window. The first class of dye was based upon a perylene diimide core. The final dye possessed piperidine moieties at the bay positions to tune its absorbance and a trihexoxybenzene imide to imbue it with solution processability, as well as to hinder packing at the $TiO_2$ surface. Although the dye had desirable light-harvesting characteristics and energy levels for DSSC function, its electrochromic behavior was very limited. The second class of dye was a derivative of Methylene Blue, a well-known cationic organic dye, which has also been shown to possess electrochromic behavior. In lieu of the dimethylamine groups on the Methylene Blue dye, this derivative sported diarylamine units functionalized with carboxylic acids. Again, although the energy levels and absorbance spectrum of the dye were favorable, thin films of the material showed no electrochromic properties. Finally, the third and fourth dyes were based upon phthalocyanine cores, which were modified with electron-deficient units to lower the HOMO and LUMO levels, thereby increasing the stability of the dyes to reduction. The first of the two possessed fused diphenyl pyrazine rings on the phthalocyanine arms, modified with carboxylic acids. This yielded a dye with an intense Soret band ca. 375 nm and weak Q band ca. 760 nm, which is contrary to the relative intensity of these two transitions in typical phthalocyanine molecules. It is not certain why this is the case. It could be due to HOMO and LUMO localization at the core and periphery of the molecule, respectively; this weak ground/excited state orbital overlap would lead to a weak absorption. Given the transparency of the dye, it was hoped that it could be used in a DSSC with a separate electrochromic layer. Unfortunately, preliminary devices showed very poor efficiencies. This is either due to poor spectral overlap, high recombination rates or some combination thereof. The second of the phthalocyanine dyes utilized electron-withdrawing succinimide groups fused to the phthalocyanine arms. Like the first phthalocyanine dye, the absorbance spectrum of this dye also exhibited a very weak Q band compared to the Soret band. The consistency of the relative Q/Soret band intensities for these two dyes suggests that poor HOMO/LUMO overlap is likely the explanation for the weak Q band transition and is caused by fusing electron-deficient moieties to the phthalocyanine core, which shifts the LUMO to the periphery of the molecule. Interestingly, this dye shows impressive electrochromism upon reduction, changing from a green-tinted ground state to a magenta colored reduced state. Despite the success at engineering a dye that is electrochromic upon reduction, the magenta coloration is not ideal for the application.

## 4.6 Experimental

**Materials:** Unless otherwise specified, all chemicals were purchased from Aldrich or TCI and used without further purification. 3,4,5-trihexoxy-aminobenzene[263], 1,7-dibromo-3,4,9,10-perylenetetracarboxylic dianhydride[264], 4-aminobenzoates[265], 4-bromobenzoates[266-267], tetraiodophenothiazinium[268], 4,4’-oxalyldi-benzoic acid dimethyl ester[269], 4,5-dibromo-1,2-benzenediamine[270], 6,7-dibromo-2,3-diphenylquinoxaline[271], and 4,5-dicyanophthalimide[272] were prepared according to the literature.

**Synthesis of 1,7-dibromo-3,4,9,10-perylenebisimide**: Dibromo-3,4,9,10-perylenetetracarboxylic dianhydride (2.1 g, 3.8 mmol, 1 eq) was suspended in propionic acid (50 mL) and 3,4,5-trihexoxy-aminobenzene (4.5 g, 11.5 mmol, 3 eq) was added. The mixture was heated to 140 °C and allowed to stir for 24 h. After cooling to room temperature, the solution was poured onto ice and filtered. This crude material was used for the next step without further purification. $^1$H NMR (300 MHz, $CDCl_3$, $\delta$): 8.45 (s, 2H), 8.27 (d, 2H), 7.44 (d, 2H), 6.81 (s, 4H), 2.35 (t, 12H), 1.78 (m, 24H), 1.10-0.80 (m, 42H)

**Synthesis of 1,7-dipieridinyl-3,4,9,10-perylenebisimide**: The bisimde (2 g) was added to piperidine (50 mL) and stirred for 24 h. The solution was dissolved in DCM, washed repeatedly with 1 M HCl to remove the piperidine. The organic fraction was dried with $Na_2SO_4$, evaporated to dryness and purified via silica gel chromatography (100% DCM) to yield a dark crystal (0.5 g, 31%). $^1$H NMR (300 MHz, $CDCl_3$, $\delta$): 8.31 (s, 2H), 8.07 (d, 2H), 7.31 (d, 2H), 6.79 (s, 4H), 2.37 (t, 12H), 1.72 (m, 24H), 1.10-0.80 (m, 42H)

**Synthesis of 1,7-dipiperidinylperylene-3,4:9,10-tetracarboxylic acid-3,4-anhydride-9,10-imide**: 1,7-dibromo-3,4,9,10-perylenebisimide (0.25 g) was added to a solution of KOH (1 g) in *tert*-butanol (10 mL) and heated to 100 °C for 2 h. The mixture was cooled to room temperature, poured into water and extracted with chloroform. The combined organic extracts were dried with $Na_2SO_4$, evaporated to dryness and purified via silica gel chromatography (DCM:MeOH 10:1) to yield a dark crystal (0.066 g, 37%). $^1$H NMR (300 MHz, $CDCl_3$, $\delta$): 8.41 (s, 1H), 8.37 (s, 1H), 8.10 (d, 1H), 8.01 (d, 1H), 7.31 (d, 1H), 7.25 (d, 1H), 6.76 (s, 2H), 2.36 (t, 6H), 1.73 (m, 12H), 1.10-0.80 (m, 24H).

**General synthesis of 4,4'-imino-bisester benzoic acids:** An oven-dried flask was charged with BINAP (10 mol%), $Pd_2(dba)_3$ (5 mol%), and NaOt-Bu (135 mg, 1.4 mmol). The flask was evacuated and backfilled with argon after which toluene (5 mL), the aryl bromide (1.0 mmol), and the diarylamine (1.2 mmol) were added. The mixture was allowed to stir at 100 °C overnight. Then, the mixture was diluted with ether (20 mL), filtered through Celite, and concentrated in vacuo. The crude material was purified by flash chromatography on silica gel.

4,4'-imino-bis(1,1'-dimethyl)ester benzoic acid: White solid. Yield: 55%. $^1H$ NMR (300 MHz, $CDCl_3$, $\delta$): 7.99 (d, 4H), 7.15 (d, 4H), 3.89 (s, 6H)

4,4'-iminobis-bis(1,1'-dimethylethyl)ester benzoic acid: White solid. Yield: 57%. $^1H$ NMR (300 MHz, $CDCl_3$, $\delta$): 7.81 (d, 4H), 7.21 (d, 4H), 1.26 (s, 18H)

4,4'-iminobis-bis(benzyl)ester benzoic acid: White solid. Yield: 69%. $^1H$ NMR (300 MHz, $CDCl_3$, $\delta$): 7.88 (d, 4H), 7.50-7.25 (m, 10H), 6.62 (d, 4H), 4.71 (s, 4H)

**General procedure for the synthesis of 3,7-bis(dibenzoateamino)phenothiazinium iodide:** Phenothiazinium tetraiodide (2.0 mmol, 1 eq) was added portionwise to a solution of the proper diphenylamine (6.0 mmol, 3 eq) in methanol (50 mL) over 30 min. The solution was stirred at room temperature for 8 h. The mixture was concentrated and precipitated by the addition of ether. The crude product was collected by filtration and purified by column chromatography (DCM:MeOH 10:1) to yield a dark blue crystal.

Dimethyl derivative: 12%. $^1H$ NMR (300 MHz, MeOH, $\delta$): 7.91 (d, 2H), 7.31 (d, 2H), 7.25-6.95 (m, 18H), 3.41 (s, 12H)

Di-*tert*-butyl derivative: 10%. $^1H$ NMR (300 MHz, MeOH, $\delta$): 7.93 (d, 2H), 7.30-6.95 (m, 20H), 3.45 (s, 36H)

Dibenzyl derivative: 15%. $^1$H NMR (300 MHz, MeOH, $\delta$): 7.91 (d, 2H), 7.30-6.95 (m, 40H), 4.12 (s, 8H)

**Synthesis of 3,7-bis(dibenzoic acidamino)phenothiazinium iodide:** The phenothiazinium precursor (50 mmol) was added to Pd/C (10 wt%) in EtOAc:EtOH (1:1, 200 mL) and shaken under 3 atm $H_2$ gas for 20 h. The solution was filtered through Celite and concentrated to yield a dark blue solid. 95%. $^1$H NMR (300 MHz, MeOH, $\delta$): 7.91 (d, 2H), 7.30-7.05 (m, 40H).

**Synthesis of 6,7-dicyano-2,3-di(phenyl)quinoxaline:** 6,7-dibromo-2,3-di(phenyl)quinoxaline (2.5 mmol, 1 eq) was dissolved in DMF (25 mL) and CuCN (10 mmol, 4 eq) was added. The solution was heated to 100 °C overnight. After cooling to room temperature, the mixture was poured into water, filtered and purified by column chromatography ($CHCl_3$:Hex 1:3) to yield a pale yellow solid (41%). $^1$H NMR (300 MHz, MeOH, $\delta$): 8.67 (s, 2H), 7.41 (d, 4H), 7.37 (d, 4H), 7.31 (t, 2H).

**Synthesis of ZnPyPc:** 6,7-dicyano-2,3-di(phenyl)quinoxaline (1 mmol), DBU (10 mol%) and $Zn(OAc)_2$ (0.5 mmol) were added to a flask, followed by 1-pentanol (3 mL). The mixture was heated to 120 °C overnight. It was then cooled to room temperature, poured into methanol and filtered. The solid was recrystallized in EtOH. Brown cystals. Yield: 15%. $^1$H NMR (300 MHz, $CHCl_3$, $\delta$): 8.98 (s, 8H), 7.50-7.30 (m, 40H).

**Synthesis of 6,7-dibromo-2,3-di(methylbenzoate)quinoxaline:** 4,4’-oxalyldi-benzoic acid dimethyl ester (5 mmol) and 4,5-dibromo-1,2-benzenediamine (5 mmol) were dissolved in acetic acid. The solution was heated to 100 °C overnight. After cooling to room temperature, the mixture was poured into water, filtered and purified by column chromatography ($CHCl_3$:Hex 2:3) to yield a pale yellow solid (65%). $^1$H NMR (300 MHz, MeOH, $\delta$): 8.54 (s, 2H), 8.06 (d, 4H), 7.60 (d, 4H), 3.96 (s, 6H).

**Synthesis of 6,7-dicyano-2,3-di(methylbenzoate)quinoxaline:** 6,7-dibromo-2,3-di(methylbenzoate)quinoxaline (2 mmol, 1 eq) was dissolved in DMF (20 mL) and CuCN (8 mmol, 4 eq) was added. The solution was heated to reflux overnight. After cooling to room temperature, the mixture was poured into water, filtered and purified by column chromatography ($CHCl_3$:Hex 1:1) to yield a pale yellow solid (22%). $^1$H NMR (300 MHz, MeOH, $\delta$): 8.69 (s, 2H), 8.10 (d, 4H), 7.66 (d, 4H), 3.97 (s, 6H).

**Synthesis of ZnPyPc-COOMe:** 6,7-dicyano-2,3-di(methylbenzoate)quinoxaline (1 mmol), DBU (10 mol%) and $Zn(OAc)_2$ (0.5 mmol) were added to a flask, followed by 1-pentanol (3 mL). The mixture was heated to 120 °C overnight. It was then cooled to room temperature, poured into methanol and filtered. The solid was recrystallized in EtOH. Light brown cystals. Yield: 15%. $^1$H NMR (300 MHz, $CHCl_3$, $\delta$): 9.02 (s, 8H), 7.75-7.35 (m, 32H).

**Synthesis of ZnPyPc-COOH:** ZnPyPc-COOMe (0.1 mmol) was added to a flask containing KOH (5 mmol) in MeOH/$H_2O$ (5:1). The mixture was stirred at room temperature overnight. The solution was acidified to ~pH 3 using 5 M HCl. The precipitated solid was filtered and recrystallized in MeOH. Light brown/yellow cystals. Yield: 84%. $^1$H NMR (300 MHz, $CHCl_3$, $\delta$): 9.05 (s, 8H), 7.90-7.50 (m, 32H).

**Synthesis of *N*-2,4,6-trimethylbenzene-4,5-dicyanophthalimide:** 4,5-dicyanophthalimide (5 mmol), mesitylene (5 mL) and $PhI(OAc)_2$ (25 mmol) were added to a flask. The mixture was heated to 140 °C for 6 h. After cooling to room temperature, the solution was filtered through a plug of silica and washed with

$CHCl_3$. The filtrate was concentrated and purified by silica gel chromatography (100 $CHCl_3$). Off white solid. Yield: 34%. $^1$H NMR (300 MHz, $CHCl_3$, $\delta$): 8.33 (s, 2H), 7.02 (s, 2H), 2.34 (s, 9H).

**Synthesis of ZnSPc:** *N*-2,4,6methylbenzene-4,5-dicyanophthalimide (1 mmol), DBU (10 mol%) and $Zn(OAc)_2$ (0.5 mmol) were added to a flask, followed by 1-pentanol (3 mL). The mixture was heated to 120 °C overnight. It was then cooled to room temperature, poured into methanol and filtered. The solid was recrystallized in EtOH. Dark green crystals. Yield: 43%. $^1$H NMR (300 MHz, $CHCl_3$, $\delta$): 8.91 (s, 8H), 8.53 (s, 8H), 3.02 (s, 36H).

# 5. Utilizing Ambipolar Hyperbranched Polymers for the Electrodes of Symmetric Supercapacitors

## 5.1 Introduction

One of the major obstacles to implementing solar energy is finding a way to efficiently store that electricity until there is a need for it. A large demand on electricity occurs when the sun is not shining, which necessitates an ability to easily store and retrieve the energy. The most common ways to do this are to use batteries.[273] There are two broad categories of batteries: primary, which cannot be recharged, and secondary, which can be. Given the need for repeated charge/discharge cycles, primary batteries will not be discussed further. There are many kinds of secondary batteries. Two of the most common are lead-acid batteries and lithium-ion batteries. However, despite their widespread use, batteries are not always the best way to store energy. Many research groups are investigating novel ways to store electricity. Supercapacitors are one such alternative to batteries.

### 5.1.1 Lead-acid Batteries

Lead-acid batteries are the oldest type of secondary battery (Figure 5.1). They consist of lead (Pb) and lead oxide ($PbO_2$) electrodes immersed in an aqueous solution of $H_2SO_4$. Upon discharging, the Pb and $PbO_2$ electrodes are oxidized and reduced, respectively, by $H_2SO_4$ to become lead sulfate ($PbSO_4$). Upon charging, electrons are removed from the $PbSO_4$ at the positive electrode to form $PbO_2$ and are used to reduce the $PbSO_4$ at the negative electrode to Pb.[274]

These batteries are desirable due to their high power-to-weight ratio and inexpensive production. Despite their ubiquity, these batteries suffer from drawbacks.

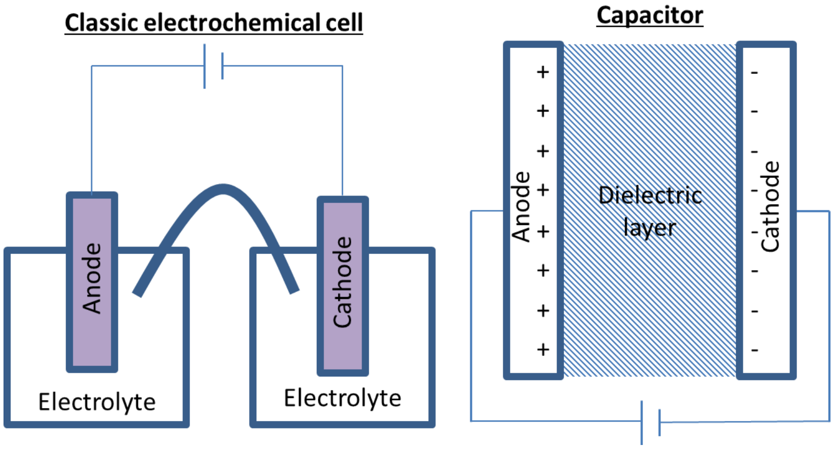

*Figure 5.1: Diagram of electrochemical battery (left) and capacitor (right)*

Over time, repeated charge-discharge cycles cause mechanical stresses at the electrodes, leading to disintegration, thereby lessening charge capacity. Additionally, if the battery is not fully charged after being discharged, sulfate deposits expand and crack the electrode plates.[275] Finally, given the toxicity of lead, the disposal of these batteries is a large environmental concern. Although they can be recycled, a significant proportion eventually reaches landfills.

### 5.1.2 Lithium-ion Batteries

Lithium-ion batteries are becoming extremely common in consumer electronics, and are also starting to be used for automobiles and other applications that have been historically within the realm of lead-acid batteries.

They function on a slightly different principle compared to lead-acid batteries. Lithium-ion batteries operate based on an intercalation/de-intercalation of $Li^+$ ions. The positive electrode is generally a metal oxide, while the negative electrode is usually composed of carbon and is almost always graphitic. These electrodes are submerged in an electrolyte; the electrolyte is commonly composed of organic carbonates containing a lithium complex. During discharge, $Li^+$ ions, which are situated in the carbon matrix, leave the electrode and diffuse into the positive electrode, where the metal oxide is reduced. Charging is the reverse of this physical process – the metal oxide is oxidized and the electrons flow to the carbon electrode where they meet the diffusing $Li^+$ ions.[276]

Given the high energy density compared to lead-acid batteries, lithium-ion batteries are gaining traction in many commercial electronics applications. However, like lead-acid batteries, they suffer from diminishing capacity upon repeated charging cycles due to the irreversible formation of lithium oxides. As a result, most lithium-ion batteries generally have lifespans less than three years.[277] Also, minable reserves of lithium are located in only a few areas of the world – primarily South America and Asia. It is relatively energy- and time-intensive to purify the lithium from these salt deposits.[278] Thus, despite the energy density of lithium-ion batteries, there are several issues that limit their efficiencies and cost effectiveness.

### 5.1.3 Supercapacitors

As stated above, supercapacitors are an emerging alternative to battery technologies. Supercapacitors are a specific kind of capacitor. Capacitors have two metallic electrodes separated by a dielectric (Figure 5.1). Upon applying a voltage to these two electrodes, positive and negative charges accumulate at the positive and negative electrodes, respectively. The capacitance is a function of the area of the electrodes and the distance between the two electrodes. The capacitance increases as the electrode area increases and the interstitial space decreases, which allows a greater energy to be stored at any given applied voltage. Capacitance is calculated by the following equation:

$$C = \varepsilon_0 \varepsilon_r \frac{A}{D}$$

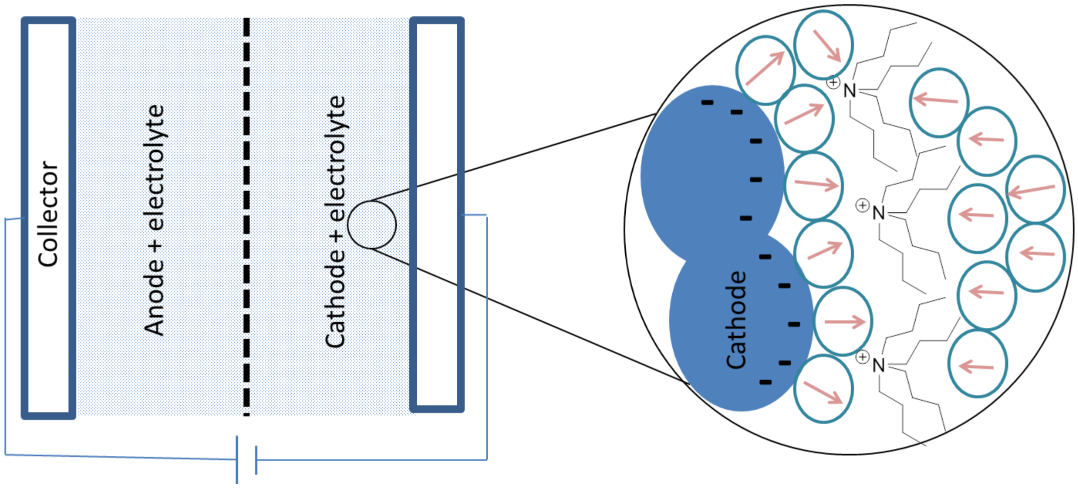

*Figure 5.2: Diagram of supercapacitor. Inset: illustration of solvent/electrolyte response to charging supercapacitor*

where C is the capacitance, $\varepsilon_0$ is the permittivity of free space, $\varepsilon_r$ is the dielectric constant of the insulating material between the electrodes, A is the area of the electrodes and D is the distance between the electrodes. The energy stored in a supercapacitor is directly proportional to the capacitance.[279]

Supercapacitors function on the same principles as a standard capacitor, but on a molecular scale (Figure 5.2). Instead of plate capacitors, supercapacitors have porous interconnected electrodes, generally composed of activated carbon. Like capacitors, these two electrodes can be composed of the same material. They are immersed in a solvent (either aqueous or organic) with a dissolved electrolyte. The two electrode compartments are separated by a dielectric separator. Upon charging, free charges accumulate at the surface of the porous electrodes. This has the effect of causing migration of the opposing charge in the electrolyte toward the electrode while counterions migrate toward the separator barrier; for example, at the positive electrode, electrolyte anions will migrate toward the electrode while the cations will move toward the separator. However, each of these solvated ions possesses a shell of solvent molecules, largely preventing direct contact between the electrode surface and the electrolyte ions. Upon being fully charged, the crevices of the porous electrode will be filled with solvent molecules and ions of opposite charge. Thus, supercapacitors function as capacitors, but on a molecular level utilizing process called electric double layer capacitance (EDLC). In this case, the electrodes are the charged porous electrode material and the electrolyte ions while solvent molecules serve as the dielectric material between them. This allows significantly more charge to be stored in supercapacitors versus capacitors of the same dimensions. Moreover, if the electrode materials are electrochemically active, they can engage in redox reactions with the electrolyte ions; the process of storing charge via redox reaction is dubbed pseudocapacitance (PC). Since the overall capacitance of a supercapacitor is determined by both EDLC and PC, a redox-active electrode material can store significantly more charge than by EDLC alone.[279]

Supercapacitors have the advantage of very quick charge/discharge cycles compared to batteries because of the quick charge accumulation on the porous electrode. The rate of charge/discharge is called the power density; supercapacitors can achieve much higher power densities compared to batteries. Additionally, commercial supercapacitors generally have much longer lifetimes than batteries because they rely on a physical process, whereas batteries undergo chemical reactions which lead to irreversible changes in the electrodes.[280] Finally, since supercapacitors often avoid the use of metals and corrosive materials, they tend to be more environmentally-friendly than batteries.[281] The disadvantages of supercapacitors are that they have a fraction of the energy density of batteries (i.e. how much energy is stored per unit volume) and generally

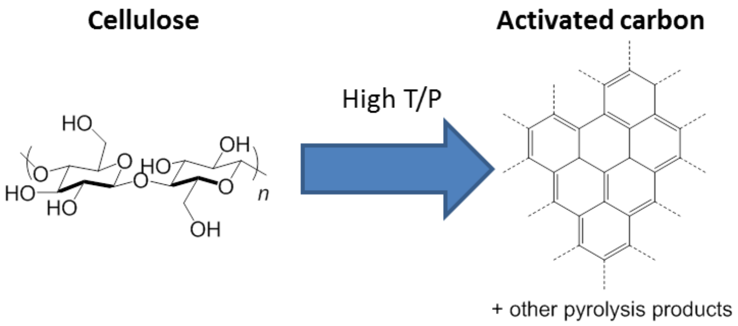

*Figure 5.3: Production of activated carbon from cellulosic materials*

have low voltage cells. Supercapacitors can only withstand low voltages before dielectric breakdown occurs; thus, several supercapacitors must be connected in series to achieve the voltages found in batteries.[282]

### 5.1.4 Activated Carbon for Supercapacitor Electrodes

Activated carbon has many advantages as a supercapacitor electrode material, including a high porosity (pore sizes ranging between 10 Å and ~500 Å with a surface area of ~500 $m^2/g$), reasonable conductivity (~50 S/cm), exceptional thermal/chemical stability and ease of production (Figure 5.3).[283] However, it has two main issues that limit its effectiveness as a supercapacitor electrode. The first is that the pore sizes of activated carbon are too small to be useful. This is problematic because these pores are generally too small to easily accommodate solvent molecules and electrolyte ions simultaneously. Thus, despite its incredibly high surface area, only a fraction of that surface area enables charge storage. Additionally, the small pore sizes hinder diffusion processes, thereby increasing the time needed for charge and discharge.[284] The second limitation is that by itself, activated carbon is not a redox-active material and cannot be oxidized or reduced.[285] Without the contribution of PC to the overall capacitance, the amount of charge stored in an activated carbon electrode is severely limited. They generally achieve capacitances up to 200 F/g.[283-284]

The first limitation can be addressed by changing the form of the activated carbon. Various groups have tried to utilize carbon aerogels and carbon nanotubes in the place of activated carbon.[286-293] Carbon aerogels are composed of carbon nanoparticles covalently bonded together. They have similar conductivities (10-100 S/cm) and can possess even higher surface areas (up to 1000 $m^2/g$).[294-295] Thus, carbon aerogels have achieved much higher capacitances than activated carbon (>500 F/g), but require tedious and expensive preparation.[296] Alternatively, carbon nanotubes can be made into an intertwined mat of fibers, yielding a porous matrix. Although they have lower surface areas compared to activated carbon and carbon aerogels, they have continuous diffusion pathways throughout their bulk, which enhances diffusion. Additionally, due to their well-defined conjugated structure, carbon nanotubes can have much higher conductivities (>500 S/cm) than activated carbon or carbon aerogels. This balance between surface area, conductivity and diffusion leads to carbon nanotube supercapacitors that show capacitances around 100 F/g.[297-302]

### 5.1.5 Pseudocapacitive Electrodes

Despite the success with activated carbon, carbon aerogels and carbon nanotubes, none of these materials are redox active. This severely limits the capacitance of the cell because PC can increase the overall capacitance of the supercapacitor by an order of magnitude or more.[283] Thus, it is worthwhile trying to find novel electrode materials that have controllable pore sizes and are also redox active, while maintaining good conductivity and electrochemical stability to both reduction and oxidation. There are not many materials that can satisfy all of these requirements. Of the few materials that are amenable to PC, there are two – metal oxides and semiconducting polymers – that have received the lion's share of research efforts.[279]

Transition metal oxides have been used by themselves as supercapacitor electrode materials, and also in conjunction with carbon electrodes in hybrid devices. Due to their ability to engage in PC, they can achieve much higher capacitances than carbon electrodes alone; by themselves, they have exhibited capacitances over 700 F/g[303-307] and in hybrid devices, they have been reported to achieve capacitances in excess of 1700 F/g.[308-309] Although they have been shown to have excellent supercapacitive properties, many of these materials are significantly more expensive than carbon-based electrodes and/or require extensive processing to fabricate the devices. As a result, these metal oxide supercapacitors have not yet become commercially viable.[310]

### 5.1.6 Semiconducting Polymers as Supercapacitor Electrode Materials

Thus, there is a great need to find an electrode material that is inexpensive, but can still achieve high capacitance through PC. Semiconducting polymers are a promising electrode material because they readily engage in redox reactions and tend to be inexpensive to fabricate and process.[311] Through synthetic chemistry, their physical characteristics can be controlled; they can be engineered to form a porous matrix, and the pore sizes of that matrix can be tuned precisely. Additionally, the electronic behavior of conjugated polymers can also be modified to alter their majority charge carriers and to enhance their conductivity and electrochemical stability.

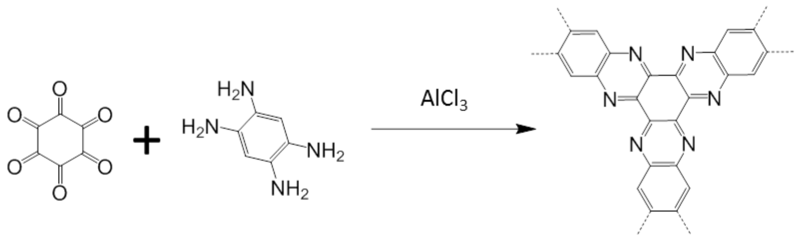

*Figure 5.4: Reported aza-fused polymer for supercapacitor electrodes*[313]

There are a number of studies on using conjugated organic polymers for supercapacitor electrodes. Of these, the most common polymers are derivatives of polythiophene, polyaniline and polypyrrole. These polymers typically show capacitance values on the order of ~200 F/g, with the best examples achieving upwards of 400 F/g.[312] However, given that most semiconducting organic molecules are p-type materials, they degrade upon n-doping, which makes them unsuitable for the negative electrode. Thus, the aforementioned reports on polymeric supercapacitor electrodes utilize activated carbon at the negative electrode or only construct half-cell electrodes. Additionally, these materials pack together fairly well in the solid state; polythiophenes are particularly crystalline. As a result, thin films of these polymers are not porous, which minimizes any contribution by EDLC to the overall capacitance.

This limitation inspired a handful of reports on porous semiconducting polymers, of which two will be discussed. The first example utilized an aza-fused polymer prepared by high temperature (300-500 °C) condensation reactions between 1,2,4,5-benzenetetramine and triquinoyl hydrate (Figure 5.4).[313] This produced a fused polymeric framework that is conductive throughout and has periodic pores. The aza units also enabled dipolar interactions with electrolyte cations. These features enabled the aza polymer to attain capacitance values near 950 F/g. Interestingly, these polymers are not

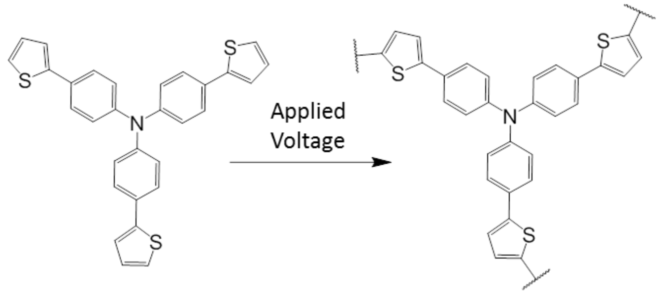

*Figure 5.5: Reported electropolymerizable TPA-based material for supercapacitor positive electrode*[314]

redox active and thus do not benefit at all from PC. The high capacitance occurs entirely from EDLC. The second example involved the electropolymerization of a tris(4-(thiophen-2-yl)phenyl)amine monomer into porous films (Figure 5.5).[314] Triphenylamines are particularly well-suited to a porous framework due to their reactivity at three equivalent sites. Additionally, their inherent propeller-like shape contributes to an amorphous hyperbranched structure. These polymers show capacitance values over 900 F/g, which is almost entirely due to PC; only ~1-2 F/g is contributed by EDLC.

The latter study directly inspired the research herein. The goal was to synthesize a similar porous polymeric matrix, but to modify the design such that the final polymer is ambipolar and stable to both p- and n-doping, thereby making it amenable for use as both the positive and negative electrodes of symmetric supercapacitors. This would eliminate the need for an asymmetric supercapacitor with one polymeric electrode and one activated carbon electrode, thereby decreasing the cost of fabricating such a device. An additional goal was to increase the pore size of the polymer matrix in the aforementioned publication to enhance the EDLC.

The triphenylamine (TPA) core is crucial to form a hyperbranched porous polymer matrix. Although TPA by itself is not amenable to reduction, the TPA arms can be modified with any number of conjugated moieties to tune the electronic properties of the resultant polymer. By affixing electron-deficient units to TPA, one can form ambipolar molecules that readily conduct both electrons and holes.

Two molecules that have been reported in the literature were most compelling, and were the basis for the design of the materials discussed within. The first material was based on a reported TPA-napthalene diimide (NDI) material.[315] This molecule showed ambipolar charge transport properties and good stability to both reduction and oxidation. A TPA-NDI molecule was synthesized. Attempts to electropolymerize this molecule were unsuccessful. To circumvent this issue, a Stille polymerization was used to chemically polymerize the TPA and NDI monomers. Initial symmetric supercapacitors were fabricated, but yielded poor capacitance (~0.5-1 F/g), although they possessed good stability over 500 cycles. Impedance spectroscopy of the devices revealed a high equivalent series resistance (ESR), which was likely due to the abundance of “dead ends” within the polymer matrix caused by limited conjugation throughout the polymer matrix, as well as low charge carrier mobilities in the polymer films.

To address these problems, the synthesis of an electropolymerizable material was attempted; it was hoped that this would create more continuous free charge pathways throughout the film, as well as to increase the mobility of the polymer film and to generate a better contact between the charge collector and the polymer. This second molecule was inspired by reports of ambipolar TPA-oxadiazole (OX) materials.[316] It was also hoped that since OX is less bulky than NDI, it would hinder electrolyte/solvent diffusion to a lesser extent. Also, to facilitate electropolymerization, 3,4-ethylenedioxythiophene rings were affixed to the terminal ends of the TPA-OX molecule.

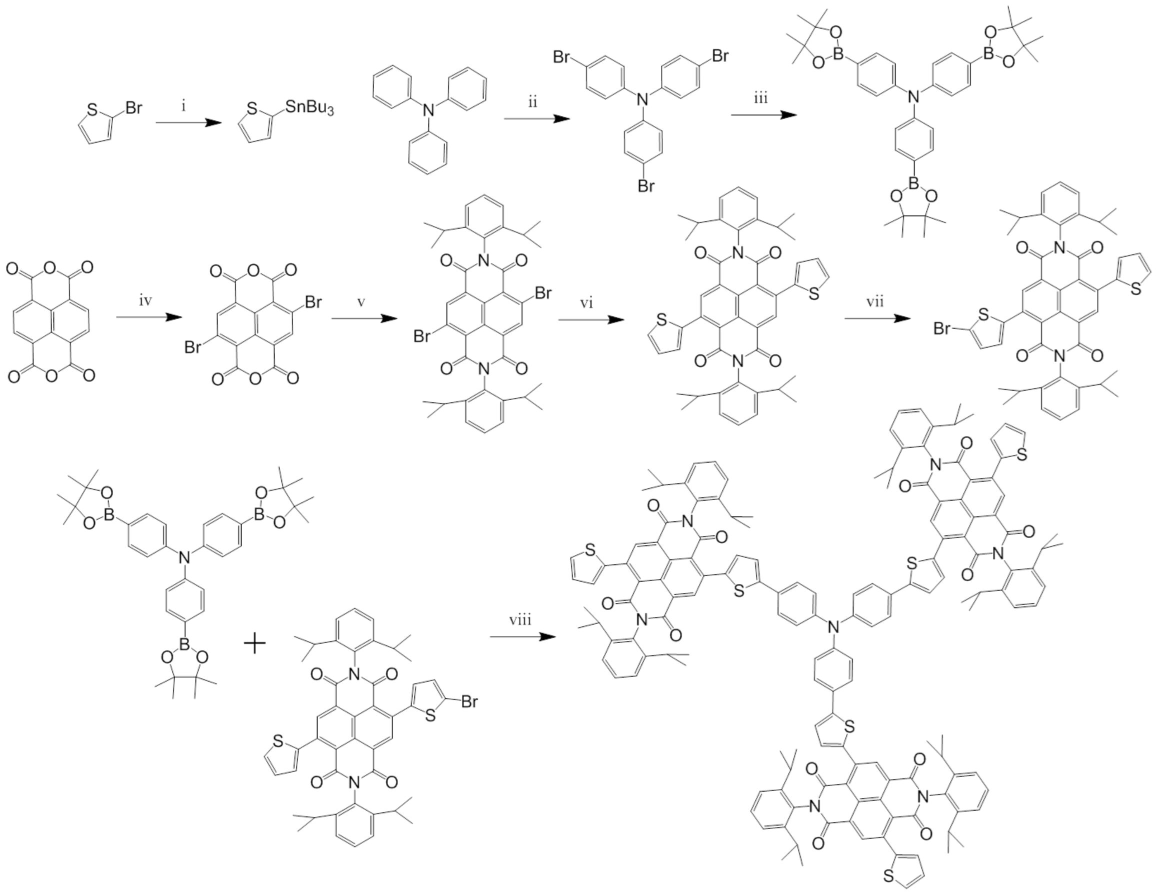

*Scheme 7: Synthesis of TPA-NDI monomer. i) 1) nBuLi, THF, -78 °C, 2) ClSnBu$_3$; ii) DMF, NBS, r.t., 20 h, 91%; iii) 1) nBuLi, THF, -78 °C, 2) 2-isopropoxy-4,4,5,5-tetramethyl-1,3,2-dioxaborolane, 69%; iv) dibromoisocyanuric acid, oleum, quant.; v) 2,6-diisopropylaniline, AcOH, 120 °C, 1 h, 27%; vi) 2-tributylstannylthiophene, Pd(PPh$_3$)$_4$, toluene, 100 °C, 24 h, 76%; vii) NBS, CHCl$_3$, 16 h, 35%; viii) Pd(PPh$_3$)$_4$, 2 M K$_2$CO$_3$, toluene, EtOH, 85 °C, 24 h, 71%*

## 5.2 Design and Synthesis of Triphenylamine-Napthalene Diimide Materials for Supercapacitors

The design for a TPA-NDI material was founded upon a previously reported structure of NDI flanked by two TPA molecules. This molecule showed reversible ambipolar behavior. To minimize the congestion within the pores of the subsequent

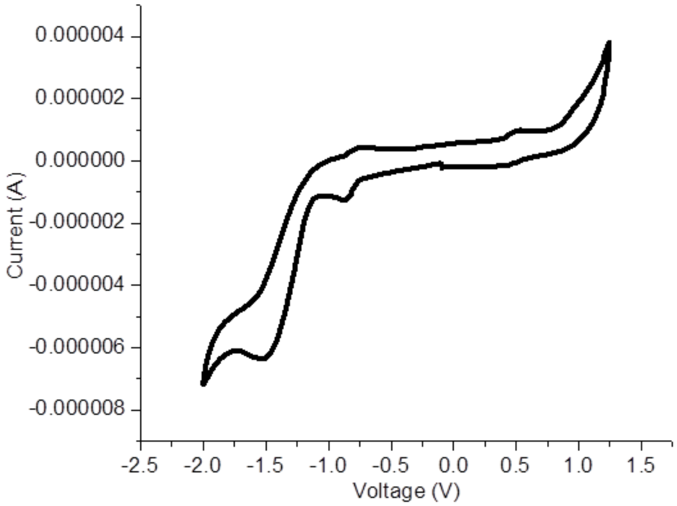

*Figure 5.6: CV scan for TPA-NDI small molecule*

polymer matrix, the naphthalene dianhydride was modified with 2,6-diisopropylamine. This was expected to strike a balance between improving the tractability of the molecule for purification and contributing to open pores for free solvent/electrolyte movement.

The first TPA-NDI material was a small molecule with a TPA core and NDI arms, with the hope that the molecule could be electropolymerized. Synthesis of the material began with the bromination of TPA, followed by lithiation and quenching with 2-isopropoxy-4,4,5,5-tetramethyl-1,3,2-dioxaborolane. Concurrently, naphthalene dianhydride was brominated and the anhydrides were converted to imides with 2,6-diisopropylamine. This molecule was coupled to thiophene at the bay positions using a Stille coupling and monobrominated with NBS. Finally, the TPA and NDI monomers were coupled using standard Suzuki coupling conditions.

The material was characterized with CV (Figure 5.6). It showed largely irreversible oxidation and reduction scans at 0.50 and -1.20 V, respectively. Following CV characterization, electropolymerization was attempted. Although thiophenes are

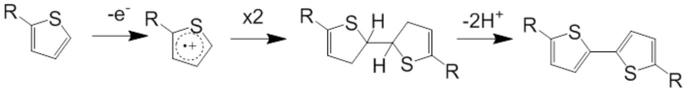

*Figure 5.7: Mechanism for oxidative coupling between thiophenes*

known to undergo electropolymerization readily, the material did not electropolymerize as expected. This is possibly because eleectropolymerization between thiophenes occurs by an oxidative process in which radical cations form on thiophene rings (monomers, dimers, oligomers, etc.) at the working electrode (Figure 5.7). Then, these oxidized thiophene rings diffuse through solution and an intermolecular coupling ensues between two radical cations, forming a C-C bond. Following the loss of two protons, the aromaticity of the thiophene rings is regained and the molecule can begin the electropolymerization process again.[317] However, electropolymerization relies on several requirements which must be satisfied for efficient electropolymerization of thiophene-containing molecules: the energy of the radical cation must be such that it is stable enough to diffuse away from the electrode without indiscriminately reacting with solvent molecules and the radical cation must be unstable enough to react upon encountering a second radical cation in solution. Finally, the spin density of the radical cation must be primarily centered at the α-position on the thiophene ring, since this is where the oxidative linking will occur. If the thiophene is connected to an electron deficient functionality, it will decrease the energy levels sufficiently that the radical cation will be extremely unstable and will react indiscriminately with solvent molecules before it diffuses to another radical cation. Conversely, if the thiophene is connected to an electron-donating moiety, the radical cation will be stabilized and may react sluggishly or not at all.[318]

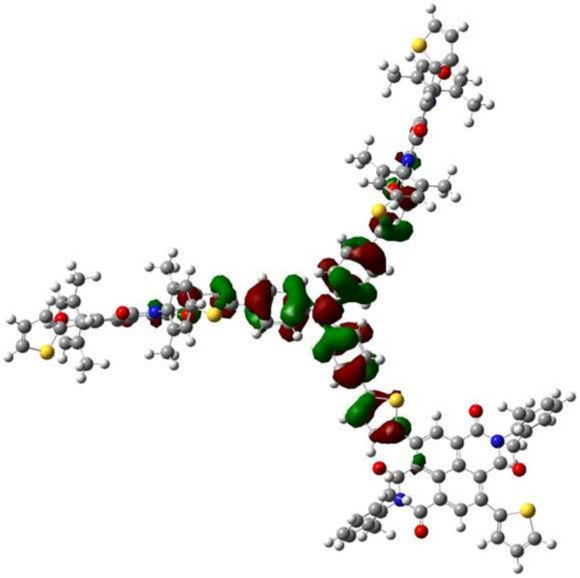

*Figure 5.8: Depiction of TPA-NDI HOMO, as calculated by DFT*

It is not clear why the TPA-NDI molecule did not electropolymerize. Since the oxidation potential ($E_{ox}$) of the material (ca. 0.75 V) is much lower than that of a thiophene ring (ca. 2 V), it could be that the radical cation is stabilized too much to react readily with other radical cations. However, given that the published report on the electropolymerized TPA-thiophene supercapacitor molecule had an even lower $E_{ox}$ (ca. 0.4 V)[296], this is unlikely. It is also possible that the spin density of the radical cation is shifted away from the terminal thiophene ring upon oxidation. Since the thiophene rings are adjacent to the electron deficient NDI unit, it is conceivable that the radical cation becomes localized on the electron-rich TPA core, making any thiophene-thiophene linkages unlikely. This theory was confirmed by DFT calculations (Figure 5.8). The HOMO is exclusively centered on the TPA core, with no electron density at the peripheral thiophene rings.

To circumvent this inability to undergo electropolymerization, the intermediates obtained previously were used to perform a solution-based synthesis of a series of

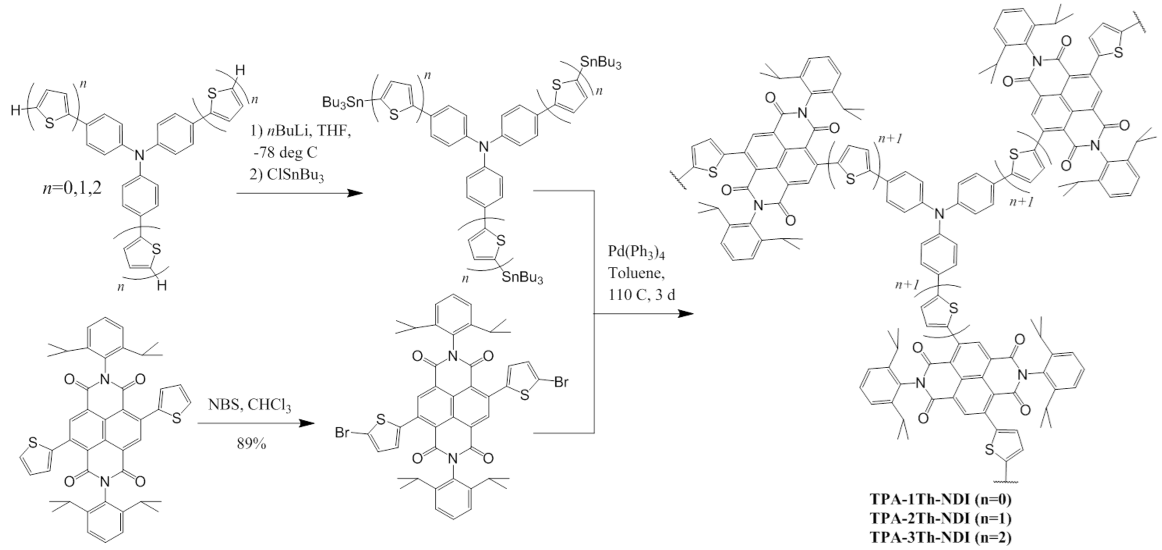

*Scheme 8: Synthesis of TPA-(n)Th-NDI polymers i) NBS, $CHCl_3$, 24 h, 87%; ii) 1) nBuLi, THF, 1 h, -78 °C, 2) $ClSnBu_3$, r.t., overnight; iii) $Pd(PPh_3)_4$, toluene, 120 °C, 3 d, 45%;*

three TPA-NDI polymers (Scheme 8). Additionally, the number of thiophene rings between each TPA and NDI functionality was modified; it was hoped that this would also modify the pore sizes of the polymer films. One or two thiophene rings were affixed to the TPA unit using standard Stille coupling conditions and the materials were thenceforth polymerized with the NDI monomer to yield three polymers. Although the lack of solubilizing chains on the polymer led to the polymer prematurely precipitating from solution, it was thought that this would be preferable compared to introducing long alkyl chains on the NDI unit, which would potentially clog pores in the polymer matrix and hinder electrolyte diffusion.

Initial experiments were performed on TPA-1Th-NDI in an attempt to understand how these materials function in the context of supercapacitors. First, the oxidation and reduction processes in the polymer were characterized by CV at different scan rates. Interestingly, the CV spectra (Figure 5.9) exhibit reversible reduction scans and largely irreversible oxidation scans. According to the CV spectra, TPA-1Th- NDI has reduction

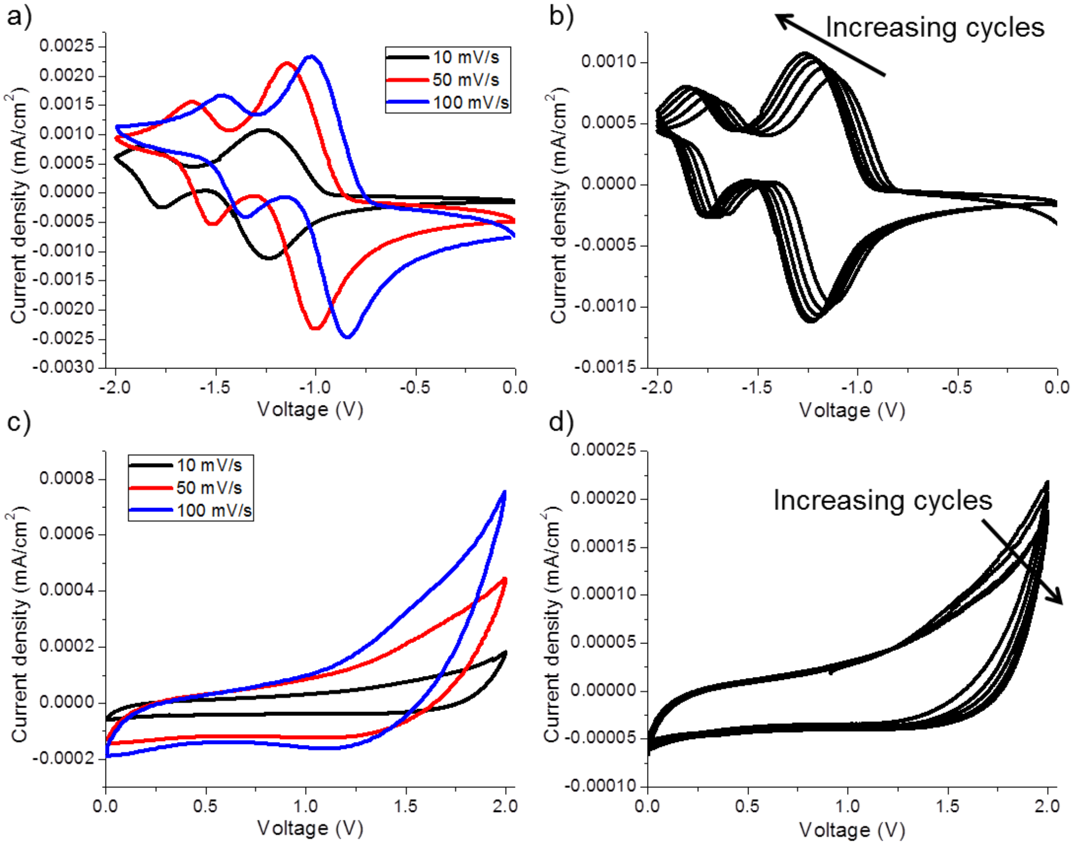

*Figure 5.9: Reduction (a, b) and oxidation (c, d) CV scans of TPA-1Th-NDI at different scan rates (a, c) and at 10 mV/s over 5 cycles (b, d)*

and oxidation onsets of -1.0 and 1.2 V. Additionally, the current response for TPA-1Th-NDI is much higher during reduction than oxidation.

Despite the poor response to oxidation, TPA-1Th-NDI was used to fabricate symmetric supercapacitors to satisfy the original goal of the project. First, the electronic transitions within the symmetric supercapacitor were examined with cyclic voltammetry (Figure 5.10a). The symmetric supercapacitor shows two main transitions. When overlaid with the oxidation and reduction scans of the polymer (Figure 5.10b), it becomes clear that the first transition is a conflation of the first reductive and oxidation processes. The

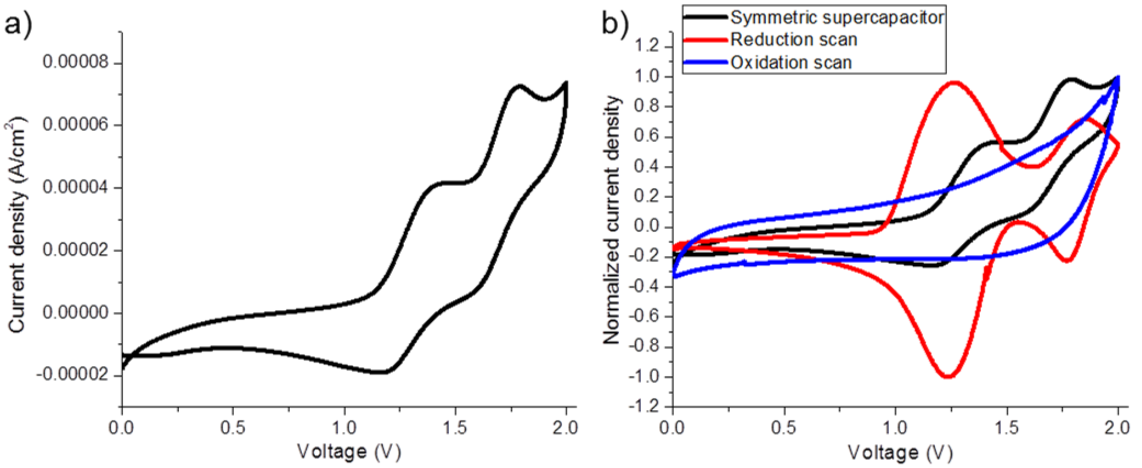

*Figure 5.10: CV scan of symmetric supercapacitor at 10 mV/s (a) and CV scans of symmetric supercapacitor overlaid with reduction and oxidation scans of TPA-1Th-TPA at 10 mV/s (b)*

second electronic transition in the symmetric device aligns well with the second reductive process of TPA-1Th-NDI. It is also worth noting that the current response of the symmetric supercapacitor is intermediate between the reduction and oxidation current responses.

Next, the charge storage capability of the device was studied with galvanic cycling from 0 to 2 V (Figure 5.11). The capacitance of TPA-1Th-NDI was calculated using the following equation for capacitance:

$$C = \frac{4(I)(t)}{(V)(m)}$$

where C is the capacitance, *I* is the discharge current (constant at 0.1 mA), *t* is the discharge time, *V* is the change in voltage during discharge and *m* is the mass of the sample. The charge and discharge processes each occur over ~40 s each at a charging rate of 0.1 mA. This leads to a very low overall capacitance (~0.5 F/g). However, the device

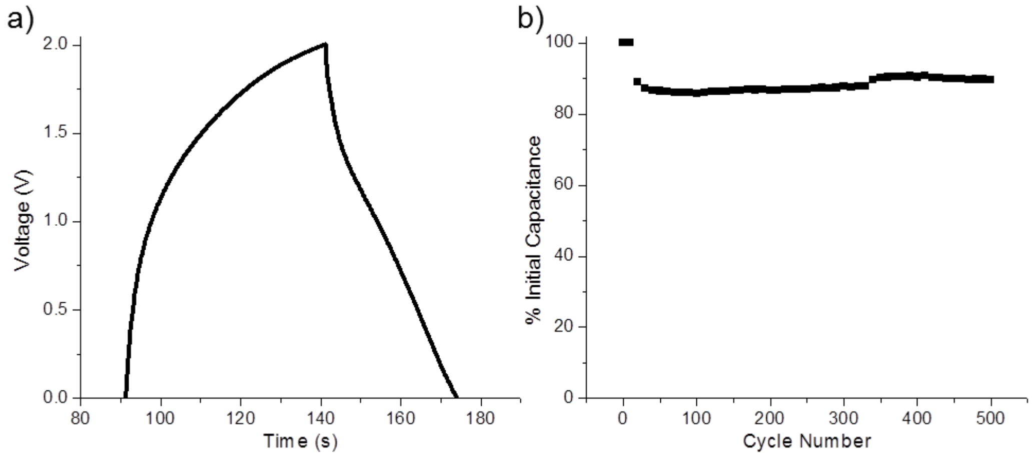

*Figure 5.11: Typical galvanic cycle at a charging rate of 0.1 mA (a) and stability (b) of symmetric supercapacitor utilizing TPA-1Th-NDI*

was exceptionally stable; it lost ~10% of its charge storage capacity over >500 cycles, which is promising for an organic material.

The underlying reasons for this poor capacitance were determined using electrochemical impedance spectroscopy (EIS), which is an effective way to determine resistances within a supercapacitor.[319] Essentially, EIS measurements reflect the electronic response of the supercapacitor when a sinusoidal potential is applied to it. The frequency of the applied potential generates different solutions to a complex form of Ohm's law:

$$Z = Z_o(\cos\phi + i\sin\phi)$$

where Z is the impedance, $Z_o$ is the magnitude of impedance, and $\phi$ represents the phase shift between stimulus and response, which is dependent upon the frequency of stimulus. Thus, any given frequency will produce a real term ($Z' = Z_o\sin\phi$) and an imaginary term ($Z'' = iZ_o\cos\phi$). By plotting the real and imaginary terms for each frequency on the x- and y-axes, respectively, a Nyquist plot is obtained. At higher frequencies, the Nyquist

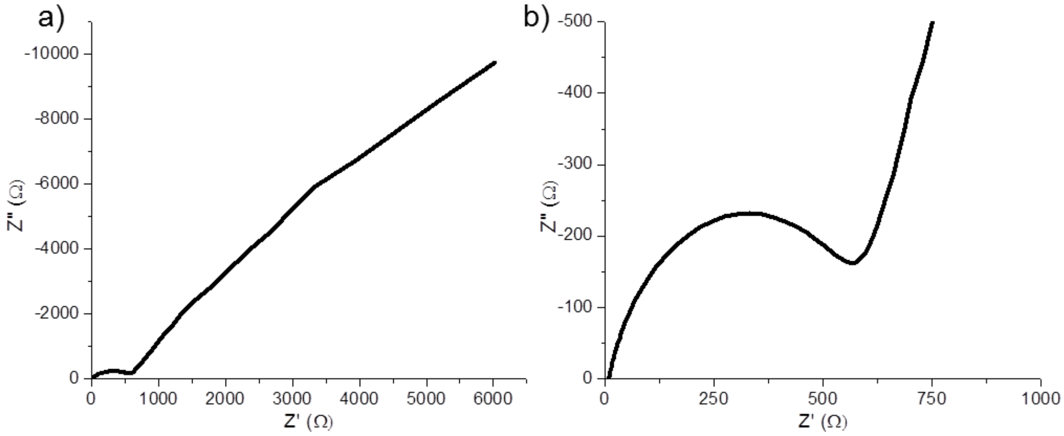

*Figure 5.12: Nyquist plots of symmetric supercapacitor over entire frequency range (a) and at high frequencies (b)*

plot provides information about electronic processes within the electrode – i.e. redox reactions in the polymer. Where the Nyquist plot intersects the x-axis reflects the equivalent series resistance (ESR); the ESR is a measure of the ohmic resistances in the device, including contributions from the electrolyte conductivity, electrode material conductivity, and contact between the electrode and current collector. Typical ESR values are around 2 Ω.[297,300] The diameter of the semi-circle at high frequencies indicates the charge-transfer resistance ($R_{ct}$) of the electrode; this value describes how easily the polymer engages in redox reactions with the electrolyte. Polymer-based supercapacitors usually possess charge transfer resistances of 5-10 Ω.[320] Additionally, the slope of the Nyquist plot at lower frequencies reflects the diffusivity resistance to the electrolyte; a more vertical line suggests minimal resistance diffusion while a horizontal line reflects severe resistance to diffusion.

The EIS characterization of the device revealed a very high $R_{ct}$ of ~570 Ω and a somewhat high ESR of ~9 Ω (Figure 5.12). The ESR is likely higher than is typically seen for several reasons. First and foremost, the solution-based polymerization yields relatively low molecular weight polymers. When these are utilized as a supercapacitor electrode, there are very limited complete free charge pathways allowing charges to migrate to the charge collectors. Only those polymers closest to the charge collector will contribute to charge storage, whereas the charges stored Faradaically in other polymers cannot be collected. Additionally, since the polymer electrode is not physically bonded to the charge collector, there is poor electronic connection between the polymers and the charge collector; this contributes to resistance within the cell. Finally, conductive polymers generally have high mobilities because they can pack well in the solid state, allowing charges to migrate through the polymer domains via hopping. The high porosity engineered into this material is mutually exclusive with efficient solid state packing, limiting the hole and electron mobilities of the polymer and further contributing to resistance within the device.

It is less clear what caused the high $R_{ct}$ value. This value represents the resistance within the polymer to redox reactions. Based on the CV data for TPA-1Th-NDI, it is clear that the polymer responds poorly to oxidation. Thus, it is probable that the majority of the charge-transfer resistance occurs at the positive electrode. However, given that the symmetric supercapacitor is essentially two supercapacitors in series and the overall capacitance for the symmetric supercapacitor is calculated as:

$$\frac{1}{C_{Total}} = \frac{1}{C_{positive}} + \frac{1}{C_{negative}}$$

it is not clear whether both electrodes are contributing equally to the high $R_{ct}$ (and low $C_{total}$) or whether one is primarily responsible.

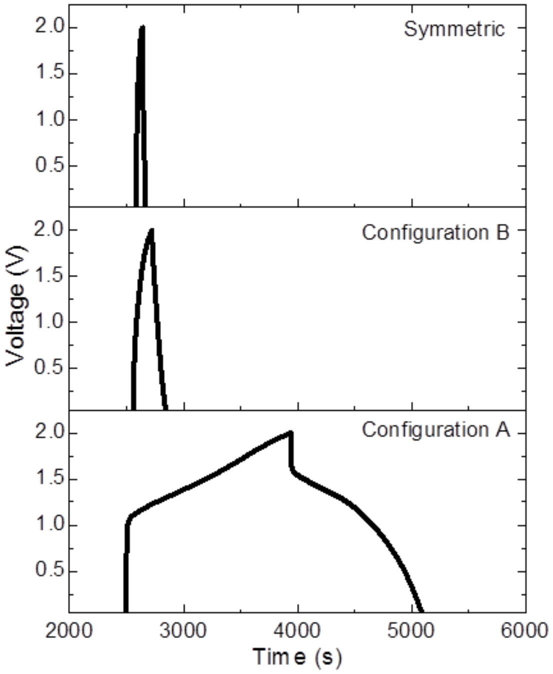

*Figure 5.13: Galvanic cycling curves taken at a rate of 0.1 mA of TPA-1Th-NDI in configurations A and B, with symmetric supercapacitor response for reference*

To further probe whence this resistance arises, asymmetric supercapacitors were fabricated with TPA-1Th-NDI as one electrode and activated carbon as the opposing electrode. In configurations A and B, TPA-1Th-NDI served as the negative and positive electrodes, respectively.

The (dis)charge curves from galvanic cycling (Figure 5.13) show that TPA-1Th-NDI functions much better as the negative electrode compared to the positive electrode. It takes ca. 200 s for configuration B to (dis)charge, while it takes ca. 1500 s for configuration A to (dis)charge, suggesting the polymer will have a higher capacitance as the negative electrode compared to the positive electrode. Indeed, the calculated

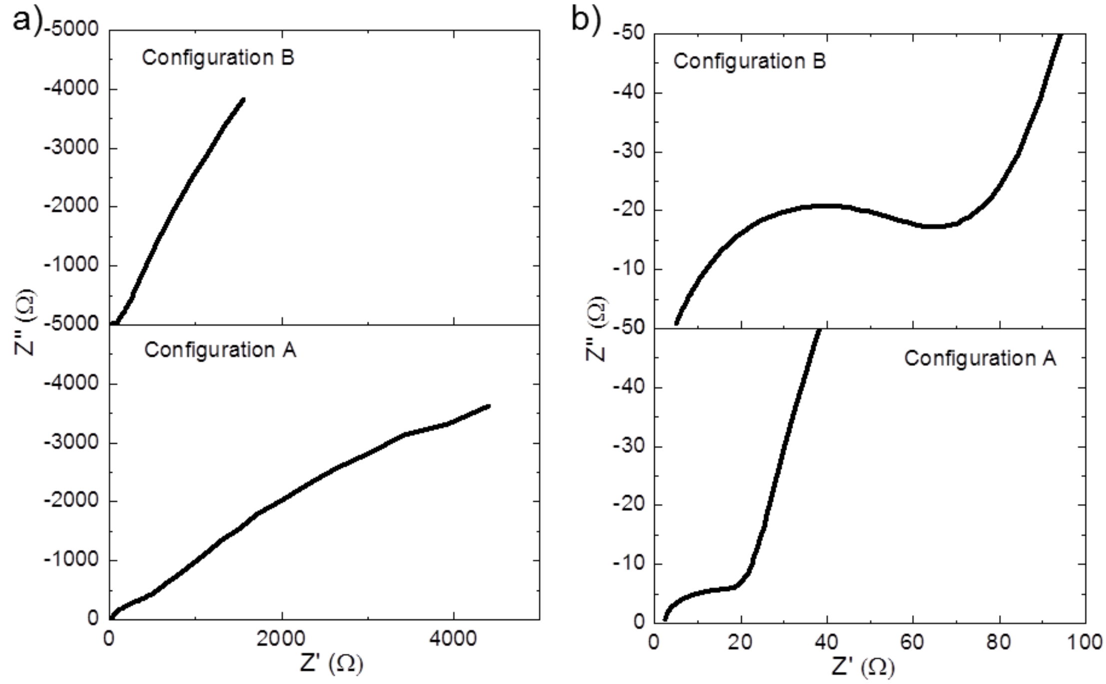

*Figure 5.14: Nyquist plots of TPA-1Th-NDI at (a) low and (b) high frequencies*

capacitance of configuration A (~22 F/g) is roughly one order of magnitude larger than that of configuration B (~2.8 F/g). Additionally, the galvanic cycle and capacitance value of the symmetric device are very similar to those of configuration B, while configuration A has a much different galvanic response and capacitance. This suggests that the poor performance of the symmetric device likely arises from the behavior of the polymer at the positive electrode, which dampens the overall capacitance of the symmetric device.

To quantify the resistance within the devices, Nyquist plots were generated for TPA-1Th-NDI in both configurations (Figure 5.14). The high frequency region makes it evident that there is a large difference between the reduction and oxidation of TPA-1Th-NDI. First, the ESR of configuration A (2.42 Ω) is less than half that of configuration B (5.05 Ω). The ESR is high, but not outlandishly so. Given that the electrolyte conductivity and electrode/charge collector contacts should be nearly identical regardless of the configuration, the disparity in ESR values likely reflects the difference in hole and electron mobilities of the polymer. The higher ESR of configuration B probably is the result of a lower hole mobility in the polymer compared to its electron mobility. Also of note are the relative diameters of the semi-circles at high frequency, which are used to calculate the $R_{ct}$ values. The $R_{ct}$ values of configuration A and B are 15.1 and 64.8 Ω, respectively. These impedance results suggest that the poor performance of the polymer as the positive electrode primarily stems from the slow kinetics of the oxidative redox reaction, as reflected in the high $R_{ct}$ value. Based on the CV plots of TPA-1Th-NDI, it is more favorably reduced – the reduction curve shows good reversibility and much higher current response. Additionally, the slope of the Nyquist plot at low frequencies suggests that electrolyte diffusion is hindered, which is likely due to the tortuous pathways within the polymer bulk. However, these Nyquist slopes are similar to other reported conjugated polymer-based supercapacitors.[313,320] Interestingly, the slope of configuration B is roughly twice as high as that of configuration A. This is likely due to the disparity in hydrodynamic radii of the positive (tetraethylammonium) and negative (tetrafluoroborate) electrolyte ions. Overall, the EIS tests suggest that the single largest hindrance to charge storage in configuration B is the slow charge transfer kinetics between the polymer and tetrafluoroborate ions.

Finally, the stability of configuration A and B were determined (Figure 5.15). Again, this polymer shows impressive stability for an organic material. There is also a clear difference in the stability between the two configurations. Configuration A loses only ~10% of its original capacitance after 500 cycles; conversely, configuration B loses ~20% after the same number of cycles. Interestingly, the symmetric device loses ~15% of

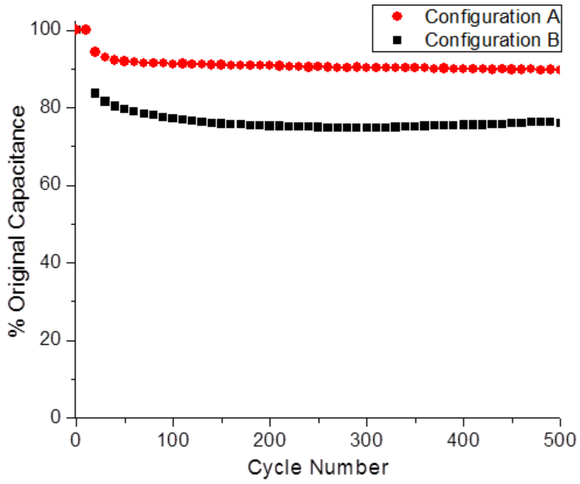

*Figure 5.15: Stability studies of configuration A and B over 500 cycles*

its capacitance over the same number of cycles, which is again intermediate between the configurations.

Following this characterization, TPA-2Th-NDI and TPA-3Th-NDI were used to fabricate asymmetric supercapacitors using configuration A. First, the two materials were characterized with CV (Figures 5.16 and 5.17). The three materials exhibit very similar electronic transitions. They all show two separate reduction processes and have nearly

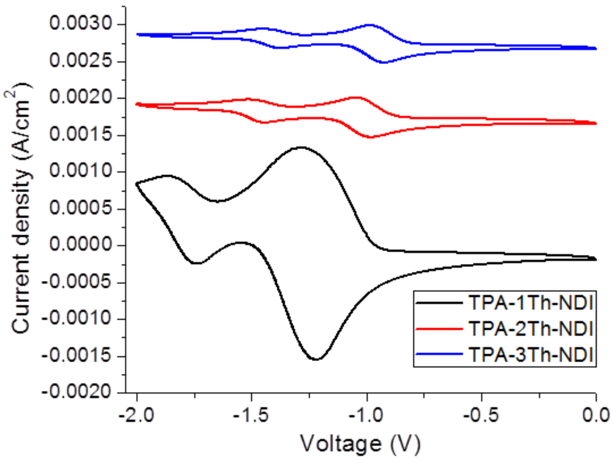

*Figure 5.16: CV spectra of the three TPA-(n)Th-NDI polymers.*

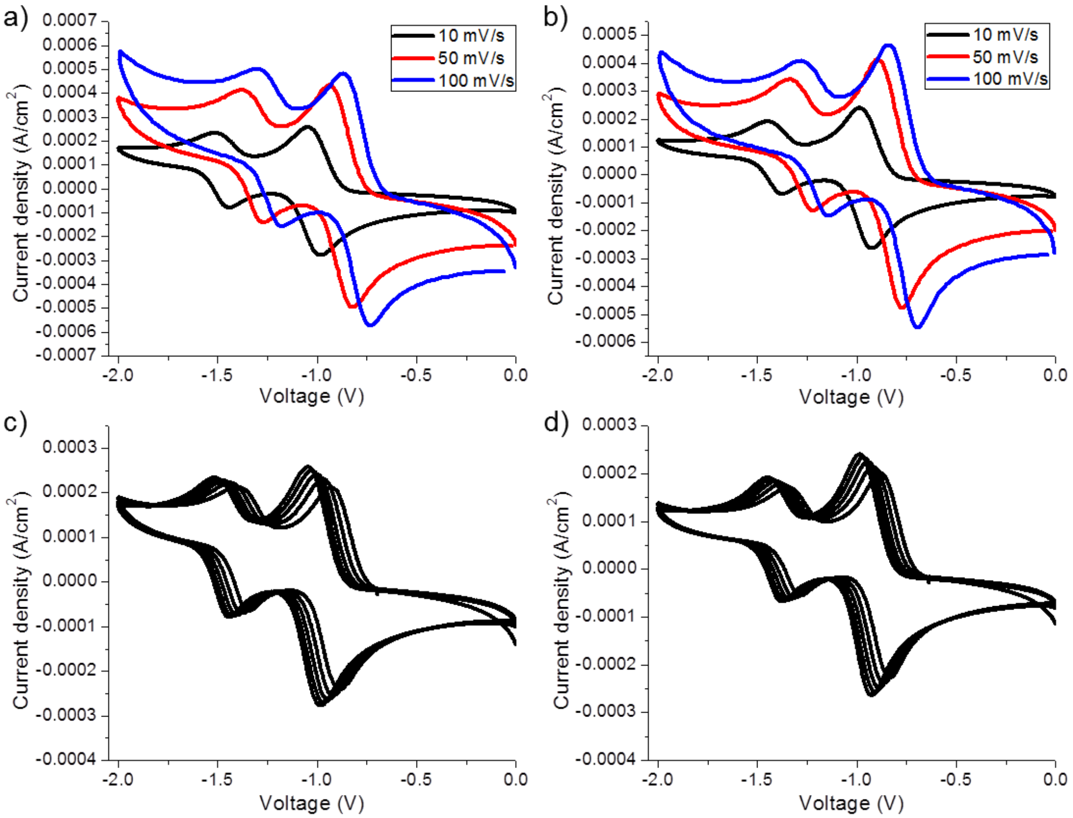

*Figure 5.17: CV spectra of TPA-2Th-NDI (a, c) and TPA-3Th-NDI (b, d) at different scan rates and over 5 cycles at 10 mV/s*

identical reduction onsets, as a result of the LUMO level of the D-A polymer being largely determined by the electron affinity of the NDI moiety; this also agrees with characterization of similar compounds in the literature.[321] Notably, the current response of TPA-1Th-NDI is roughly an order of magnitude more intense than those of TPA-2Th-NDI and TPA-3Th-NDI.

Subsequently, galvanic cycling was performed on the asymmetric supercapacitors. Typical charge/discharge cycles of TPA-1Th-NDI, TPA-2Th-NDI and TPA-3Th-NDI are shown in Figure 5.17. These tests reveal that TPA-2Th-NDI and TPA-3Th-NDI charge in ~200-300 s and discharge over another ~200-300 s. This information

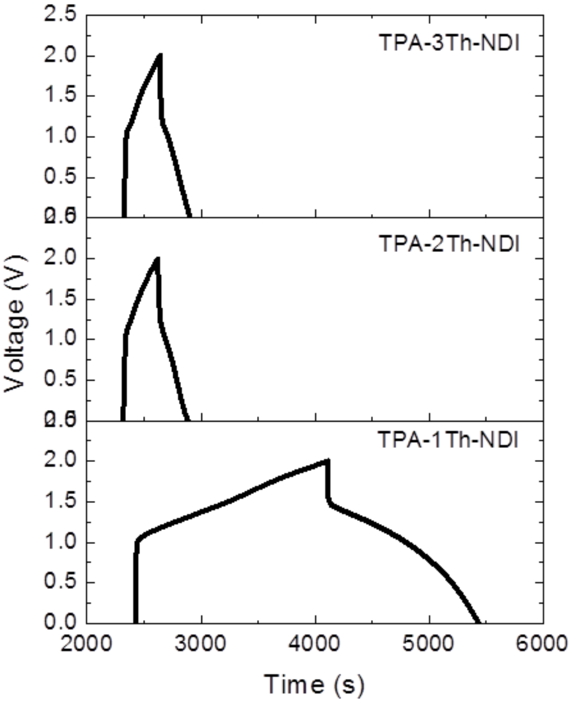

*Figure 5.18: Galvanic cycling of TPA-(n)Th-NDI polymers*

suggests that TPA-2Th-NDI and TPA-3Th-NDI will have smaller energy storage capacities compared to TPA-1Th-NDI. The calculated capacitance from the discharge curves verifies this; the gravimetric and volumetric capacitances of TPA-2Th-NDI (4.92 F/g and 3.85 F/cm$^3$) and TPA-3Th-NDI (4.94 F/g and 3.84 F/cm$^3$) are about 5-fold smaller than those of TPA-1Th-NDI.

Again, EIS was used to examine the reasons for this disparity in charge storage capacity (Figure 5.18). The ESR and $R_{ct}$ values increase sequentially from TPA-1Th-NDI (2.34 and 10.46 Ω) to TPA-2Th-NDI (2.40 and 10.63 Ω) to TPA-3Th-NDI (2.47 and 13.03 Ω). It is possible that adding thiophene spacers to these polymers (i.e. diluting the n-type NDI content) hinders their n-type behavior. This could decrease the electron mobility and/or slow the kinetics of reduction, which would thereby increase the ESR and

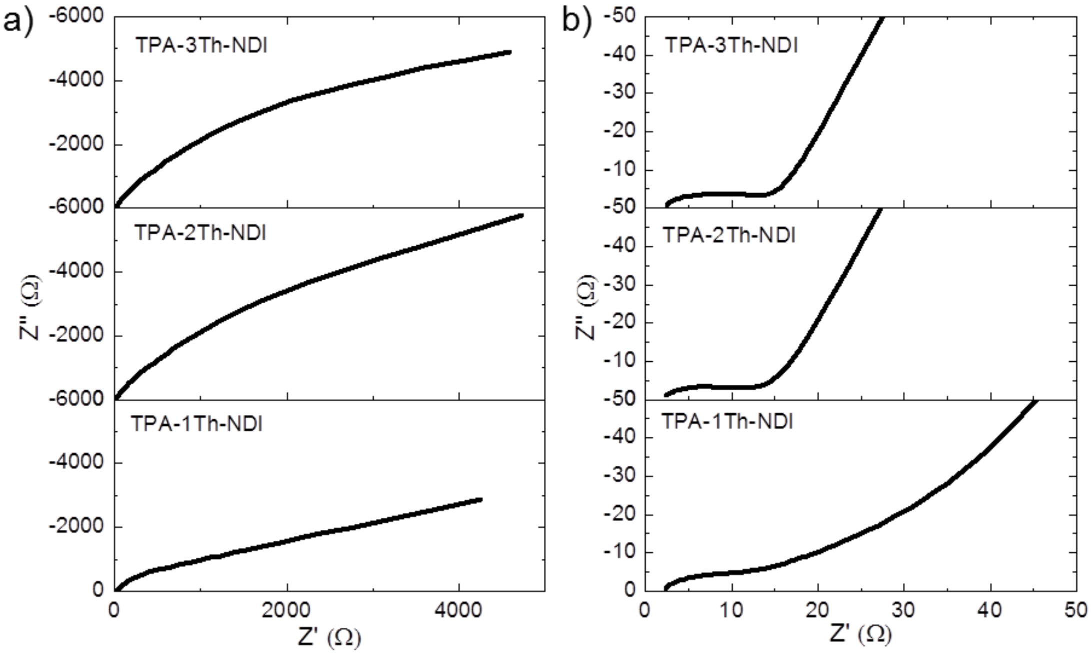

*Figure 5.19: Nyquist plots of TPA-(n)Th-NDI polymers at (a) low and (b) high frequencies*

$R_{ct}$. TPA-3Th-NDI experiences the largest increase in ESR and $R_{ct}$. This could be the result of having increasingly more p-type character. It has been shown in NDI-thiophene small molecules that conjugating more thiophene units to the NDI core results in increasing hole mobilities and decreasing electron mobilities.[321] This increasing p-type character could be the explanation for the increasingly lower current response upon reduction and higher ESR and $R_{ct}$ for TPA-2Th-NDI and TPA-3Th-NDI. Additionally, since reduction is a site-specific process, it is possible that adding thiophene spacers decreases the locations where reduction can favorably occur, thereby increasing the $R_{ct}$. Interestingly, the diffusivity resistances of TPA-2Th-NDI and TPA-3Th-NDI are qualitatively lower than that of TPA-1Th-NDI. This lends credence to the idea that adding thiophene spacers increases the pore sizes of the polymer matrix and facilitates diffusion.

### 5.3 Conclusions

An ambipolar material possessing TPA and NDI units was designed for use as the electrodes of symmetric supercapacitors. Initially, a TPA-NDI small molecule was synthesized, with the aim of electropolymerizing it into films, although ultimately this material was not amenable to electropolymerization; this is likely due to the fact that the electron density of the radical electron lies on TPA core, as opposed to the thiophene termini.

As a proof of concept, a solution-based polymerization was used to synthesize a series of three TPA-(n)Th-NDI polymers from the available intermediates. It was hoped that inserting thiophene spacers into the polymers would enhance the EDLC properties of the supercapacitors. These materials were characterized by CV. Each polymer exhibited reversible reduction and irreversible oxidation processes.

First, symmetric supercapacitors were fabricated using TPA-1Th-NDI. Although the device showed good stability over 500 cycles and predictable charge/discharge ability, it was limited by a marginal capacitance (~1 F/g). EIS characterization confirmed that the device had an exceedingly high $R_{ct}$ value (~550 Ω) and a slightly higher-than-average ESR (~9 Ω).

To further understand how the polymer behaved at each of the electrodes asymmetric supercapacitors were fabricated with activated carbon as the opposing electrode. This enabled TPA-1Th-NDI to be tested independently as the positive and negative electrode. Galvanic cycling of these configurations revealed that TPA-1Th-NDI functioned much better as the negative electrode than the positive electrode, which reflects its disfavored and slow oxidation kinetics. EIS confirmed this resistance to oxidation; the $R_{ct}$ values of TPA-1Th-NDI as the positive and negative electrodes were ~65 and ~15 Ω, respectively. Additionally, the ESR was doubled upon utilizing the polymer at the negative electrode.

With this information, all three polymers were incorporated into asymmetric supercapacitors with activated carbon positive electrodes. These devices revealed that TPA-1Th-NDI had the largest capacitance (~22 F/g) compared to TPA-2Th-NDI and TPA-3Th-NDI (both ca. 5 F/g). This disparity was examined using EIS. In all cases, the non-trivial ESR is probably the result of a combination of issues – e.g. low molecular weight polymers with low free charge carrier mobilities, few continuous free charge pathways, and poor contact between the polymer and the charge collector. Overall, both ESR and $R_{ct}$ values increased from TPA-1Th-NDI to TPA-3Th-NDI. It is speculated that the addition of thiophene spacers decreases the n-type character of the polymers and leads to slower reduction kinetics. The EIS characterization also revealed that the diffusivity resistance for the polymers decreased with the addition of thiophene spacers, in agreement with the original hypothesis.

## 5.4 Experimental

**Materials:** Unless otherwise specified, all chemicals were purchased from Aldrich or TCI and used without further purification. *N,N*-Di-(2,6-diisopropylphenyl)-2,6-dibromonaphthalene-1,4,5,8-tetracarboxylic acid bisimide,[322] tris(4-bromophenyl)amine,[323] tris[4-(4,4,5,5-tetramethyl-1,3,2-dioxaborolan-2-yl) phenylamine,[323] tris(4-tributylstannylphenyl)amine[324], tris(4-(thiophen-2-

yl)phenyl)amine,[325] and tris(4-(2,2'-bithiophen-2-yl)phenyl)amine[325] were prepared according to the literature.

**Supercapacitor fabrication:** The polymer was ground with a mortar and pestle and mixed with approximately 3 wt% of polytetrafluoroethylene (PTFE) as a binder. The mixture was mechanically rolled into sheets with a thickness of 0.07-0.08 mm and electrodes were punched out with a diameter of 10 mm. A Celgard® porous film separates the electrodes to prevent short circuiting and carbon-coated aluminum contacts were used as current collectors. The two-electrode assembly was pressed under vacuum overnight to ensure good contact between the electrodes and the current collectors and to remove moisture from the porous electrodes. The electrolyte used was 1 M tetraethylammonium tetrafluoroborate (TEATFB) in 1:1 propylene carbonate:dimethylcarbonate. The electrode assembly was placed in a flat cell and electrolyte as added in an argon-filled glovebox. The samples were placed under vacuum to increase the penetration of the electrolyte into the pores.

**Synthesis of *N,N*-Di-(2,6-diisopropylphenyl)-2,6-dithienylnaphthalene-1,4,5,8-tetracarboxylic acid bisimide:** *N,N*-Di-(2,6-diisopropylphenyl)-2,6-dibromonaphthalene-1,4,5,8-tetracarboxylic acid bisimide (6 mmol), 2-tributylstannylthiophene (18 mmol), and toluene (20 mL) were added to a flask. The contents were evacuated and backfilled with $N_2$ thrice. Then, $Pd(PPh_3)_4$ (0.6 mmol) was added quickly. The mixture was heated to 100 °C and stirred 24 h. After cooling, the mixture was filtered through a silica plug, concentrated and purified by silica gel chromatography ($CHCl_3$:Hex 3:1) to yield a bright red solid. Yield: 76%. $^1$H NMR (300

MHz, $CDCl_3$, $\delta$): 8.89 (s, 2H), 7.56 (dd, 2H), 7.52 (t, 2H), 7.40-7.35 (m, 6H), 7.17 (dd, 2H), 2.79 (m, 4H), 1.18 (d, 24H)

**Synthesis of *N,N*-Di-(2,6-diisopropylphenyl)-2-(2-bromothienyl)-6-thienyl-naphthalene-1,4,5,8-tetracarboxylic acid bisimide:** *N*,*N*-Di-(2,6-diisopropylphenyl)-2,6-dithienylnaphthalene-1,4,5,8-tetracarboxylic acid bisimide (2 mmol) was dissolved in $CHCl_3$ and cooled on an ice bath. The flask was protected from ambient sunlight. Then, NBS (2.2 mmol) was dissolved in $CHCl_3$ and added dropwise. The mixture was allowed to warm to room temperature and stirred for 16 h. The solution was poured into water, extracted, and the combined organic extracts were dried with $Na_2SO_4$ and concentrated. The residue was purified by column chromatography (($CHCl_3$:Hex 3:2) to yield a bright red solid. Yield: 35%. $^1H$ NMR (300 MHz, $CDCl_3$, $\delta$): 8.90 (s, 1H), 8.87 (s, 1H), 7.50 (dd, 1H), 7.46 (t, 2H), 7.40-7.35 (m, 6H), 7.13 (dd, 2H), 2.76 (m, 4H), 1.18 (d, 24H)

**Synthesis of TPA-NDI small molecule:** *N*,*N*-Di-(2,6-diisopropylphenyl)-2-(2-bromothienyl)-6-thienyl-naphthalene-1,4,5,8-tetracarboxylic acid bisimide (0.4 mmol), tris[4-(4,4,5,5-tetramethyl-1,3,2-dioxaborolan-2-yl) phenylamine (0.1 mmol), 2M $K_2CO_3$ (1 mL), toluene (3 mL), and EtOH (3 mL) were added to a flask. The contents were evacuated and backfilled with $N_2$ three times. Then, $Pd(PPh_3)_4$ (0.02 mmol) was added. The mixture was heated to 85 °C and stirred 24 h. After cooling, the mixture was filtered through a silica plug, concentrated and purified by silica gel chromatography ($CHCl_3$:Hex 3:1 to 100% $CHCl_3$) to yield a dark solid. Yield: 71%. $^1H$ NMR (300 MHz, $CDCl_3$, $\delta$): 8.97 (s, 3H), 8.81 (s, 3H), 7.71 (dd, 3H), 7.63 (dd, 3H), 7.55-7.30 (m, 27H), 7.20-7.00 (m, 12H), 2.72 (m, 4H), 1.15 (d, 24H)

**Synthesis of *N,N*-Di-(2,6-diisopropylphenyl)-2,6-(2-bromothienyl)-naphthalene-1,4,5,8-tetracarboxylic acid bisimide:** *N,N*-Di-(2,6-diisopropylphenyl)-2,6-dithienylnaphthalene-1,4,5,8-tetracarboxylic acid bisimide (2 mmol) was dissolved in $CHCl_3$ and cooled on an ice bath. The flask was protected from ambient sunlight. Then, NBS (4.4 mmol) was dissolved in $CHCl_3$ and added dropwise. The mixture was allowed to warm to room temperature and stirred for 16 h. The solution was poured into water, extracted, and the combined organic extracts were dried with $Na_2SO_4$ and concentrated. The residue was purified by column chromatography (($CHCl_3$:Hex 3:2) to yield a bright red solid. Yield: 83%. $^1$H NMR (300 MHz, $CDCl_3$, $\delta$): 8.87 (s, 2H), 7.51 (t, 2H), 7.39 (s, 2H), 7.36 (d, 2H), 7.16 (dd, 4H), 2.75 (m, 4H), 1.18 (d, 24H)

**Synthesis of TPA-1Th-NDI polymer:** *N*,*N*-Di-(2,6-diisopropylphenyl)-2,6-(2-bromothienyl)-naphthalene-1,4,5,8-tetracarboxylic acid bisimide (1.2 mmol), tris(3-tributylstannyl)phenylamine (0.30 mmol), and toluene (10 mL) were added to a flask. The contents were evacuated and backfilled with $N_2$ three times. Then, $Pd(PPh_3)_4$ (0.03 mmol) was added rapidly. The mixture was heated to 120 °C and stirred 72 h. After cooling, the mixture was poured into MeOH and filtered. The solid was Soxhlet extracted with methanol (12 h), acetone (24 h). The remaining solid was collected. Dark solid. Yield: 45%. $^1$H NMR (300 MHz, $CDCl_3$, $\delta$): 8.92 (br s), 7.75-7.55 (m), 7.45-7.00 (m), 2.72 (m), 1.15 (d)

**Synthesis of TPA-2Th-NDI polymer:** First, tris(4-(thiophen-2-yl)phenyl)amine (0.3 mmol) was dissolved in THF (30 mL) and cooled to -78 °C. Then, *n*-BuLi (0.93 mmol, 3.1 eq) was added dropwise. The solution was stirred at -78 °C for two hours. Then, tributyltin chloride (0.95 mmol, 3.2 eq) was added in one portion and the solution was allowed to warm to room temperature and was stirred overnight. Then, the solution was poured into water and extracted with ether. The combined organic solvents were dried over $Na_2SO_4$ and concentrated and was used without further purification. This material was added to *N*,*N*-Di-(2,6-diisopropylphenyl)-2,6-(2-bromothienyl)-naphthalene-1,4,5,8-tetracarboxylic acid bisimide (1.2 mmol) and toluene (10 mL) in a three-neck flask. The contents were evacuated and backfilled with $N_2$ three times. Then, $Pd(PPh_3)_4$ (0.03 mmol) was added rapidly. The mixture was heated to 120 °C and stirred 72 h. After cooling, the mixture was poured into MeOH and filtered. The solid was Soxhlet extracted with methanol (12 h), acetone (24 h). The remaining solid was collected. Dark solid. Yield: 45%. $^1$H NMR (300 MHz, $CDCl_3$, $\delta$): 8.90 (br s), 7.70-7.50 (m), 7.43-7.02 (m), 2.70 (m), 1.14 (d)

**Synthesis of TPA-3Th-NDI polymer:** First, tris(4-(2,2'-bithiophen-2-yl)phenyl)amine (0.4 mmol) was dissolved in THF (40 mL) and cooled to -78 °C. Then, *n*-BuLi (1.24 mmol, 3.1 eq) was added dropwise. The solution was stirred at -78 °C for two hours. Then, tributyltin chloride (1.27 mmol, 3.2 eq) was added in one portion and the solution was allowed to warm to room temperature and was stirred overnight. Then, the solution was poured into water and extracted with ether. The combined organic solvents were dried over $Na_2SO_4$ and concentrated and was used without further purification. This material was added to *N*,*N*-Di-(2,6-diisopropylphenyl)-2,6-(2-bromothienyl)-naphthalene-1,4,5,8-tetracarboxylic acid bisimide (1.6 mmol) and toluene (15 mL) in a three-neck flask. The contents were evacuated and backfilled with $N_2$ three times. Then, $Pd(PPh_3)_4$ (0.03 mmol) was added rapidly. The mixture was heated to 120 °C and stirred 72 h. After cooling, the mixture was poured into MeOH and filtered. The solid was

Soxhlet extracted with methanol (12 h), acetone (24 h). The remaining solid was collected. Dark solid. Yield: 45%. $^1$H NMR (300 MHz, CDCl$_3$, $\delta$): 8.91 (br s), 7.75-7.50 (m), 7.45-7.05 (m), 2.70 (m), 1.14 (d)

## 6. General Conclusions and Future Work

In summary, this body of work explored electronically-active organic materials with novel architectures and/or applications. Various ways to control the spectral and electronic properties of conjugated organic materials were investigated. Post-polymerization is one method to modify the optical and electronic properties of a polymer. In this work, a polymer comprised of a thiophene-triphenylamine backbone with aldehyde-functionalized indacenodithiophene side chains was synthesized. By performing Knoevenagel condensations on the aldehyde using three electron deficient molecules, the absorbance and electronic properties were changed drastically. This occurs because the HOMO lies along the polymer backbone while the LUMO sits at the terminus of the indacenodithiphene moiety; thus, the electron acceptor affects only the LUMO, leaving the highest occupied molecular orbital unchanged. Stronger electron acceptors decrease the LUMO energy progressively more, thereby decreasing the polymer bandgap and redshifting the internal charge transfer absorbance. Despite the increase in ICT intensity compared to existing side chain polymers and better overlap with the solar spectrum, these polymers showed modest hole mobilities (~$10^{-3}$ to $10^{-4}$ cm$^2$ V$^{-1}$ s$^{-1}$) and power conversion efficiencies (~2%). In the future, this strategy can be expanded to include different kinds of side chains and polymer backbones. It is clear that indacenodithiophene is not optimal as a π-bridge. Instead, a cyclopentadithiophene or fused bithiophene could be used as a π-bridge, either of which would hopefully improve the communication between the side chain and the main chain. Additionally, utilizing a planar backbone with minimal steric congestion seems to be advantageous. Thus, this strategy could be further explored by replacing triphenylamine with planar functionalities such as dithienopyrrole. Finally, instead of having a donor-donor type backbone, donor-acceptor backbones could be explored with side chains terminated by donating or accepting moieties.

A second way to modify the optical and electronic properties of a polymer is to graft it onto a second polymer with a significantly different bandgap. In this study, a polymer consisting of a carbazole-diketopyrrolopyrrole backbone and poly(3-hexylthiophene) side chains was synthesized using a graft through approach. The final polymers showed characteristics that were proportional to the amount of P3HT and donor-acceptor polymer in the material – shorter P3HT chains yielded graft copolymers that had more donor-acceptor character and *vice versa*. This was corroborated optically with UV-visible spectroscopy, physically with differential scanning calorimetry and electronically with cyclic voltammetry. Finally, the charge transport abilities of the polymers were investigated by fabricating organic field effect transistors with them. Interestingly, the polymer possessing the shortest P3HT chain showed ambipolar charge transport, similar to the linear donor-acceptor copolymer. However, longer P3HT chains exhibited only p-type transport. The main drawback to this strategy was that it necessarily used a graft through approach based on the requirements for the *ex situ* catalyst formation. Grafting P3HT from a donor-acceptor polymer would be much more preferable given the strict requirements for Suzuki and Stille polymerizations. Thus, different initiating species could be used. For example, inserting a phenyl linkage between the carbazole and toluene initiator would cause a significant torsional twist between the units and could further limit the electronic influence of the carbazole on the initiator. This could enable the use of a graft from approach and lead to improved efficiency of catalyst formation.

Additionally, a bi-functional dye was sought to serve as the basis for an energy-harvesting electrochromic window. To this end, several different classes of dyes were synthesized and their optical and electronic properties were probed with UV-visible spectroscopy and cyclic voltammetry. The first class utilized a perylene diimide core. Although this dye showed good stability and absorptive properties, it possessed minimal electrochromism upon reduction. The second class utilized a Methylene Blue scaffold. Unfortunately, despite its ideal absorption profile, this dye showed no electrochromism upon reduction. Finally, two phthalocyanine-based dyes were synthesized, both of which extended the conjugated core by appending pyrazine and succinimide rings, respectively. Both had relatively weak charge transfer absorption, likely due to poor overlap between the ground and excited state orbitals involved in the charge transfer state. However, due to its transparency, it was incorporated into a DSSC to see if it might be useful in conjunction with a separate electrochromic layer. Both iodide/triiodide and cobalt redox mediators were tested. Unfortunately, both showed poor efficiency, limited by a low short-circuit current density. Conversely, the succinimide-phthalocyanine showed a slightly more intense ICT absorption, imbuing it with a dark green color. Additionally, this material showed electrochromism upon reduction, transitioning to a magenta state. Unfortunately, the dye was only partially stable to reduction, degrading after repeated cycles. Clearly, there are a number of options for future work. One option is to modify a dye with known electrochromic properties in an attempt to satisfy the other requirements. That being said, it is entirely possible that no organic material can satisfy all the requirements to realize such a device.

Finally, an attempt was made to design and synthesize a porous ambipolar conjugated polymer that could replace activated carbon as the electrodes of symmetric supercapacitors. Although there has been limited exploration of porous conjugated frameworks for solar cells, using a porous ambipolar polymer for a symmetric supercapacitor is unprecedented. This required the design of a hyperbranched donor-acceptor polymer with ambipolar charge transport. The inspiration for this work was a publication utilizing a triphenylamine-based electropolymerized polymer. The first class of polymer utilized a triphenylamine-napthalene diimide polymer. Initial endeavors to electropolymerize the monomer failed; to circumvent this problem, a solution-based chemical polymerization was utilized. The material was used to fabricate a symmetric supercapacitor. Although the device showed meager capacitance (~1 F/g), it possessed excellent stability, only losing ~10% of its performance after 500 charge/discharge cycles. The reason for the poor capacitance was that the polymer had poor performance as a positive electrode.

To further understand how the polymer behaves at the two electrodes, asymmetric supercapacitors were fabricated and tested. The polymer showed a much better performance at the negative electrode, exhibiting a capacitance over 22 F/g; conversely, the positive electrode configuration had a capacitance slightly over 2 F/g. The reasons for this disparity were examined with impedance spectroscopy. The lower capacitance of the polymer as the positive electrode was the result of a high charge-transfer resistance as a result of the predominant n-type character of the polymer.

Subsequently, the two other TPA-(n)Th-NDI polymers were used to fabricate asymmetric supercapacitors. Both TPA-2Th-NDI and TPA-3Th-NDI had lower capacitances (both ca. 5 F/g) than TPA-1Th-NDI. EIS revealed that both ESR and $R_{ct}$ values increased from TPA-1Th-NDI to TPA-3Th-NDI. It is speculated that the addition of thiophene spacers decreases the n-type character of the polymers and leads to slower reduction kinetics. The EIS characterization also revealed that the diffusivity resistance for the polymers decreased with the addition of thiophene spacers, in agreement with the original hypothesis.

From here, the TPA-(n)Th-NDI polymers could be used to fabricate OFET devices to determine their relative hole and electron mobilities, providing more insight to why the ESR fluctuates across the different configurations and polymers. Additionally, to achieve higher capacitances, a new material should be designed. Electropolymerization is likely necessary to produce high mobility polymers, continuous charge pathways through the polymer matrix and good electrical contact between the polymer and charge collector. Finally, balanced hole and electron mobilities are necessary to produce electrodes with similar capacitances; the NDI unit imbues the polymers with too much n-type character. Additionally, replacing the NDI unit with a less bulky functionality would benefit electrolyte diffusion. A smaller and less electron-deficient monomer should be used.

## 7. List of Publications

1) Zeigler, D. F.; Mazzio, K. A.; Luscombe, C. K. *Macromolecules*, 2014, ASAP.

2) Yang, P.; Zeigler, D. F.; Bryant, K. C.; Martin, T. R.; Gamelin, D. R.; Luscombe, C. K. Identifying Effects of TiO2 Nanowires Inside Bulk Heterojunction Organic Photovoltaics on Charge Diffusion and Recombination. *J. Mater. Chem. C* 2014, *2*, 4922-4927.

3) Yang, P.; Yuan, M.; Zeigler, D. F.; Watkins, S. E.; Lee, J. A.; Luscombe, C. K. Influence of Fluorine Substituents on the Film Dielectric Constant and Open-circuit Voltage in Organic Photovoltaics. *J. Mater. Chem. C* 2014, *2*, 3278-3284.

4) Ji, Y.; Zeigler, D. F.; Lee, D. S.; Choi, H.; Jen, A. K.-Y.; Ko, H. C.; Kim, T.-W. Flexible and Twistable Non-volatile Memory Cell Array with All-organic One Diode-One Resistor Architecture. *Nature Commun.* 2013, *4*, 2707.

5) Yuan, M. J.; Durban, M. M.; Kazarinoff, P. D.; Zeigler, D. F.; Rice, A. H.; Segawa, Y.; Luscombe, C. K. "Synthesis and Characterization of Fused-Thiophene Containing Naphthalene Diimide n-Type Copolymers for Organic Thin Film Transistor and All-Polymer Solar Cell Applications" *J. Polym. Sci. Part A; Polym. Chem.*, 2013, *51*, 4061-4069.

6) Zeigler, D. F.; Chen, K.-S.; Yip. H.-L.; Zhang, Y.; Jen, A. K.-Y. Tunable Light-Harvesting Polymers Containing Embedded Dipolar Chromophores for Polymer Solar Cell Applications. *J. Polym. Sci. Part A: Polym. Chem.*, 2012, *50*, 1362-1373.

7) Kim, T.-W.; Zeigler, D. F.; Acton, O.; Yip, H.-L.; Ma, H.; Jen, A. K.-Y. All Organic Photo-patterned One Diode-One Resistor Cell Array for Advanced Organic Nonvolatile Memory Applications. *Adv. Mater.*, 2012, *24*, 828-833.

8) Sun, Y.; Chien, S.-C.; Yip. H.-L.; Zhang, Y.; Chen, K.-S.; Zeigler, D. F.; Chen, F.-C.; Lin, B.; Jen, A. K.-Y. Chemically Doped and Cross-Linked Hole-Transporting Materials as an Efficient Anode Buffer Layer for Polymer Solar Cells. *Chem. Mater.*, 2011, *23*, 5006-5015.
9) Cho, N.; Yip, H.-L.; Davies, J. A.; Kazarinoff, P. D.; Zeigler, D. F.; Durban, M. M.; Segawa, Y.; O'Malley, K. M.; Luscombe, C. K.; Jen, A. K.-Y. In-Situ Crosslinking and n-doping of Semiconducting Polymers and Their Application as Efficient Electron-Transporting Materials in Inverted Polymer Solar Cells. *Adv. Ener. Mater.*, 2011, *1*, 1148-1153.
10) Zhang, Y.; Zou, J.; Yip, H.-L.; Chen, K.-S.; Zeigler, D. F.; Sun, Y.; Jen, A. K.-Y. Indacenodithiophene and Quinoxaline-Based Conjugated Polymers for Efficient Polymer Solar Cells. *Chem. Mater.*, 2011, *23*, 2289-2291.
11) Cho, N.; Yip, H.-L.; Hau, S. K.; Chen, K.-S.; Kim, T.-W.; Davies, J. A.; Zeigler, D. F.; Jen, A. K.-Y. N-Doping of Thermally Polymerizable Fullerenes as an Electron Transporting Layer for Inverted Polymer Solar Cells. *J. Mater. Chem.*, 2011, *21*, 6956-6961.

## 8. References

1. Morton, O. *Nature*. **2006**, *443*, 19-22
2. Yu, G.; Gao, J.; Hummelen, J. C.; Wudl, F.; Heeger, A. J. *Science*. **1995**, *270*, 1789-1791
3. Rösch, R. et al. *Energy Environ. Sci.*, **2012**, *5*, 6521-6540
4. Kroon, R.; Lenes, M.; Hummelen, J. C.; Blom, P. W. M.; De Boer, B. *Polym. Rev.* **2008**, *48*, 531-582
5. Dennler, G.; Scharber, M. C.; Brabec, C. J., *Adv. Mater.* **2009**, *21*, 1323-1338
6. Muhlbacher, D. S., M.; Morana, M.; Zhu, Z. G.; Waller, D.; Gaudiana, R.; Brabec, C., *Adv. Mater.* **2006**, *18*, 2884-2889

7. Li, H.; Kim, F. S.; Ren, G.; Jenekhe, S. A. *J. Am. Chem. Soc.* **2013**, *135*, 14920-14923
8. Earmme, T.; Hwang, Y. J.; Murari, N. M.; Subramaniyan, S.; Jenekhe, S. A. *J. Am. Chem. Soc.* **2013**, *135*, 14960-14963
9. Thompson, B. C.; Kim, Y. G.; McCarley, T. D.; Reynolds, J. R., *J. Am. Chem. Soc.* **2006**, *128*, 12714-12725
10. Wong, W. Y. *et al. J. Am. Chem. Soc.* **2007**, *129*, 14372-14380
11. Blouin, N.; Michaud, A.; Gendron, D.; Wakim, S.; Blair, E.; Neagu-Plesu, R.; Belletete, M.; Durocher, G.; Tao, Y.; Leclerc, M. *J. Am. Chem. Soc.* **2008**, *130*, 732-742
12. Chen, C. P.; Chan, S. H.; Chao, T. C.; Ting, C.; Ko, B. T. *J. Am. Chem. Soc.* **2008**, *130*, 12828-12833.
13. Hou, J. H.; Chen, H. Y.; Zhang, S. Q.; Li, G.; Yang, Y. *J. Am. Chem. Soc.* **2008**, *130*, 16144
14. Wang, E. G.; Wang, L.; Lan, L. F.; Luo, C.; Zhuang, W. L.; Peng, J. B.; Cao, Y. *Appl. Phys. Lett.* **2008**, *92*, 033307
15. Wienk, M. M.; Turbiez, M.; Gilot, J.; Janssen, R. A. J. *Adv. Mater.* **2008**, *20*, 2556
16. Chen, H. Y.; Hou, J. H.; Zhang, S. Q.; Liang, Y. Y.; Yang, G. W.; Yang, Y.; Yu, L. P.; Wu, Y.; Li, G. *Nature Photon.* **2009**, *3*, 649-653
17. Park, S. H.; Roy, A.; Beaupre, S.; Cho, S.; Coates, N.; Moon, J. S.; Moses, D.; Leclerc, M.; Lee, K.; Heeger, A. J. *Nature Photon.* **2009**, *3*, 297
18. Qin, R. P. *et al. J. Am. Chem. Soc.* **2009**, *131*, 14612
19. Yuan, M. J.; Rice, A. H.; Luscombe, C. K. *J. Polym. Sci. Part A: Polym. Chem.* **2011**, *49*, 701-711
20. Rice, A. H.; Giridharagopal, R.; Zheng, S. X.; Ohuchi, F. S.; Ginger, D. S.; Luscombe, C. K. *ACS Nano* **2011**, *5*, 3132-3140
21. Richards, J. J.; Rice, A. H.; Nelson, R. M.; Kim, F. S.; Jenekhe, S. A.; Luscombe, C. K.; Pozzo, D. C. Adv. *Funct. Mater.* **2013**, *23*, 514-522
22. Coakley, K. M.; McGehee, M. D. *Chem. Mater.* **2004**, *16*, 4533-4542
23. Blom, P. W. M.; Mihailetchi, V. D.; Koster, L. J. A.; Markov, D. E. *Adv. Mater.* **2007**, *19*, 1551-1566
24. Thompson, B. C.; Frechet, J. M. J. *Angew. Chem. Int. Ed.* **2008**, *47*, 58-77

25. Gunes, S.; Neugebauer, H.; Sariciftci, N. S. *Chem. Rev.* **2007**, *107*, 1324-1338

26. Giridharagopal, R.; Ginger, D. S.. *J. Phys. Chem. Lett.* **2010**, *1*, 1160-1169

27. Groves, C.; Reid, O. G.; Ginger, D. S. *Acc. Chem. Res.* **2010**, *43*, 612-620

28. Terao, J.; Wadahama, A.; Matono, A.; Tada, T.; Watanabe, S.; Seki, S.; Fujihara, T.; Tsuji, Y. *Nature Commun.* **2012**, *4*, 1-9

29. Brabec, C. J., Dyakonov, V., Parisi, J. and Sariciftci, N. S. *Organic Photovoltaics: Concepts and Realization*. Springer, Berlin, Germany, 300 p

30. Meier, H.; Stalmach, U.; Kolshorn, H. *Acta. Polym.* **1997**, 379-384

31. Klaerner, G.; Miller, R. D. *Macromolecules* **1998**, *31*, 2007-2009

32. Ma, J.; Li, S.; Jiang, Y. *Macromolecules* **2002** *35*, 1109-1115

33. Kuzmany, H.; Kurti, J. *Synth. Metals* **1987**, *21*, 95-102

34. Roncali, J. *Macromol. Rapid Commun.* **2007**, *28*, 1761-1775

35. Bredas, J. L.; Heeger, A. J. *Chem. Phys. Lett.* **1994**, *217*, 507-512

36. Cravino, A.; Sariciftci, N. S. *Nature Mater.* **2003**, *2*, 360-361

37. Li, H.; Kim, F. S.; Ren, G.; Jenekhe, S. A. *J. Am. Chem. Soc.* **2013**, *35*, 14920-14923

38. Wang, C.; Dong, H.; Hu, W.; Liu, Y.; Zhu, D. *Chem. Rev.* **2012**, *112*, 2208

39. Tsao, H. N.; Cho, D. M.; Park, I.; Hansen, M. R.; Mavrinskiy, A.; Yoon, D. Y.; Graf, R.; Pisula, W.; Spiess, H. W.; Müllen, K. *J. Am. Chem. Soc.* **2011**, 133, 2605.

40. Chen, H.; Guo, Y.; Yu, G.; Zhao, Y.; Zhang, J.; Gao, D.; Liu, H.; Liu, Y. *Adv. Mater.* **2012**, 24, 4589

41. Babel, A.; Jenekhe, S. A. *J. Am. Chem. Soc.* **2003**, 125, 13656

42. Yan, H.; Chen, Z.; Zheng, Y.; Newman, C.; Quinn, J. R.; Dötz, F.; Kastler, M.; Facchetti, A. Nature 2009, 457, 679

43. Guo, X.; Ortiz, R. P.; Zheng, Y.; Hu, Y.; Noh, Y.-Y.; Baeg, K.-J.; Facchetti, A.; Marks, T. J. J. Am. Chem. Soc. 2011, 133, 1405

44. Takeda, Y.; Andrew, T. L.; Lobez, J. M.; Mork, A. J.; Swager, T. M. Angew. Chem., Int. Ed. 2012, 51, 9042

45. Lee, J.-K.; Gwinner, M. C.; Berger, R.; Newby, C.; Zentel, R.; Friend, R. H.; Sirringhaus, H.; Ober, C. K. J. Am. Chem. Soc. 2011, 133, 9949

46. Lei, T.; Dou, J.-H.; Cao, X.-Y.; Wang, J.-Y.; Pei, J. *J. Am. Chem. Soc.* **2013**, 135, 12168

47. Facchetti, A. *Chem. Mater.* **2011**, 23, 733

48. Newman, C. R.; Frisbie, C. D.; da Silva Filho, D. A.; Bredas, J.-L.; Ewbank, P. C.; Mann,´K. R. Chem. Mater. **2004**, *16*, 4436

49. Sirringhaus, H. *Nature Mater.* **2003**, *2*, 641-642

50. Jen, K.-Y.; Miller, G. G.; Elsenbaumer, R. L. *J. Chem. Soc., Chem. Commun.* **1986**, *17*, 1346-1347

51. Chen, T. A.; Rieke, R. D. *J. Am. Chem. Soc.* **1992**, 114, 10087

52. McCullough, R.D.; Lowe, R. D. *J. Chem. Soc. Chem. Commun.* **1992**, 70

53. McCullough, R.D.; Lowe, R. D.; Jayaraman, M.; Anderson, D. L. *J. Org. Chem.* **1993**, 58, 904

54. McCullough, R.D.; Tristram-Nagle, S.; Williams, S. P.; Lowe, R. D.; Jayaraman, M. *J. Am. Chem. Soc.* **1993**, 115, 4910

55. McCullough, R. D. *Adv. Mater.* **1998**, 10, 93

56. Bao, Z. N.; Lovinger, A. J. *Chem. Mater.* **1999**, 11, 2607

57. Ma, W.; Yang, C.; Gong, X.; Lee, K.; Heeger, A. J. *Adv. Funct. Mater.* **2005**, 15, 1617

58. Zhang, Y.; Basel, T. P.; Gautam, B. R.; Yang, X.; Mascaro, D. J.; Liu, F.; Verdeny, Z. V. *Nature Commun.* **2012**, *3*, 1-7

59. Ryu, M. S.; Cha, H. J.; Jang, J. *Curr Appl Phys*, **2010**, *10*, S206–S209

60. Moule, A. J.; Meerholz, K. *Adv. Mater.* **2008**, *20*, 240-245

61. Loewe, R. S.; Ewbank, P. C.; Liu, J.; Zhai, L.; McCullough, R. D. *Macromolecules*, **2001**, 34, 4324

62. Kim, Y. et al. *Nature Mater.* **2006**, *5*, 197-203

63. Sai, N.; Li, Z. Q.; Martin, M. C.; Basov, D. N.; Di Ventra, M. *Phys. Rev.* **2007**, *75*, 045307

64. Kitamura, C.; Tanaka, S.; Yamashita, Y. *Chem. Mater*. **1996**, *8*, 570-578

65. Bakhshi, A. K.; Yamaguchi, Y.; Ago, H.; Yamabe, T. *J. Mol. Struct.* **1998**, *427*, 211-219

66. Pai, C.-L.; Liu, C.-L.; Chen, W.-C.; Jenekhe, S. A. *Polymer*, **2006**, *47*, 699-708

67. Liu, Y.; Liu, Y.; Zhan, X. *Macromol. Chem. Phys.* **2011**, *212*, 428-443

68. Patil, A. V.; Lee, W.-H.; Lee, E.; Kim, K.; Kang, I.-N.; Lee, S.-H. *Macromolecules* **2011**, *44*, 1238-1241

69. Chen, C.-H.; Hsieh, C.-H.; Dubosc, M.; Cheng, Y.-J.; Hsu, C.-S. *Macromolecules* **2010**, *43*, 697-708

70. Huo, L.; Hou, J.; Chen, H.-Y.; Zhang, S.; Jiang, Y.; Chen, T. L.; Yang, Y. *Macromolecules* **2009**, *42*, 6564-6571

71. Hou, J.; Park, M.-H.; Zhang, S.; Yao, Y.; Chen. L.-M.; Li, J.-H.; Yang, Y. *Macromolecules* **2008**, *41*, 6012-6018

72. Shi, M.-M.; Deng, D.; Chen, L.; Ling, J.; Fu, L.; Hu, X.-L.; Chen, H.-Z. *J. Polym. Sci. Part A: Polym. Chem.* **2011**, *49*, 1453-1461

73. Chen, G.-Y.; Chiang, C.-M.; Kekuda, D.; Lan, S.-C.; Chu, C.-W.; Wei, K.-H. *J. Polym. Sci. Part A: Polym. Chem.* **2010**, *48*, 1669-1675

74. Zhang, S.; Guo, Y.; Fan, H.; Liu, Y.; Chen. H.-Y.; Yang, G.; Zhan, X.; Liu, Y.; Li, Y.; Yang, Y. *J. Polym. Sci. Part A: Polym. Chem.* **2009**, *47*, 5498-5508

75. Zhang, Y.; Zou, J.; Yip, H.-L.; Sun, Y.; Davies, J. A.; Chen, K.-S.; Acton, O.; Jen, A. K.-Y. *J. Mater. Chem.* **2011**, *21*, 3895-3902

76. Zoombelt, A. P.; Mathijssen, S. G. J.; Turbiez, M. G. R.; Wienk, M. M.; Janssen, R. A. J. *J. Mater. Chem.* **2010**, *20*, 2240-2246

77. Zhang, X.; Steckler, T. T.; Dasari, R. R.; Ohira, S.; Potscavage, W. J. Jr.; Tiwari, S. P.; Coppee, S.; Ellinger, S.; Barlow, S.; Bredas, J.-L.; Kippelen, B.; Reynolds, J. R.; Marder, S. R. *J. Mater. Chem.* **2010**, *20*, 123-134

78. Facchetti, A. *Chem. Mater.* **2011**, *23*, 733-758

79. Zhou, H.; Yang, L.; Stoneking, S.; You, W. *ACS Appl. Mater. Inter.* **2010**, *2*, 1377-1383

80. Li, J.; Grimsdale, A. C. *Chem. Soc. Rev.* **2010**, *39*, 2399-2410

81. Chen, H.-Y.; Hou, J.; Zhang, S.; Liang, Y.; Yang, G.; Yang, Y.; Yu, L.; Wu, Y.; Li, G. *Nature Photon.* **2009**, *3*, 649-653

82. Bassler, H.; Kohler, A. *Top Curr. Chem.* **2012**, *312*, 1-66

83. Xu, T.; Yu, L. *Mater. Today* **2013**, *17*, 11-15

84. Deibel, C.; Dyakonov, V. *Rep. Prog. Phys.* **2010**, *73*, 096401

85. Roncali, J. *Acc. Chem. Res.* **2009**, *42*, 1719-1730

86. Huijser, A.; Savenije, T. J.; Meskers, S. C. J.; Vermeulen, M. J. W.; Siebbeles, L. D. A. *J. Am. Chem. Soc.* **2008**, *130*, 12496-12500

87. Feron, K.; Belcher, W. J.; Fell, C. J.; Dastoor, P. C. *Int. J. Mol. Sci.* **2012**, *13*, 17019-17047

88. Burlakov, V. M.; Kawata, K.; Assender, H. E.; Briggs, G. A. D., Ruseckas, A.; Samuel, I. D. W. *Phys. Rev. B* **2005**, *72*, 075206

89. Haugeneder, A.; Neges, M.; Kallinger, C.; Spirkl, W.; Lemmer, U.; Feldman, J.; Scherf, U.; Harth, E.; Gugel, A.; Mullen, K. *Phys. Rev. B.* **1999**, 59, 15346.

90. Kraabel, B.; McBranch, D.; Sariciftci, N. S.; Moses, D.; Heeger, A.J. *Phys. Rev. B.* **1994**, 50, 18543.

91. Brabec, C.; Zerza, G.; Cerullo, G.; De Silvestri, S.; Luzatti, S.; Hummelen, J.C.; Sariciftci, S. *Chem. Phys. Lett.* **2001**, 340, 232.

92. Parker, I. *J. Appl. Phys.* **1994**, 75, 1656

93. Chow, P. C. Y.; Gelinas, S.; Rao, A.; Friend, R. H. *J. Am. Chem. Soc.* **2014**, *136*, 3424-3429

94. Shieh, J.-T.; Liu, C.-H.; Meng, H.-F.; Tseng, S.-R.; Chao, Y.-C.; Horng, S.-F. *J. Appl. Phys.* **2010**, *107*, 084503

95. Tang, C. W. *Appl. Phys. Lett.* **1986**, *48*, 183-185

96. Peumans, Y. P. and Forrest, S. R. *J. Appl. Phys.* **2003**, *93*, 3693

97. Yu, G.; Heeger, A. J. *J. Appl. Phys.* **1995**, *78*, 4510

98. Yu, G.; Gao, J.; Hummelen, J. C.; Wudl, F.; Heeger, A. J. *Science* **1995**, 1789-1791

99. Heeger, A. J. *Adv. Mater.* **2014**, *26*, 10-28

100. Scharber, M. C.; Sariciftci, N S. *Prog. Polym. Sci.* **2013**, *38*, 1929-1940

101. Servaites, J. D.; Ratner, M. A.; Marks, T. J. *Appl. Phys. Lett.* **2009**, *95*, 163302

102. Padilla, M; Michi, B.; Thaidigsmann, B.; Warta, W.; Schubert, M. C. **2014**, *120*, 282-288

103. Perez, M. D.; Borek, C.; Forrest, S. R.; Thompson, M. E. *J. Am. Chem. Soc.* **2009**, *131*, 9281-9286

104. Fan, X. M.; Lian, J. S.; Guo, Z. X.; Lu, H. J. *Appl. Surf. Sci.* **2005**, *239*, 176

105. Scharber, M. C.; Muhlbacher, D.; Koppe, M.; Denk, P.; Waldauf, C.; Heeger, A. J.; Brabec, C. J. *Adv. Mater.* **2006**, *18*, 789-794
106. Stille, J. K. *J. Chem. Edu.* **1981**, *58*, 862-866
107. Yokozawa, T.; Yokoyama, A. *Prog. Polym. Sci.* **2007**, *32*, 147-172
108. Flory, P. J. *J. Am. Chem. Soc.* **1936**, *58*, 1877-1885
109. Rogosic, M.; Mencer, H. J.; Gomzi, Z. *Eur. Polym. J.* **1996**, *32*, 1337-1344
110. Yokoyama, A.; Yokozawa, T. *Macromolecules,* **2007**, 40, 4094
111. Kricheldorf, H. R. *Angew. Chem. Int. Ed.* **2006**, 45, 5752.
112. Shea, K. J.; Walker, J. W.; Zhu, H.; Paz, M.; Greaves, J. *J. Am. Chem. Soc.* **1997**, 119, 9049.
113. Goddard, J.-P.; Lixon, P.; Le Gall, T.; Mioskowski, C. *J. Am. Chem. Soc.* **2003**, 125, 9242.
114. Wang, B. *Macromolecules*, **2005**, 38, 643
115. Milstein, D.; Stille, J. K. *J. Am. Chem. Soc.* **1978**, *100*, 3636-3638
116. Stille, J. K. *Angew. Chem. Int. Ed.* **1986**, *25*, 508-524
117. Mitchell, T. N. *J. Organomet. Chem.* **1986**, *304*, 1-16
118. Espinet, P.; Echavarren, A. M. *Angew. Chem. Int. Ed.* **2004**, *43*, 4704-4734
119. Pattenden, G.; Sinclair, D. J. *J. Organomet. Chem.* **2002**, *653*, 261-268
120. Scott, W. J.; Crisp, G. T.; Stille, J. K. *Org. Synth.*, **1993**, Coll. Vol. 8, p 97
121. Stille, J. K.; Echavarren, A. M.; Williams, R. M.; Hendrix, J. A. *Org. Synth.*, **1998**, Coll. Vol. 9, p 553
122. Davidson, K.; Ponsonby, A. M. *Synth. Met.* **1999**, *102*, 1512-1513
123. Yang, Y.-L.; Lee, Y.-H.; Chang, C.-J.; Lu, A.-J.; Hsu, W.-C.; Wang, L.; Leung, M.-K.; Dai, C.-A. *J. Polym. Sci. Part A: Polym. Chem.* **2010**, *48*, 1607-1616
124. Hou, J.; Park, M.-H.; Zhang, S.; Yao, Y.; Chen, L.-M.; Li, J.-H.; Yang, Y. *Macromolecules* **2008**, *41*, 6012-6018
125. Liang, Y.; Feng, D.; Wu, Y.; Tsai, S.-T.; Li, G.; Ray, C.; Yu, L. *J. Am. Chem. Soc.* **2009**, *131*, 7792-7799
126. Casado, A. L.; Espinet, P.; Gallego, A. M. *J. Am. Chem. Soc.* **2000**, *122*, 11771-11782
127. Miyaura, N.; Yamada, K.; Suzuki, A. *Tet. Lett.* **1979,** *20*, 3437-3440

128. Miyaura, N.; Suzuki, A. *J. Chem. Soc.. Chem. Commun.* **1979**, *19*, 866-867
129. Matos, K.; Soderquist, J. A. *J. Org. Chem.* **1998**, *63*, 461-470
130. Amatore, C.; Jutand, A.; Le Duc, G. *Chem. Eur. J.* **2011**, *17*, 2492-2503
131. Smith, G. B.; Dezeny, G. C.; Hughes, D. L.; King, A. O.; Verhoeven, T. R. *J. Org. Chem.* **1994**, *59*, 8151-8156
132. Yokoyama, A.; Miyakoshi, R.; Yokozawa, T. *Macromolecules*, **2004**, 37, 116
133. Miyakoshi, R.; Yokoyama, A.; Yokozawa, T. *J. Am. Chem. Soc.* **2005**, *127*, 17542
134. Sheina, E. E.; Liu, J.; Iovu, M. C.; Laird, D. W.; McCullough, R. D. *Macromolecules* **2005**, *38*, 8649
135. Iovu, M. C.; Sheina, E. E.; Gil, R. R.; McCullough, R. D. *Macromolecules*, **2005**, 38, 8649.
136. Kiriy, A.; Senkovskyy, V.; Sommer, M. *Macromol. Rapid Commun.* **2011**, *32*, 1503-1517
137. V. Senkovskyy, N. Khanduyeva, H. Komber, U. Oertel, M. Stamm, D. Kuckling, A. Kiriy, *J. Am. Chem. Soc.* **2007**, *129*, 6626.
138. N. Khanduyeva, V. Senkovskyy, T. Beryozkina, V. Bocharova, F. Simon, M. Nitschke, M. Stamm, R. Groetzschel, A. Kiriy, *Macromolecules* **2008**, *41*, 7383
139. N. Doubina, M. Stoddard, H. A. Bronstein, A. K.-Y. Jen, C. K. Luscombe, *Macromol. Chem. Phys.* **2009**, *210*, 1966
140. McCormick, T. M.; Bridges, C. R.; Carrera, E. I.; DiCarmine, P. M.; Gibson, G. L.; Hollinger, J.; Kozycz, L. M.; Seferos, D. S. *Macromolecules* **2013**, *46*, 3879-3886
141. Dufresne, S.; Guarin, S. A. P.; Bolduc, A.; Bourque, A. N.; Skene, W. G. *Photochem. Photobiol. Sci.* 2009, *8*, 796-804
142. Huang, F.; Chen, K.-S.; Yip, H.-L.; Hau, S. K.; Acton, O.; Zhang, Y.; Luo, J.; Jen, A. K.-Y. *J. Am. Chem. Soc.*2009, *131*, 13886-13887
143. Hsu, S.-L.; Chen, C.-M.; Wei, K.-H. *J. Polym. Sci., Part A: Polym. Chem.*2010, *48*, 5128-5134.
144. Duan, C.; Chen, K.-S.; Huang, F.; Yip, H.-L.; Liu, S.; Zhang, J.; Jen, A. K.-Y.; Cao, Y. *Chem. Mater.* 2010, *22*, 6444-6452.
145. Sahu, D.; Padhy, H.; Patra, D.; Huang, J.-H.; Chu, C.-W.; Lin, H.-C. *J. Polym. Sci., Part A: Polym. Chem.*2010, *48*, 5812-5823.

146. Zhang, Z.-G.; Liu, Y.-L.; Yang, Y.; Hou, K.; Peng, B.; Zhao, G.; Zhang, M.; Guo, X.; Kang, E.-T.; Li, Y. *Macromolecules*. 2010, *43*, 9376-9383.

147. Marder, S. R.; Cheng, L.-T.; Tiemann, B. G.; Friedli, A. C.; Blanchard-Desce, M.; Perry, J. W.; Skindhøj, J. *Science*. 1994, *263*, 511-514.

148. Liu, S.; Haller, M. A.; Ma, H.; Dalton, L. R.; Jang, S.-H.; Jen, A. K.-Y. *Adv. Mater.*2003, *15*, 603.

149. Cheng, Y.-J.; Luo, J.; Hau, S.; Bale, D. H.; Kim, T.-D.; Shi, Z.; Lao, D. B.; Tucker, N. M.; Tian, Y.; Dalton, L. R.; Reid, P. J.; Jen, A. K.-Y. *Chem Mater.*2007, *19*, 1154-1163.

150. Shen, P.; Bin, H.; Xiao, L.; Li, Y. *Macromolecules* **2013**, *46*, 9575-9586

151. Hou, J. H.; Huo, L. J.; He, C.; Yang, C. H.; Li, Y. *Macromolecules* **2006**, *39*, 594-603

152. Fan, H.; Zhang, Z.; Li, Y.; Zhan, X. *J. Polym. Sci Part A; Polym. Chem.* **2011**, *49*, 1462-1470

153. Zhang, Z.-G.; Fan, H.; Min, J.; Zhang, J.; Zhang, M.; Guo, X.; Zhan, X.; Li, Y. *Polym. Chem.* **2011**, *2*, 1678-1687

154. Xie, H.; Zhang, K.; Duan, C.; Liu, S.; Huang, F.; Cao, Y. *Polym.* **2012**, *53*, 5676-5683

155. Sancho-Garcia, J. C.; Foden, C. L.; Grizzi, I.; Greczynski, G.; de Jong, M. P.; Salaneck, W. R.; Brédas, J.-L.; Cornil, J. *J. Phys. Chem. B*. 2004, *108*, 5594-5599

156. Schulz, G. L.; Chen, X.; Holdcroft, S. *Appl. Phys. Lett.* 2009, *94*, 023302

157. Zeigler, D. F.; Chen, K.-S.; Yip. H.-L.; Zhang, Y.; Jen, A. K.-Y.*J. Polym. Sci. Part A: Polym. Chem.*, **2012**, *50*, 1362-1373

158. Chen, C.-P.; Chan, S.-H.; Chao, T.-C.; Ting, C.; Ko, B.-T. *J. Am. Chem. Soc.*2008, *130*, 12828-12833

159. Chen, Y.-C.; Yu, C.-Y.; Fan, Y.-L.; Huang, L.-I.; Chen, C.-P.; Ting, C. *Chem. Commun.*2010, *46*, 6503-6505

160. Yu, C.-Y.; Chen, C.-P., Chan, S.-H.; Hwang, G.-W.; Ting, C. *Macromolecules*. 2009, *21*, 3262-3269.

161. Zhang, W. M.; Smith, J.; Watkins, S. E.; Gysel, R.;McGehee, M.; Salleo, A.;Kirkpatrick, J.; Ashraf, S.; Anthopoulos, T.; Heeney, M.; McCulloch, I. *J. Am. Chem. Soc.*2010, *132*, 11437.

162. Zhang, Y.; Zhou, J.; Yip, H.-L.; Chen, K.-S.; Zeigler, D. F.; Sun, Y.; Jen A. K.-Y. *Chem. Mater.* 2011, *23*, 2289-2291

163. Oberhumer, P. M.; Huang, Y.-S.; Massip, S.; James, D. T.; Tu, G.; Albert-Seifriend, S.; Beljonne, D.; Cornil, J.; Kim J.-S.; Huck, W. T. S.; Greenham, N. C.; Hodgkiss, J. M.; Friend, R. H. *J. Chem. Phys.* 2011, *134*, 114901

164. Poolmee, P.; Ehara, M.; Hannongbua, S.; Nakatsuji, H. *Polymer*. 2005, *46*, 6474-6481

165. Li, Z.; Zhao, Y.; Zhou, J.; Shen, Y. *Eur. Polym. J.* 2000, *36*, 2417-2421

166. Hohenberg, P.; Kohn, W. *Phys. Rev.* 1964, *136*, B864

167. Kohn, W.; Sham, L. J. *Phys. Rev.* 1965, *140*, A1133

168. Gaussian 09, Revision A.02, Frisch, M. J.; Trucks, G. W.; Schlegel, H. B.; Scuseria, G. E.; Robb, M. A.; Cheeseman, J. R.; Scalmani, G.; Barone, V.; Mennucci, B.; Petersson, G. A.; Nakatsuji, H.; Caricato, M.; Li, X.; Hratchian, H. P.; Izmaylov, A. F.; Bloino, J.; Zheng, G.; Sonnenberg, J. L.; Hada, M.; Ehara, M.; Toyota, K.; Fukuda, R.; Hasegawa, J.; Ishida, M.; Nakajima, T.; Honda, Y.; Kitao, O.; Nakai, H.; Vreven, T.; Montgomery, Jr., J. A.; Peralta, J. E.; Ogliaro, F.; Bearpark, M.; Heyd, J. J.; Brothers, E.; Kudin, K. N.; Staroverov, V. N.; Kobayashi, R.; Normand, J.; Raghavachari, K.; Rendell, A.; Burant, J. C.; Iyengar, S. S.; Tomasi, J.; Cossi, M.; Rega, N.; Millam, N. J.; Klene, M.; Knox, J. E.; Cross, J. B.; Bakken, V.; Adamo, C.; Jaramillo, J.; Gomperts, R.; Stratmann, R. E.; Yazyev, O.; Austin, A. J.; Cammi, R.; Pomelli, C.; Ochterski, J. W.; Martin, R. L.; Morokuma, K.; Zakrzewski, V. G.; Voth, G. A.; Salvador, P.; Dannenberg, J. J.; Dapprich, S.; Daniels, A. D.; Farkas, Ö.; Foresman, J. B.; Ortiz, J. V.; Cioslowski, J.; Fox, D. J. Gaussian, Inc., Wallingford CT, 2009

169. Lee, C.; Yang, W.; Parr, R. G. *Phys. Rev. B: Condens. Matter*1988, *37*, 785

170. Becke, A. D. *J. Chem. Phys.* 1993, *98*, 5648

171. Ditchfield, R.; Hehre, W. J.; Pople, J. A. *J. Chem. Phys.* 1971, *54*, 724

172. Blouin, N.; Michaud, A.; Gendron, D.; Wakim, S.; Blair, E.; Neagu-Plesu, R.; Belletête, M.; Durocher, G.; Tao, Y.; Leclerc, M. *J. Am. Chem. Soc.*2008, *130*, 732

173. Hirani, B.; Li, J.; Djurovich, P. I.; Yousufuddin, M.; Oxgaard, J.; Persson, P.; Wilson, S. R.; Bau, R.; Goddard, W. A.; Thompson, M. E. *Inorg. Chem.* 2007, *46*, 3865-3875

174. Boland, P.; Sunkavalli, S. S.; Chennuri, S.; Foe, K.; Abdel-Fattah, T.; Namkoong, G. *Thin Solid Films*. 2010, *518*, 1728-1731

175. D’Auria, M.; De Mico, A.; D’Onofrio, F.; Piancatelli, G. *J. Chem. Soc. Perkin Trans. I* 1987, 1777-1780.

176. Spagnolo, P.; Zanirato, P.; Gronowitz, S. *J. Org. Chem.*1982, *47*, 3177-3180.

177. Li, Z. H.; Wong, M. S. *Org. Lett.*2006, *8*, 1499.

178. Qian, G.; Dai, B.; Luo, M.; Yu, D.; Zhan, J.; Zhang, Z.; Ma, D.; Wang, Z. Y. *Chem. Mater.* 2008, *20*, 6208-6216.

179. Pham, C. van; Macomber, R. S.; Mark, H. B. Jr.; Zimmer, H. *J. Org. Chem.* 1984, *49*, 5250-5253.

180. Polman, A.; Atwater, H. A. *Nat. Mater.* **2012**, *11*, 174

181. P. Würfel, *Physics of Solar Cells*, Wiley-VCH, Weinheim, Germany, **2004**

182. Ameri, T.; Li, N.; Brabec, C. J. *Energy Environ. Sci.*, **2013**, *6*, 2390–2413

183. Riede, M.; Uhrich, C.; Widmer, J.; Timmreck, R.; Wynands, D.; Schwartz, G.; Gnehr, W.-M.; Hildebrandt, D.; Weiss, A.; Hwang, J.; Sundarraj, S.; Erk, P.; Pfeiffer, M.; Leo, K. *Adv. Funct. Mater.* **2011**, *21*, 3019-3028

184. You, J.; Dou, L.; Yoshimura, K.; Kato, T.; Ohya, K.; Moriarty, T.; Emery, K.; Chen, C.-C.; Gao, J.; Li, G.; Yang, Y. *Nat. Comm.* **2013**, *4*, 1-10

185. Kim, J. Y.; Lee, K.; Coates, N. E.; Moses, D.; Nguyen, T.-Q.; Dante, M.; Heeger, A. J. *Science*. **2007**, *317*, 222-225

186. Dennler, G.; Scharber, M. C.; Ameri, T.; Denk, P.; Forberich, K.; Waldauf, C.; Brabec, C. J. *Adv. Mater.* **2008**, *20*, 579-583

187. Yang, J.; Zhu, R.; Hong, Z.; He, Y.; Kumar, A.; Li, Y.; Yang, Y. *Adv. Mater.* **2011**, *23*, 3465-3470

188. Jo, J.; Pouliot, J.-R.; Wynands, D.; Collins, S. D.; Kim, J. Y.; Nguyen, T. L.; Woo, H. Y.; Sun, Y.; Leclerc, M.; Heeger, A. J. *Adv. Mater.* **2013**, *25*, 4783-4788

189. Li, K.; Li, Z.; Feng, K.; Xu, X.; Wang, L.; Peng, Q. *J. Am. Chem. Soc.* **2013**, *135*, 13549-13557

190. Meiss, J.; Menke, T.; Leo, K.; Uhrich, C.; Gnehr, W.-M.; Sonntag, S.; Pfeiffer, M.; Riede, M. *Appl. Phys. Lett.* **2011**, *99*, 043301

191. Dennler, G.; Prall, H.-J.; Koeppe, R.; Egginger, M.; Autengruber, R.; Sariciftci, N. S. *Appl. Phys. Lett.* **2006**, *89*, 073502

192. You, J.; Dou, L.; Yoshimura, K.; Kato, T.; Ohya, K.; Moriarty, T.; Emery, K.; Chen, C.-C.; Gao, J.; Li, G.; Yang, Y. *Nat. Commun.*, **2013**, *4*, 1446

193. M. A. Green, M. A.; Emery, K.; Hishikawa, Y.; Warta, W.; Dunlop, E. D. *Prog. Photovoltaics*, **2013**, *21*, 1

194. Yang, L.; Yan, L.; You, W. J. Phys. Chem. Lett., **2013**, 11, 1802–1810

195. Cheng, P.; Li, Y.; Zhan, X. *Energy Environ. Sci.* **2014**, advance article.

196. Khlyabich, P. P.; Burkhart, B.; Thompson, B. C. *J. Am. Chem. Soc.* **2011**, *133*, 14534-14537

197. Street, R. A.; Davies, D.; Khlyabich, P. P.; Burkhart, B.; Thompson, B. C. *J. Am. Chem. Soc.* **2013**, *135*, 986-989.

198. Hesse, H. C.; Weickert, J.; Hundschell, C.; Feng, X.; Müllen, K.; Nickel, B.; Mozer, A. J.; Schmidt-Mende, L. *Adv. Energy Mater.* **2011**, *1*, 861-869.

199. Hu, Z.; Tang, S.; Ahlvers, A.; Khondaker, S. i.; Gesquiere, A. J. *Appl. Phys. Lett.* **2012**, *101*, 053308

200. Koppe, M.; Egelhaaf, H. J.; Dennler, G.; Scharber, M. C.; Brabec, C. J.; Schilinsky, P.; Hoth, C. N. Adv. Funct. Mater. **2010**, 20, 338

201. Ameri, T.; Khoram, P.; Min, J.; Brabec, C. J. Adv. Mater. **2013**, 1-22

202. Bronstein, H. A.; Luscombe, C. K. *J. Am. Chem. Soc.* **2009**, *131*, 12894–12895

203. Segura, J. L.; Martin, N.; Guldi, D. M. *Chem. Soc. Rev.* **2005**, *34*, 31-47

204. Wang, M.; Wudl, F. *J. Mater. Chem.* **2012**, *22*, 24297-24314

205. Gao, H.; Matyjaszewski, K. *J. Am. Chem. Soc.* **2007**, 129, 6633-6639

206. Zhang, M.; Müller, A. H. E. *J. Polym. Sci. Part A: Polym. Chem.* **2005**, *43*, 3461-3481

207. Wang, J.; Lu, C.; Mizobe, T.; Ueda, M.; Chen, W.-C.; Higashihara, T. *Macromolecules* **2013**, *46*, 1783-1793

208. Marrocchi, A.; Lanari, D.; Facchetti, A.; Vaccaro, L. *Energy Environ. Sci.*, **2012**, *5*, 8457-8474

209. Zeigler, D. F.; Mazzio, K. A.; Luscombe, C. K. *Macromolecules*, **2014**, submitted.

210. Zou, Y.; Gendron, D.; Badrou-Aïch, R.; Najari, A.; Tao, Y.; Leclerc, M. *Macromolecules*. **2009**, *42*, 2891-2894

211. Kwon, O.; Barlow, S.; Odom, S. A.; Beverina, L.; Thompson, N. J.; Zojer, E.; Brédas J.-L.; Marder, S. R. *J. Phys. Chem. A* **2005**, *109*¸ 9346-9352.

212. Doubina, N.; Ho, A.; Jen, A. K.-Y.; Luscombe, C. K. *Macromolecules* **2009**, *42*, 7670-7677

213. Freeman, A. W.; Urvoy, M.; Criswell, M. E. *J. Org. Chem.* **2005**, *70*, 5014–5019

214. Jiang, W.; Duan, L.; Qiao, J.; Dong, G.; Zhang, D.; Wang, L.; Qiu, Y. *J. Mater. Chem.* **2011**, *21*, 4918-4926

215. Lee, O. P.; Yiu, A. T.; Beaujuge, P. M.; Woo, C. H.; Holcombe, T. W.; Millstone, J. E.; Douglas, J. D.; Chen, M. S.; Fréchet, J. M. J. *Adv. Mater.* **2011**, *45*, 5369-5363

216. Iovu, M. C.; Sheina, E. E.; Gil, R. R.; McCullough, R. D. *Macromolecules* **2005**, *38*, 8649–8656

217. Bilbrey, J. A.; Sontag, S. K.; Huddleston, N. E.; Allen, W. D.; Locklin, J. *ACS Macro Lett.* **2012**, *1*, 995–1000

218. Mao, Z.; Vakhshouri, K.; Jaye, C.; Fischer, D. A.; Fernando, R.; DeLongchamp, D. M.; Gomez, E. D.; Sauvé, G. *Macromolecules* **2013**, *46*, 103-112

219. Mao, Z.; Vakhshouri, K.; Jaye, C.; Fischer, D. A.; Fernando, R.; DeLongchamp, D. M.; Gomez, E. D.; Sauvé, G. *Macromolecules* **2013**, *46*, 103-112

220. Okamoto, K.; Luscombe, C. K.; *Chem. Commun.* **2014**, *50*, 5310-5312

221. Wetzel, S. J.; Guttman, C. M.; Flynn, K. M.; Filliben, J. J. *J. Am. Soc. Mass Spectrom.* **2006**, *17*, 246-252

222. Khan, M. S.; Al-Mandhary, M. R. A.; Al-Suti, M. K.; Ahrens, B.; Mahon, M. F.; Male, L.; Raithby, P R.; Boothby, C. E.; Köhler, A. *Dalton Trans.* **2003**, *24*, 74-84

223. Wang, M.; Hu, X.; Liu, P.; Li, W.; Gong, X.; Huang, F.; Cao, Y. *J. Am. Chem. Soc.* **2011**, *133*, 9638–9641

224. Kularatne, R. S.; Sista, P.; Nguyen, H. Q.; Bhatt, M. P.; Biewer, M. C.; Stefan, M. C. *Macromolecules* **2012**, *45*, 7855−7862

225. Kuo, C.-Y.; Nie, W.; Tsai, H.; Yen, H.-J.; Mohite, A. D.; Gupta, G.; Dattelbaum, A. M.; William, D. J.; Cha, K. C.; Yang, Y.; Wang, L.; Wang, H.-L. *Macromolecules*. **2014**, *47*, 1008-1020.

226. Jiang, W.; Duan, L.; Qiao, J.; Dong, G.; Zhang, D.; Wang, L.; Qiu, Y. *J. Mater. Chem.* **2011**, *21*, 4918-4926

227. Letizia, J. A.; Salata, M. R.; Tribout, C. M.; Facchetti, A.; Ratner, M. A.; Marks, T. J. *J. Am. Chem. Soc.* **2008**, *130*, 9679-9694.
228. Lee, O. P.; Yiu, A. T.; Beaujuge, P. M.; Woo, C. H.; Holcombe, T. W.; Millstone, J. E.; Douglas, J. D.; Chen, M. S.; Fréchet, J. M. J. *Adv. Mater.* **2011**, *23*, 5359-5363.
229. O'Regan, B.; Gratzel, M. *Science* **1991**, *353*, 737-740
230. Wei, D. *Int, J. Mol. Sci.* **2010**, *11*, 1103-1113
231. Hagfeldt, A.; Gratzel, M. *Acc. Chem. Res.* **2000**, *33*, 269-277
232. Peter, L. *Acc. Chem. Res.* **2009**, *42*, 1839-1847
233. Boschloo, G.; Hagfeldt, A. *Acc. Chem. Res.* **2009**, *42*, 1819-1826
234. Wu, J.-J.; Hsieh, M.-D.; Liao, W.-P.; Wu, W.-T.; Chen, J.-S. *ACS Nano* **2009**, *3*, 2297-2303
235. Yanagida, S.; Yu, Y.; Manseki, K. *Acc. Chem. Res.* **2009**, *42*, 1827-1838
236. Nusbaumer, H.; Moser, J.-E.; Zakeeruddin, S. M.; Nazeeruddin, M. K.; Gratzel, M. *J. Phys. Chem. B* **2001**, *105*, 10461
237. Mishra, A.; Fischer, M. K. R.; Bauerle, P. *Angew. Chem. Int. Ed.* **2009**, *48*, 2474-2499
238. Hod, I.; Gonzalez-Pedro, V.; Tachan, Z.; Fabregat-Santiago, F.; Mora-Sero, I.; Bisquert, J.; Zaban, A. *J. Phys. Chem. Lett.* **2011**, *2*, 3032-3035
239. Lumpkin, R. S.; Kober, E. M.; Wort, L. A.; Murtaza, Z.; Meyer, T. J. *J. Phys. Chem.* **1990**, *94*, 239-243
240. Mortimer, R. J. *Electrochim. Acta* **1999**, *44*, 2971-2981
241. Beaujuge, P. M.; Reynolds, J. R. *Chem. Rev.* **2010**, *110*, 268-320
242. Garnier, F.; Tourillon, G.; Gazard, M.; Dubois, J. C. *J. Electroanal. Chem.* **1983**, *148*, 299
243. Gazard, M.; Dubois, J. C.; Champagne, M.; Garnier, F.; Tourillon, G. *J. Phys., Colloq.* **1983**, *44*, 537
244. Druy, M. A.; Seymour, R. J. *Org. Coat. Appl. Polym. Sci. Proc.***1983**, *48*, 561
245. Druy, M.; Seymour, R. *J. Phys., Colloq.* **1983**, *44*, 595
246. Basova, T.; Gurek, A. G.; Ahsen, V.; Ray, A. *Opt. Mater.* **2013**, *35*, 634-637
247. Silver, J.; Lukes, P.; Hey, P.; Ahmet, M. T. *J. Mater. Chem.* **1991**, *1*, 881-888
248. Wang, G.; Fu, X.; Deng, J.; Huang, X.; Miao, Q. *Chem. Phys. Lett.* **2013**, *579*, 105-110

249. Ganesan, V.; John, S. A.; Ramaraj, R. *J. Electroanal. Chem.* **2001**, *502*, 167-173

250. Ling, M.-M.; Erk, P.; Gomez, M.; Koenemann, M.; Locklin, J.; Bao, Z. *Adv. Mater.* **2007**, *19*, 1123-1127

251. Lu, W.; Gao, J. P.; Wang, Z. Y. *Macromolecules* **1999,** *32*, 8880-8885

252. Shibano, Y.; Umeyama, T.; Matano, Y.; Imahori, H. *Org. Lett.* **2007**, *9*, 1971-1974

253. Wang, M.; Zhang, Y.; Zhou, Y.; Yang, F.; Kim, E. J.; Hahn, S. H.; Seong, S. G. *Cryst. Eng. Comm.* **2013**, *15*, 754-763

254. Ghani, F.; Kristen, J.; Riegler, H. *J. Chem. Eng. Data* **2012**, *57*, 439-449

255. Birnbaum, T.; Hahn, T.; Martin, C.; Kortus, J.; Fronk, M.; Lungwitz, F.; Zahn, D. R. T.; Salvan, G. *J. Phys. Condens. Matter* **2014**, *26*, 104201

256. Yoon, S. M.; Lou, S. J.; Loser, S.; Smith, J.; Chen, L. X.; Facchetti, A.; Marks, T. *Nano Lett.* **2012**, 6315-6321

257. Lee, J. U.; Kim, Y. D.; Jo, J. W.; Kim, J. P.; Jo, W. H. *J. Mater. Chem.* **2011**, *21*, 17209

258. Bao, Z.; Lovinger, A. J.; Brown, J. *J. Am. Chem. Soc.* **1998**, *120*, 207-208

259. Varotto, A.; Nam, C.-Y.; Radivojevic, I.; Tome, J. P. C.; Cavaleiro, J. A. S.; Black, C. T.; Drain, C. M. *J. Am. Chem. Soc.* **2010**, *132*, 2552-2554

260. Walter, M. G.; Rudine, A. B.; Wamser, C. C. *J. Porphyrins Phthalocyanines* **2010**, *14*, 759-792

261. Calzaferri, G.; Rytz, R. *J. Phys. Chem.* **1995**, *99*, 12141-12150

262. "Reference Solar Spectral Irradiance: Air Mass 1.5", http://rredc.nrel.gov/solar/spectra/am1.5/

263. Jeong, M. J.; Park, J. H.; Lee, C.; Chang, J. Y. *Org. Lett.* **2006**, *8*, 2221-2224

264. Wurthner, F.; Stepanenko, V.; Chen Z.; Saha-Moller, C. R.; Kocher, N.; Stalke, D. *J. Org. Chem.* **2004**, *69*, 7933-7939

265. Frischmuth, A.; Knochel, P. *Angew. Chem. Int. Ed.* **2013**, *52*, 10084-10088

266. Mita, Y.; Noguchi-Yachide, T.; Ishikawa, M.; Hasimoto, Y. *Bioorg. Med. Chem.* **2013**, *21*, 608-617

267. Miao, Q.; Gao, J.; Wang, Z.; Yu, H.; Luo, Y.; Ma, T. *Inorg. Chim. Acta* **2011**, *376*, 619-627

268. Wolfe, J. P.; Tomori, H.; Sadighi, J. P.; Yin, J.; Buchwald, S. L. *J. Org. Chem.* **2000**, *65*, 1158-1174

269. Gorman, S. A.; Bell, A. L.; Griffiths, J.; Roberts, D.; Brown, S. B. *Dyes and Pigments* **2006**, *71*, 153-160
270. Shao, J.; Chang, J.; Chi, C.; *Org. Biomol. Chem.* **2012**, *10*, 7045-7052
271. Hasanon, J. *Egypt. J. Chem.* **2007**, *50*, 337
272. Freccero, M.; Fasani, E.; Albini, A. *J. Org. Chem.* **1993**, *58*, 1740-1745
273. Poullikkas, A. *Renew. Sust. Energ. Rev.* **2013**, *27*, 778-788
274. Linden, David; Reddy, Thomas B. *Handbook Of Batteries,* **2002,** New York: McGraw-Hill. p. 23
275. Ruetschi, P. *J. Power Sources* **2004**, *127*, 33-44
276. Goodenough, J. B.; Park, K.-S. *J. Am. Chem. Soc.* **2013**, *135*, 1167-1176
277. Kanewskii, L. S.; Dubasova, V. S. *Russ. J. Electrochem.* **2005**, *41*, 1-16
278. Tahil, W. “The Trouble with Lithium: Implications of Future PHEV Production for Lithium Demand”, **2006**, http://www.evworld.com/library/lithium_shortage.pdf
279. Halper, M. S.; Ellenbogen, J. C. ”Supercapacitors: A Brief Overview”, **2006**, MITRE Nanosystems Group, http://www.mitre.org/tech/nanotech
280. Arico, A. S.; Bruce, P.; Scrosati, B.; Tarascon, J.-M.; van Schalkwijk, W. *Nature Mater.* **2005**, *4*, 366-377
281. Dyatkin, B.; Presser, V.; Heon, M.; Lukatskaya, M. R.; Beidaghi, M.; Gogotsi, Y. *ChemSusChem* **2013**, *6*, 2269-2280
282. Jayalakshmi, M.; Balasubramanian, K. *Int. J. Electrochem. Sci.* **2008**, *3*, 1196-1217
283. Candelaria, S. L.; Shao, Y.; Zhou, W.; Li, X.; Xiao, J.; Zhang, J.-G.; Wang, Y.; Liu, J.; Li, J.; Cao, G. *Nano Energy* **2012**, *1*, 195-220
284. Frackowiak, E. *Phys. Chem. Chem. Phys.* **2007**, *9*, 1774.
285. Qu, D. *J. Power Sources* **2002**, *109*, 403-411
286. Garcia-Gomez, A.; Miles, P.; Centeno, T. A.; Rojo, J. M. *Electrochim. Acta* **2010**, *55*, 8539
287. Calvo, E. G.; Ania, C. O.; Zubizarreta, L.; Menendez, J. A.; Arenillas, A. *Energ. Fuels* **2010**, *24*, 3334
288. Wang, J.; Zhang, S. Q. *J. Electrochem. Soc.* **2001**, *148*, 75-77
289. Kim, S. J.; Hwang, S. W.; Hyun, S. H. *J. Mater. Sci.* **2005**, *40*, 725-731

290. Li, W.; Reichenauer, G.; Fricke, J. *Carbon* **2002**, *40*, 2955-2959

291. Li, J.; Wang, X.; Huang, Q.; Gamboa, S.; Sebastian, P. J. *J. Power Sources* **2006**, *158*, 784-788

292. Fang, B.; Binder, L. *J. Power Sources* **2006**, *163*, 616-622

293. Fischer, U.; Saliger, R.; Bock, V.; Petricevic, R.; Fricke, J. *J. Porous Mater.* **1997**, *4*, 281-285

294. Pandolfo, A. G.; Hollenkamp, A. F. *J Power Sources* **2006**, *157*, 11-27

295. Zhang, L. L.; Zhao, X. S. *Chem. Soc. Rev.* **2009**, *38*, 2520-2531

296. Frackowiak, E.; Beguin, F. *Carbon* **2002**, *40*, 1775-1787

297. Bordjiba, T.; Mohamedia, M.; Dao, L. H. *Adv. Mater.* **2008**, *20*, 815-819

298. Pico, F.; Rojo, J. M. *J. Electrochem. Soc.* **2004**, *151*, 831-837

299. Du. C. S.; Yeh, J. Pan, N. *Nanotech.* **2005**, *16*, 350-353

300. Niu, C.; Sichel, E. K.; Hoch, R.; Moy, D.; Tennet, H. *Appl. Phys. Lett.* **1997**, *70*, 1480-1482

301. Frackowiak, E.; Metenier, K.; Bertagna, V.; Beguin, F. *Appl. Phys. Lett.* **2000**, *77*, 2421-2423

302. An, K. H.; Kim, W. S.; Park, Y. S.; Choi, Y. C.; Lee, S. M.; Chung, D. C.; Bae, D. J.; Lim, S. C.; Lee, Y. H. *Adv. Mater.* **2001**, *13*, 497-500

303. Hu, C.-C.; Liu, M.-J.; Chang, K.-H. *Electrochim. Acta* **2008,** *53*, 2679

304. Park. B.-O.; Lokhande, C. D.; Park. H.-S.; Jung, K.-D.; Joo, O.-S. *J. Power Sources* **2004**, *134*, 148

305. Jang, J. H.; Kato, A.; Machida, K.; Naoi, K. *J. Electrochem. Soc.* **2006**, *153,* A321

306. Patake, V. D.; Pawar, S. M.; Shinde, V. R.; Gujar, T. P.; Lokhande, C. D. *Curr. Appl. Phys.* **2010**, *10*, 99

307. Fang, W. C.; Chen, K.-H.; Chen, L.-C. *Nanotech.* **2007**, *18*, 485716

308. Wang, R.; Yan, X. *Sci. Reports* **2014,** *4*, 1-9

309. Chen, H.-C.; Cheng, W.-Y.; Wang, Y.-H.; Lu, S.-Y. *Adv. Func. Mater.* **2012**, *22*, 5038-5043

310. Lokhande, C. D.; Dubai, D. P.; Joo, O.-S. *Curr. Appl. Phys.* **2011**, *11*, 255-270

311. Arbizzani, C.; Mastragostino, M. *J. Power Sources* **2001**, *100*, 164-170

312. Snook, G. A.; Kao, P.; Best, A. S. *J. Power Sources* **2011**, *196*, 1-12

313. Kou, Y.; Xu, Y.; Guo, Z.; Jiang, D. *Angew. Chem. Int. Ed.* **2011**, *50*, 8753-8757

314. Roberts, M. E.; Wheeler, D. R.; McKenzie, B. B.; Bunker, B. C. *J. Mater. Chem.* **2009**, *19*, 6977-6979

315. Lin, C.-C.; Velusamy, M.; Chou, H.-H.; Lin, J. T.; Chou, P.-T. *Tetrahedron* **2010**, *66*, 8629-8634
316. Zhang, Y.; Zuniga, C.; Kim, S.-J.; Cai, D.; Barlow, S.; Salman, S.; Coropceanu, V.; Bredas J.-L.; Kippelen, B.; Marder, S. *Chem. Mater.* **2011**, *23*, 4002-4015
317. Sadki, S.; Schottland, P.; Brodie, N.; Sabouraud, G. *Chem. Soc. Rev.* **2000**, *29*, 283-293
318. Nalwa, H. S. "Handbook of Advanced Electronic and Photonic Materials and Devices" **2001**, Academic Press: London, p. 15-16
319. Macdonald, D. D. *Electrochim. Acta* **2006**, *51*, 1376-1388
320. Paul, S.; Kim, J.-H.; Kim, D.-W. *J. Electrochem. Sci. Tech.* **2011**, *2*, 91-96
321. Ahmed, E.; Ren, G.; Kim, F. S.; Hollenbeck, E. C.; Jenekhe, S. A. *Chem. Mater.* **2011**, *23*, 4563-4577
322. Chopin, S.; Chaignon, F.; Blart, E.; Odobel, F. *J. Mater. Chem.* **2007**, *17*, 4139-4146
323. Sahu, D.; Tsai, C.-H.; Wei, H.-Y.; Ho, K.-C.; Chang, F.-C.; Chu, C.-W. *J. Mater. Chem.* **2012**, *22*, 7945-7953
324. Shang, H.; Fan, H.; Liu, Y.; Hu, W.; Li, Y.; Zhan, X. *Adv. Mater.* **2011**, *23*, 1554-1557
325. Metri, N.; Sallenave, X.; Beouch, L.; Plesse, C.; Goubard, F.; Chevrot, C. *Tet. Lett.* **2010**, *51*, 6673-6676